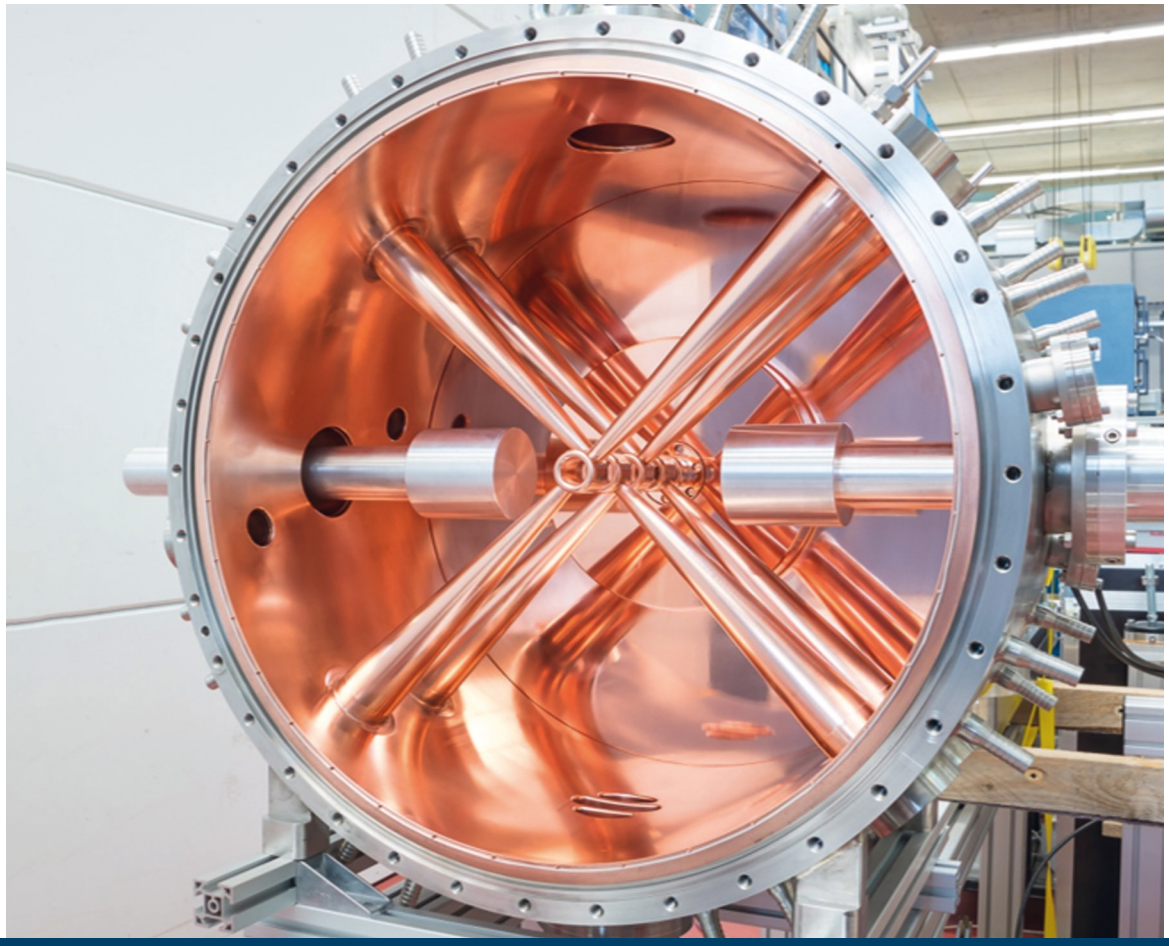

Technical Design Report HBS
Volume 1 – Accelerator

R. Gebel, A. Lehrach, H. Podlech (Vol. Eds.), T. Brückel, T. Gutberlet (Ser. Eds.)

J. Baggemann, M. Droba, O. Felden, T. Gutberlet, H. Kleines, K. Kümpel, S. Lamprecht, E. Mauerhofer, O. Meusel, I. Pechenitzkiy, N. Petry, S. Reimann, U. Rücker, M. Schwarz, P. Zakalek, C. Zhang

Allgemeines / General
Band / Volume 9-01
ISBN 978-3-95806-709-7

Mitglied der Helmholtz-Gemeinschaft

JÜLICH
Forschungszentrum

Schriften des Forschungszentrums Jülich
Reihe Allgemeines / General Band / Volume 9-01

Forschungszentrum Jülich GmbH
Jülich Centre for Neutron Science (JCNS)
Quantenmaterialien und kollektive Phänomene (JCNS-2 / PGI-4)

Technical Design Report HBS
Volume 1 – Accelerator

R. Gebel, A. Lehrach, H. Podlech (Vol. Eds.)
T. Brückel, T. Gutberlet (Ser. Eds.)

J. Baggemann, M. Droba, O. Felden, T. Gutberlet, H. Kleines, K. Kümpel, S. Lamprecht, E. Mauerhofer, O. Meusel, I. Pechenitzkiy, N. Petry, S. Reimann, U. Rücker, M. Schwarz, P. Zakalek, C. Zhang

Schriften des Forschungszentrums Jülich
Reihe Allgemeines / General Band / Volume 9-01

ISSN 1433-5565 ISBN 978-3-95806-709-7

Bibliografische Information der Deutschen Nationalbibliothek.
Die Deutsche Nationalbibliothek verzeichnet diese Publikation in der
Deutschen Nationalbibliografie; detaillierte Bibliografische Daten
sind im Internet über http://dnb.d-nb.de abrufbar.

Herausgeber und Vertrieb:	Forschungszentrum Jülich GmbH Zentralbibliothek, Verlag 52425 Jülich Tel.: +49 2461 61-5368 Fax: +49 2461 61-6103 zb-publikation@fz-juelich.de www.fz-juelich.de/zb
Umschlaggestaltung:	Grafische Medien, Forschungszentrum Jülich GmbH
Druck:	Grafische Medien, Forschungszentrum Jülich GmbH
Copyright:	Forschungszentrum Jülich 2023

Schriften des Forschungszentrums Jülich
Reihe Allgemeines / General, Band / Volume 9-01

ISSN 1433-5565
ISBN 978-3-95806-709-7

Vollständig frei verfügbar über das Publikationsportal des Forschungszentrums Jülich (JuSER)
unter www.fz-juelich.de/zb/openaccess.

CONTENTS

I.

INTRODUCTION

Accelerator-based neutron sources provide a versatile and effective opportunity to improve and spread neutron access in Europe and also a new route for the supply of neutrons to science and industry with leading-edge research infrastructures. The HBS project pushes the performance of such sources to the technological limits by employing state-of-the-art technologies in accelerator development, target and moderator design as well as beam extraction, beam optics and instrumentation. Based on a high current low energy proton accelerator, which produces powerful pulsed beams hitting a metal target (tantalum for HBS) to release a thermal neutron flux comparable to existing medium to high flux reactor sources, a variable suite of neutron instruments and applications can be served.

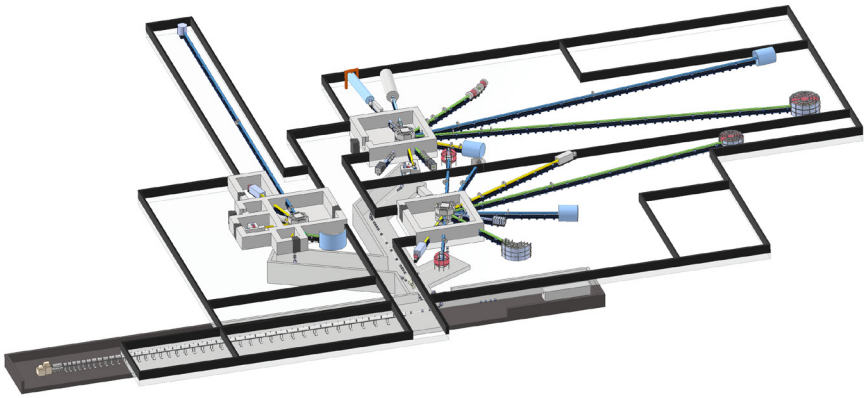

Figure I.1: *General layout of the HBS facility*

Main components of the HBS (Fig. I.1) are

- a dedicated proton accelerator with an optimized energy of 70 MeV and a current of 100 mA that is multiplexed to feed several target stations operated at different frequencies.
- a target – moderator combination (described in TDR Target Stations and Moderators) that offers a pulsed neutron beam at optimal frequency, pulse duration and neutron spectrum to fulfil the needs of the corresponding instruments.
- optimized moderators (described in TDR Target Stations and Moderators) according to the spectral needs of individual instruments.

- a number of instruments (described in TDR Instrumentation) at each target station.

The construction of the buildings, organisation and sustainable operation of the facility are outlined in the TDR Infrastructure and Sustainability. This volume of the TDR series presents the design of the accelerator system of the HBS.

I.1 Accelerator parameters

H. Podlech, O. Meusel, U. Rücker

The High Brilliance Neutron Source (HBS) belongs to the class of High Current Accelerator based Neutron Sources (Hi-CANS). The driver accelerator for HBS must be able to reliably accelerate a 100 mA proton beam to an energy of 70 MeV. The beam is sent pulse-by-pulse to three different targets by means of a multiplexer in the High Energy Beam Transfer (HEBT) section (see fig. O.1). Each individual proton beam behind the multiplexer has a specific time structure in order to optimally serve the different instruments grouped around one target station. The minimum power requirement per target is 100 kW average power. The repetition rates are adapted to the pulse lengths in order to obtain the same average power.

Required	Specifications	Unit	Detail/Comment
Particle type	Protons	N/A	User requirement
Accelerator type	RF Linac	N/A	
Beam current	100	mA	Output current
Final energy	70	MeV	User requirement
Beam duty factor	4.8 (up to 20)	%	User requirement
RF duty factor	7 (up to 25)	%	Required for cavity filling
Pulse length	167/167/667	μs	User requirement
Repetition rate	96/96/24	Hz	User requirement
Average beam power	420 (1400)	kW	can be upgraded
Peak beam power	7	MW	
Availability	>95	%	During scheduled operation
Maintainability	Hand-on	N/A	
Life time	>25	Years	

Table I.1: *Top level performance requirements of the HBS linac.*

Presently three target stations are planned. One station will be driven with 24 Hz and 667 μs, the two other stations are using 96 Hz and 167 μs. A maximum average beam power of 140 kW per target and 420 kW total beam power, respectively, is obtained. For all pulses, the beam peak power is identical to 7 MW. The beam duty factor is 4.8 to 11.6 % and the RF duty factor is 7 to 12.5 % because of the high loaded quality factor (2000–10000) of the cavities; a 50–100 μs RF pulse length must be added to the macro pulse length in order to be able to build up the nominal fields in the cavities. However, for future upgrades (e.g. 4th target station or higher target power) the accelerator should be able to be operated with a maximum RF duty cycle of up to 25 % and with a beam duty cycle of up to 20 %. The top level performance requirements of the accelerator are summarized in Table I.1 and the requirements in various operation modes in Table I.2.

Type of target station	Place	Power	Duty cycle (RF)
Long pulse (about 24 Hz)	junction of multiplexer	100 kW	1.6 % (1.8 %)
High resolution (about 96 Hz), maybe 2x	junction of multiplexer	100 kW	1.6 % (2.6 %)
Isotope production	beam stop of accelerator or straight direction of multiplexer	500 kW	8 % (8.1 %)
Epithermal and fast neutrons (about 4000 Hz)	straight direction of multiplexer	500 kW	in the burst: 50–80 %, in between larger gaps, 1.6 % (3.5 %) or 8 % (8.1 %)
High frequency (about 200 Hz)	straight direction of multiplexer	160 kW 160 kW	2.5 % (3.5 %) 2.5 % (3.5 %)

Table I.2: *Various operation modes and requirements of the HBS linac.*

I.2 HBS in the context of accelerator based neutron sources

T. Gutberlet, H. Podlech

Various methods are available for the generation of neutrons. The best known technology is nuclear fission in nuclear reactors. Also well known and used is spallation with high-energy proton accelerators. Other methods to produce neutrons are neutron generators using DT or DD fusion reactions, nuclear reactions with low-energy proton or deuteron accelerators, electron accelerators creating Bremsstrahlung for neutron generation and high power lasers.

Spallation use high energy proton beams with energies above 500 MeV. As accelerators, cyclotrons (PSI), synchrotrons (ISIS) or linacs (SNS, ESS) are used. Modern high power spallation sources use powerful linacs, which can deliver the desired pulse structure with high average power up to some MW. The high proton energy leads to high investment costs (>1 Billion EUR), so these sources tend to be of trans-national character.

For low and medium energy accelerators using nuclear reactions for neutron production with lithium, beryllium, or tantalum targets, there are different possibilities. So called compact accelerator based neutron sources (CANS) have beam powers from less than 1 kW to about 10 kW. Systems with a beam power exceeding 100 kW have not yet been realized. Due to the significantly lower investment costs compared to spallation sources, a larger number of CANS can be realized and optimized for users with respect to peak power and pulse structure. HBS, with an energy of 70 MeV, belongs to the class of high current compact accelerator based neutron sources (HiCANS). Different types of accelerator systems could be considered to drive HBS.

Cyclotrons

In a cyclotron, charged particles pass from the ion source to the center and are accelerated. The particles are accelerated by an RF electric field while being guided in a static magnetic field. With each revolution, the energy of the charged particles increases and the radius of their orbit increases, resulting in a spiral path in the cyclotron. Cyclotrons are usually limited to currents on the order of

1 mA. This and their maximum beam energy dictate the maximum strength of the neutron source from a given target. There are developments to significantly increase the current limit in cyclotrons (I>10 mA). However, these developments require a significant R&D effort in terms of financial resources with longer time scales. It is questionable that cyclotron can reach peak beam currents required by HBS. A major drawback is the lack of scalability especially with respect to the maximum energy and beam power.

Electrostatic accelerators

The conceptually simplest accelerator for charged particles is the electrostatic accelerator, which uses static electric fields to accelerate ions. An important advantage of an electrostatic accelerator compared to an electrodynamic accelerator is the ability to accelerate different ions with the same accelerate structure. The technology is relatively simple compared to RF accelerators. Classical Van-de-Graaf and tandem accelerators, respectively, are limited in peak currents (I<1 mA) and energy (a few MeV to about 15 MeV). Tandetron electrostatic quadrupole accelerators can deliver higher currents up to about 30 mA, but have so far only been realized for energies of 2–3 MeV. Peak beam powers in the MW range and average powers of several 100 kW or more do not seem feasible with these facilities.

RF Linacs

Compact linacs for high ion (proton or deuteron) currents combine a radio frequency quadrupole with a drift tube linac (DTL). The advantages of using ion linacs are that they enable optimization and operation in continuous wave (CW) or pulsed mode, or both enabling high beam currents with low beam loss. Compared to a typical cyclotron, similar beam losses in a linac occur at a current one order of magnitude higher in CW operation and about two orders of magnitude higher in pulse operation They also enable neutron production in a single (nuclear) interaction, making the neutron production scheme more efficient for many applications and less complex than in electron accelerators. In addition they can operate at different beam energies, which can be optimized for the required neutron source.

For HBS, an RF Linac is the most promising solution. This is especially true because of the high peak and average beam power. Such a driver accelerator consists of the following sections:

- An ion source whose task is to generate a high intensity proton beam with energies in the range of 30–100 keV and currents above 100 mA
- A Low Energy Beam Transport (LEBT) whose task is to prepare the beam for injection into the Radio Frequency Quadrupole and to create a suitable macro pulse structure.
- A Radio Frequency Quadrupole (RFQ), whose task is to accelerate the low energy proton beam and to focus the beam into bunches
- A Medium Energy Beam Transfer section (MEBT) for matching into a drift tube Linac
- A Drift Tube Linac (DTL) to accelerate the protons to their final energy
- A High Energy Beam Transfer section (HEBT) to steer the beam to the target stations

I.3 Choice of technology

H. Podlech

Worldwide there is an increasing interest in a new generation of high power proton and ion Linacs. The term high power refers to the product of beam energy and beam current which is the beam power. With a peak beam power of 7 MW and an average power of at least 420 kW, HBS is clearly a high power Linac (Fig I.2 and I.3).

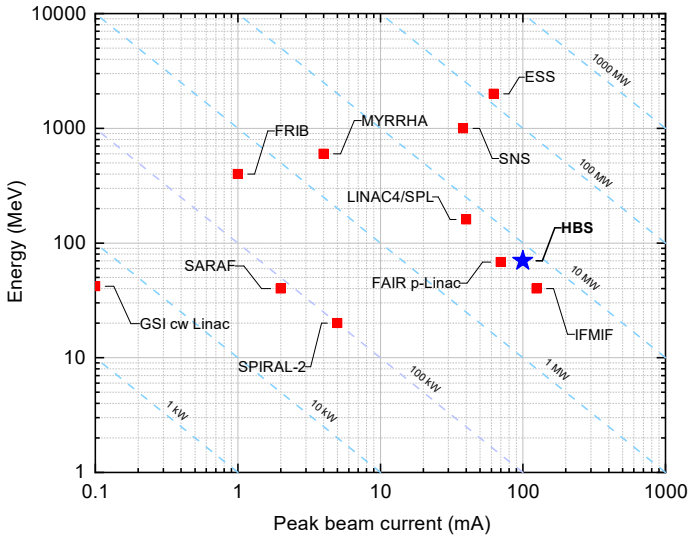

Figure I.2: Peak beam power of modern hadron Linacs.

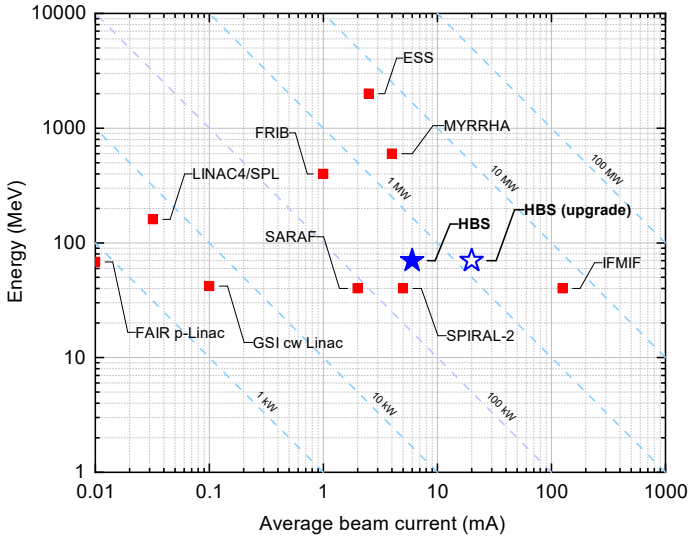

Figure I.3: Average beam power of modern hadron Linacs.

The typical modern hadron linac consists of three major parts (Fig. I.4). The unit AMeV refers to heavy ion linacs. For proton accelerators A is equal to 1.:

- front end (low energy part, E=0.1–5 AMeV)
- drift tube linac (intermediate energy part, E=3–200 AMeV
- superconducting section (high energy part, E>100 AMeV)

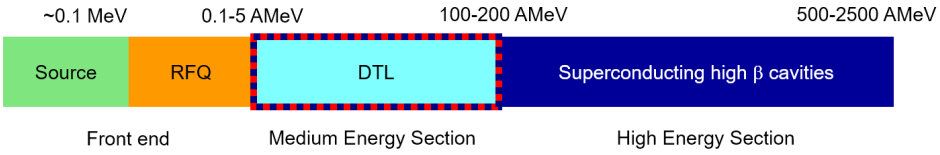

Figure I.4: *Scheme of modern High Power Hadron Linacs.*

One of the most important issues of high-power hadron linacs is the choice of technology with respect to superconducting or room-temperature operation. The advantage of a certain technology depends on various parameters. These include the RF duty cycle η, the peak beam current I and the final energy [Pod13]. The front-end consists of an ion source, a Low Energy Beam Transport (LEBT) and a Radio Frequency Quadrupole (RFQ). The vast majority of all RFQ structures have been realized using normal conducting technology because of particles losses in the RF structure which would likely lead to thermal quench in case of high power Linacs.

The high-energy section starts typically between 100 AMeV and 200 AMeV and mostly uses superconducting elliptical multi-cell cavities and more recently superconducting double-Spoke cavities (ESS, MYRRHA). Even for lower duty factors superconducting cavities are a good choice in most cases with respect to the overall required radio-frequency (RF) and plug power. In the case of the intermediate energy part, which is completely covered by the HBS Linac the situation is not as clear. An important parameter is the transition energy between the room temperature and the possible superconducting section. In general, the higher the duty factor and the lower the beam current, the smaller the transition energy (Fig. I.5 and I.6).

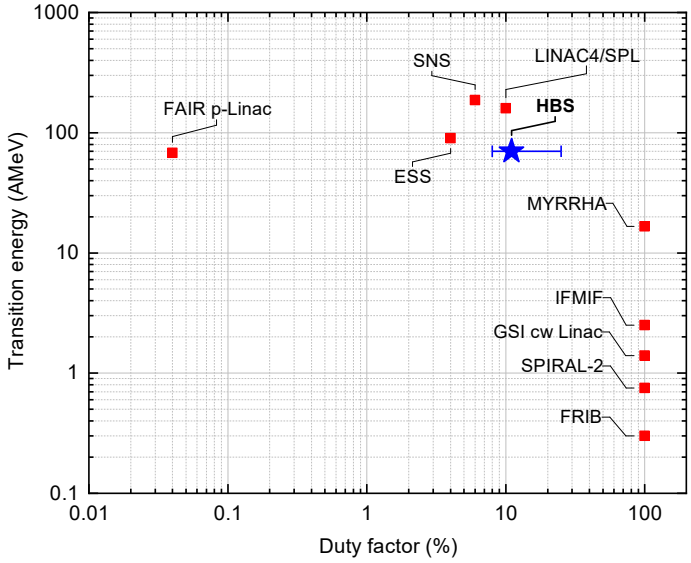

Figure I.5: *Transition energy as function of the duty factor of modern Hadron Linacs. For fully room temperature Linacs the transition energy is the final energy. The horizontal bar for HBS represents the duty factor range depending on the pulse scheme and further upgrades.*

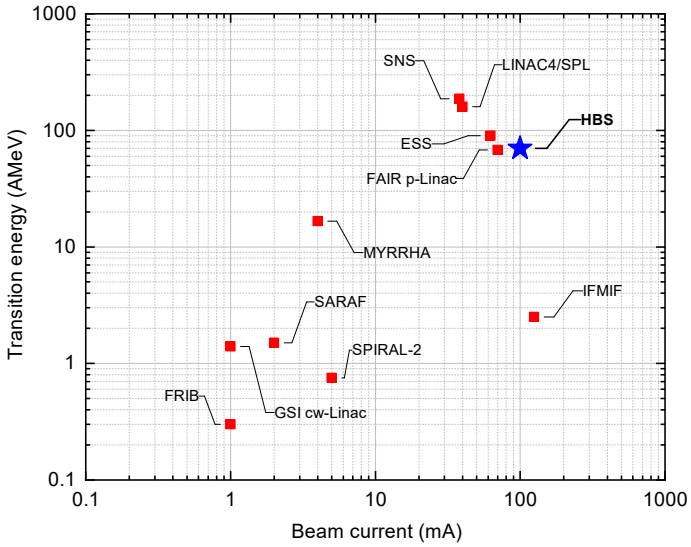

Figure I.6: Transition energy as function of the peak beam current. For fully room temperature Linacs the transition energy is the final energy.

Each project has to make the choice which is the best suited technology for the specific application. The main issues are capital costs, operating costs (power), technical risk, reliability and availability. During the last few decades the transition energy between normal conducting and superconducting technology decreased significantly. The main reasons for this are lower operation costs for high duty factor machines and especially the availability of suitable superconducting RF structures in the low- and medium-energy range such as quarter-wave resonators, half-wave resonators and CH cavities.

In general, the shunt impedance is higher at low energies. There are very efficient low-energy drift tube structures such as H-mode cavities available. Above 100 MeV superconducting cavities are the best choice in most cases even for machines with lower duty cycle because there are no real efficient

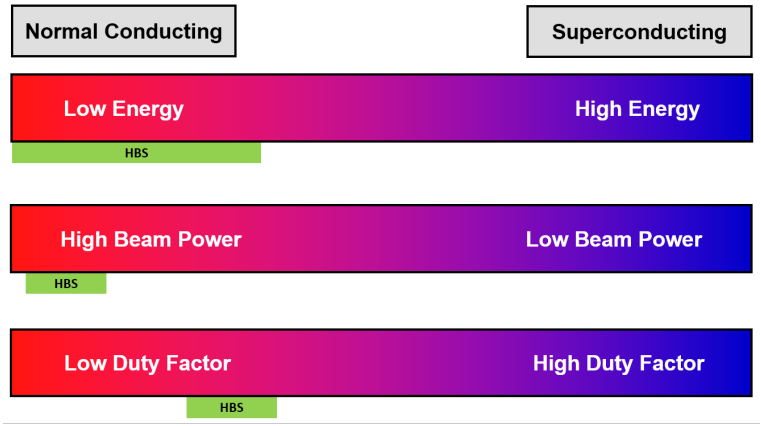

Figure I.7: The favor for room temperature or superconducting technology depends mainly on the energy, beam current and duty factor.

normal conducting structures available. On the other side, superconducting high energy cavities can reach high gradients (E_a >10 MV/m) resulting in a much shorter linac. In general, normal conducting cavities are more favourable at lower energies with high beam current and low duty cycle. For superconducting cavities the opposite is valid (Fig. I.7) [Pod13]. Both technologies have their advantages and disadvantages. Superconducting technology requires a cryogenic plant with associated helium distribution. The development of superconducting cavities and cryo-modules requires a large R&D effort with respect to simulations and prototyping. For each cavity type specific high power coupler have to be developed. In addition, these cavities are very sensitive to contaminations, pressure variations, multi-pacting and vibrations and they need under certain circumstances complex fast frequency tuning systems [Pod13].

Because of the high beam current the required RF power is dominated by the beam power even for room temperature cavities. In case of HBS, superconducting cavities providing 2.5 MeV will need 250 kW RF power plus appropriate margin. For comparison, an equivalent room temperature structure requires about 100 kW more RF power. Because of the much simpler technology avoiding a cryogenic plant, the development of cryo-modules and suitable power couplers a room temperature solution is preferred for HBS.

I.4 Design philosophy for the HBS linac

H. Podlech, A. Lehrach

The realization of high power proton accelerators is usually associated with a large R&D effort with corresponding resources regarding man power, prototyping and testing infrastructure. In the case of HBS, this development effort should be minimized by using already developed and proven technology. This lowers the costs and the time frame of the development and minimizes risks regarding construction costs, technological difficulties and time schedule. The design objectives of the HBS Linac should aim for an accelerator system to be as efficient as possible (length, RF power) and as reliable as possible as a user facility (see Fig. I.8). High reliability and availability can be achieved by implementing a modular design that allows easy access to all components for repair and main-

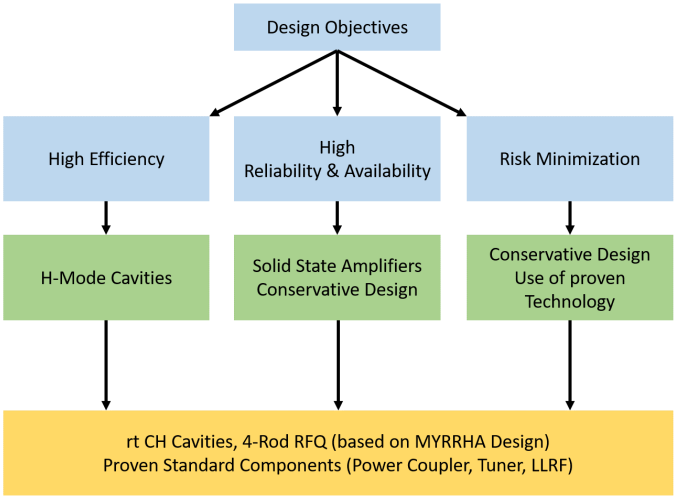

Figure I.8: *The design philosophy of the HBS-Linac is driven by obtaining high availability, risk minimization, high efficiency and cost reduction.*

tenance. Furthermore, all components should be operated well below their technical and physical limitations. Redundancies in critical components can significantly increase reliability and availability.

The RF duty factor of up to 25 % already leads to significant thermal loads in the cavities. For the 17 MeV injector of the MYRRHA project cw capable CH-cavities and the corresponding RFQ were developed [HKK+19][PKL+17][GBD+21]. The thermal loads for this project add up to 35 kW/m. The technology for the MYRRHA Linac is successfully tested and is now also available for future neutron sources. Just like MYRRHA, the frequency of HBS will be 176.1 MHz. This frequency makes it possible to adopt the MYRRHA technology. Additionally, the frequency is well suited for high beam currents and gives still efficient DTL-cavities. The MYRRHA-RFQ has been commissioned (RF and beam) with superior performance [GBD+21]. Thus, the RFQ RF structure can be adopted without any changes. The CH-cavities have to be adapted to the beam dynamics of HBS with regard to cell number and cell length. The basic geometry and the cooling system can be adopted with minor changes. Due to the RF duty factor of up to 25 %, higher gradients can be used compared to cw operation to keep the Linac length as short as possible. The exact gradient results from the maximum RF power available per cavity and the beam dynamics. The subsystems of the cavities such as power couplers and frequency tuners can also be used. Presently, a conservative beam dynamic with a constant negative synchronous phase is foreseen. The Drift Tube Linac consists of modular accelerating sections. Each section consists of one cavity, one quadrupole triplet and at least one beam diagnostic device. Above 20-25 MeV, EQUUS beam dynamics could be used, where the cell length is constant. The modular Linac design with short CH-cavities limit the amplifier power to 500 kW. This allows the use of Solid State Amplifiers (SSA). This modern technology offers significant advantages over classic tube amplifiers. Apart from a significantly smaller foot print, no high voltage is required. Due to the modular design of these amplifiers, individual amplifier modules can fail without interrupting operation resulting in an increased reliability and availability of the whole facility.

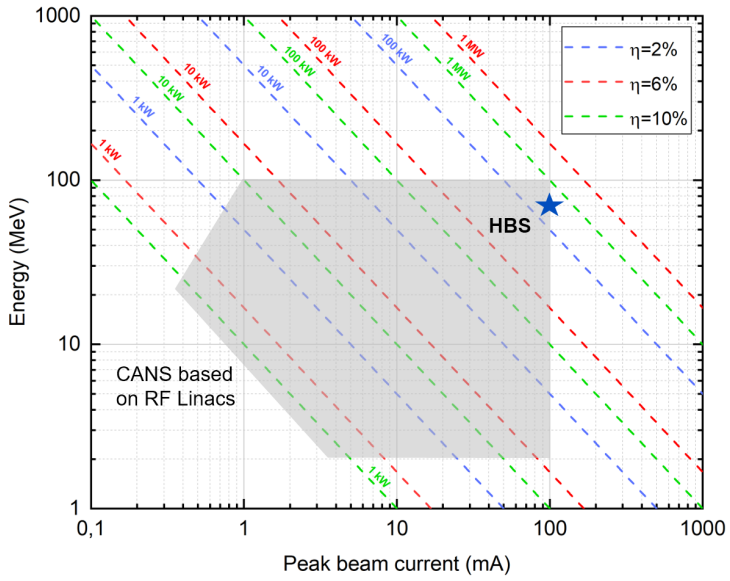

Figure 1.9: *The shaded area shows the combinations of peak beam current and energy for compact accelerator based neutron sources (CANS). Depending on the beam duty factor different average power levels are obtained (coloured lines for η=2 %, 6 % and 10 %. The HBS design concept can cover the whole area only by adapting the front-end and the number of cavities.*

Since further accelerator-based neutron sources will be needed in the future, it is advisable to design HBS modular and scalable. Duty cycle, beam current, pulse lengths and energy can then be varied over a wide range without fundamentally changing the design (Fig. I.9). If necessary, only the front end has to be adapted for modified beam currents. The drift tube linac can consist of exactly the same lattice and is only adapted in length to the required energy. Figure I.10 shows the base line design of the HBS linac following the design philosophy and the requirements of HBS.

Figure I.10: *Conceptual layout of the HBS linac.*

I.5 Realisation

T. Gutberlet

The realization of high power proton accelerators is usually associated with a large R&D effort with corresponding resources regarding man power, prototyping and testing infrastructure. In the case of HBS, this development effort are minimized by using already developed technology. This lowers the costs and the time frame of the development and minimizes risks regarding construction costs, technological difficulties and time schedule. The HBS Linac should be as efficient as possible (length, RF power) and as reliable as possible as a user facility. High availability is achieved by implementing a modular design that allows easy access to all components for repair and maintenance. Furthermore, all components will be operated well below their technical and physical limitations. Redundancies in critical components significantly increases reliability and availability. Most components of the HBS-Linac are based on technology developed for the MYRRHA Project as the design of this high power cw operated accelerator does fit very well for the demands of HBS.

As detailed in volume TDR Infrastructure & Sustainability the facility is constructed in in three building stages. This means that at first, the accelerator with certain basic energy, one target station and instrument hall and one part of the HEBT and multiplexer system can be built. In the second and third stage the full facility will be realized (see Vol. TDR Infrastructure & Sustainability).

II.

FRONT END

K. Kümpel, H. Podlech, O. Meusel, M. Schwarz, C. Zhang

The front-end of the HBS-Linac covers the area from the proton source to the Medium Energy Beam Transfer (MEBT) before the injection into the drift-tube Linac. This section has to fulfill several tasks. After the beam creation in the proton source, the beam has to be transported to the entrance of the RFQ using the Low Energy Beam Transfer (LEBT). The LEBT has also to match the transverse phase space to the acceptance of the RFQ. By means of a chopper, the necessary pulse structure is imposed on the DC beam in front of the RFQ. The beam energy at injection into the drift-tube Linac is 2.5 MeV. Because of the frequency of 176.1 MHz, the RFQ would become impracticable long. Therefore, it has been decided to split the RFQ into two independently phased RF structures. To have maximum flexibility for matching (longitudinal and transverse), a first Medium Energy Beam Transfer (MEBT-1) will be used in between the two RFQ-structures. After the second RFQ, the MEBT-2 is matching the beam into the acceptance of the drift-tube Linac. The front-end is a very critical section especially with respect to beam dynamics because of the high space charge forces at this low energy. The emphasis during the design was on the minimization of emittance growth and only to lesser extent on efficiency.

II.1 Ion source

O. Meusel, R. Gebel

The source will provide a DC beam with a proton current of at least 120 mA. Several source types are available but with respect to reliability, availability, maintenance and high proton fraction, an Electron Cyclotron Resonance Source (ECR) is favourable. Table II.1 summarizes the main parameters of the proton source and Figure II.1 shows a schematic sketch. The RF-power needed for the plasma generation will be provided by a magnetron and RF-infrastructure like circulator, bi-directional coupler and tuner. The RF frequency is $f_{\text{Source}} = 2.45\,\text{GHz}$ with a power range of $P_{\text{Source}} \approx 0.3\text{–}1.5\,\text{kW}$.

It should be possible to switch between with or without ECR-mode to provide a flexibility in plasma generation. The proton source already developed at FZJ provides a proton beam with required specification after minor modifications. The RF-driven plasma produces a beam with a proton fraction of 90 %. Therefore, the extracted beam current has to be adapted to the proton fraction with an accepted fluctuation of 2 %. Each of the unwanted fraction consisting of H_2^+ and H_3^+ are extracted as well. Their intensities are inverse proportional to the plasma temperature. On the other hand, high plasma temperatures lead to high beam emittances. Balancing both values needs a filter for the unwanted species.

The plasma generator and all required infra-structure as RF generator, magnets and power supplies

Parameter	Value	Unit
Source type	ECR	N/A
Beam current	>120	mA
Proton fraction	>90	%
Beam energy	85	keV
Operation mode	DC	N/A
Current Fluctuations	<2	%
Emittance (norm, rms)	0.35	πmm mrad

Table II.1: *Parameters of the proton source.*

are installed on a high voltage terminal (HVT) surrounded by a faraday cage. The dimensions of the platform are 5 m length, 4 m width and 4 m height and is supported by isolating feeds. The ion source needs power supplies for charging parts of the plasma generator and extraction system as well as applying the magnetic field for plasma confinement. All devices include infrastructure for cooling and ventilation support will need an electrical power of 40 kW which will be provided by an isolating transformer. The cooling water will be transferred to the platform by a double heat exchanger following the water-oil-water chain to minimize dark currents. The high voltage power supply has to provide the terminal voltage as well as the current which is the sum of dark currents and the beam current. The beam current is planned to be 120 mA in the first stage to deliver 100 mA proton beam current at the neutron production targets. For future upgrades the beam current could be increased to more than 200 mA (Fig. II.1).

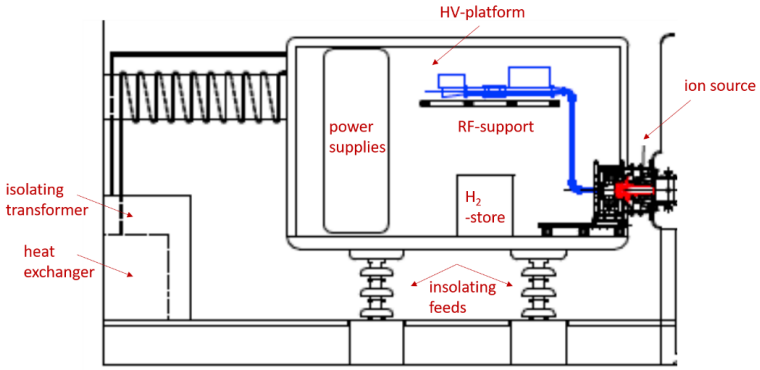

Figure II.1: *View of the ECR-source with high voltage platform. The protons are created in the plasma generator which is fed by an 2.45 GHz RF amplifier. The beam will be formed by a triode acceleration-deceleration extraction system to prevent the back stream of secondary electrons. The electric field strength for the extraction has to be matched to the plasma parameters. The extraction system is integrated in the wall of the Faraday-cage and is connected to the catcher-solenoid as first part of the following low energy beam transfer section (LEBT).*

The proton beam will be formed by a triode accel-decel extraction system to prevent the back stream of secondary electrons and space charge de-compensation within the LEBT. The electric field strength for the extraction has to be matched to the plasma parameters. The extraction system is integrated in the wall of the Faraday-cage and is connected to the catcher-solenoid as first part of the following LEBT. The stray field of the catcher solenoid has an influence on the plasma dynamic within the ion

source. A dedicated control unit has to adjust the ion source with respect to the magnetic field to provide a stable plasma sheet.

II.2 Low Energy Beam Transport

O. Meusel

The LEBT is used to transport the beam from the ion source to the first accelerator stage [Wie14].The main tasks for this section of the front end are matching the emittance of the source into the acceptance of RFQ 1, providing the time structure by creating beam macro pulses and monitoring of beam properties right before the acceleration. The LEBT consists of two sections and a chopper in-between them. The first section catches the beam right after the extraction from the source and match it into the acceptance of the chopper. Because of the high space charge force, it is necessary to use a carefully designed chopper, which interrupts space charge compensation in an interaction region as short as possible. A second section will match the beam pulses into the acceptance of the RFQ 1 (see Fig. II.2).

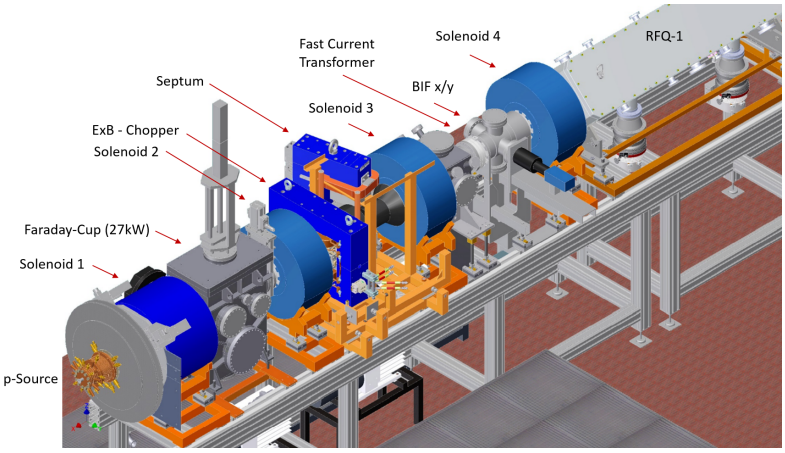

Figure II.2: *Schematic overview of the LEBT with beam optics, instrumentation and chopper.*

The length of the LEBT is 3.8 m and is designed for proton beams with currents up to 200 mA and energies up to 150 keV for future upgrades. It is also equipped with a high power Faraday-cup and non-interceptive beam diagnostic devices. Two turbo molecular pumps with pumping speed of S=2000 Ls^{-1} and S=1500 Ls^{-1} are foreseen to provide a base vacuum pressure of p_{base}=10^{-7} hPa. This low base pressure enables the possibility to add different buffer gases to improve the beam emittance, if necessary. The interface between LEBT and RFQ-1 is a matching cone to prevent space charge de-compensation and to dump the unwanted species H_2^+ and H_3^+.

II.2.1 Beam Line Layout

Solenoid 1, the catcher-solenoid is placed as close as possible to the ion source to ensure small beam spot sizes at its entrance. Due to non-linearity of the fringing field the ratio of beam diameter and aperture of the solenoid should not exceed 2/3. The solenoid 2 matches the beam into the acceptance of the ExB-Chopper. A vacuum chamber between both solenoids houses a Faraday-cup. This device can withstand beam power of about P_{beam} = 27 kW. It will be used for the adjustment

of the ion source after a maintenance or in case of an emergency a beam dump is needed. The ExB-chopper is a pulsed Wien-filter and it can provide repetition rates up to 127 kHz. Therefore, it enables a huge flexibility in macro pulse formation and duty cycle. This will be important for the beam delivery to the different neutron production targets and experimental requirements. The chopper section clears the beam finally from unwanted fractions. The second LEBT section matches the beam into the acceptance of RFQ1. It consist of two solenoids, a vacuum chamber equipped with beam diagnostics and an injection cone in-between right in front of the RFQ1. All solenoids are equipped with Lambertson-coils to provide beam steering in both transverse directions. Thus, focusing and steering will be provided at the same time without spending additional space for beam alignment. The magnetic field strength of the solenoids is B_z = 600 mT on the axis. The maximum electrical power needed for each solenoid operation is in the range of P_{Sol} = 12 kW. The steering system needs P_{steer} = 2 kW each. The cooling system for the LEBT includes the beam optic devices, the Faraday-cup as well as the beam dump of the chopper and the injection cone. The latter will be used to protect the RFQ-1 against beam mismatch and the screening of secondary electrons (Fig. II.3.

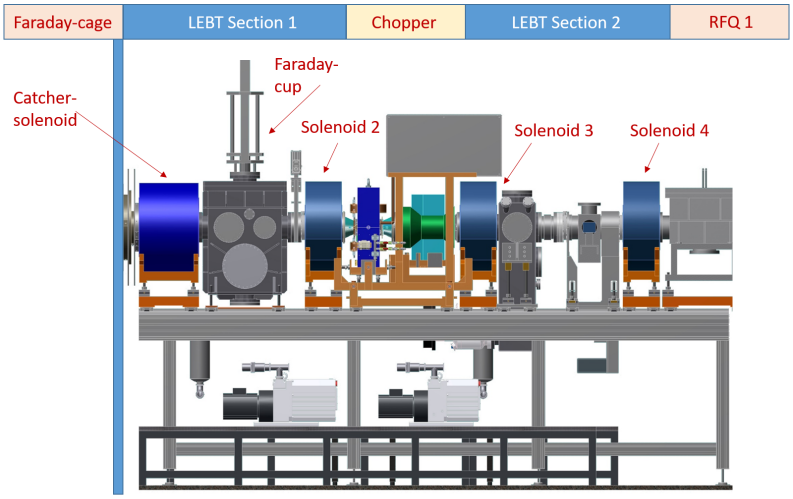

Figure II.3: *Schematic overview of the LEBT consisting of two sections with the chopper in-between. (modified from [Wie14]).*

A vacuum shot is integrated into the LEBT right downstream of the first diagnosis chamber. It will separate section 1 against the front end to provide maintenance of the proton source. A multi-purpose water cooled adapter is mounted between the gate valve and solenoid 2. It can be used for scraper or screening electrodes to remove the beam halo and the unwanted species as well as improve the space charge compensation.

II.2.2 Beam Optics

Four solenoids are used for radial-symmetric beam focusing in the LEBT. Solenoids provide space charge compensation in the LEBT without an asymmetric distortion of the compensation electron density. The focal strength of a solenoid is given by equation II.1 for both types of solenoids.

$$f = \frac{1}{k \sin(k\,L)}\,, \text{ mit } k = \frac{qB}{2m_p v_p} \tag{II.1}$$

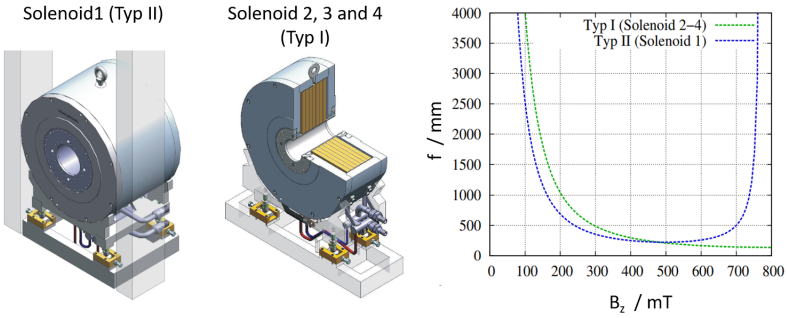

Figure II.4: *Schematic overview of solenoid type II (left), cross sectional view of solenoid type I (middle) and focal length of both of the solenoid types (right). (modified from [Wie14]).*

The first solenoid right downstream of the ion source needs a larger aperture to prevent aberrations. Therefore, this solenoid distinguish itself from the following three solenoids (Fig. II.4). It has an aperture of 175 mm, whereas the others have an aperture of 100 mm. To keep the aspect ratio for all solenoids constant, solenoid 1 has a length of 400 mm instead of 250 mm like solenoid 2, 3 and 4. The maximum field strength is $B_{z,\text{Type II,max}} = 660$ mT and $B_{z,\text{Type I,max}} = 780$ mT. The power supplies for the solenoids have to deliver 400 A at 45 V.

II.2.3 ExB Chopper

The chopper [Wie14] provides the time structure of the proton beam. To prevent high power losses within the chopper it is foreseen to extend the chopper section by a septum system with a dedicated beam dump. This allows to handle high beam intensity which will lead to high power deposition in the range of several kW. At the entrance of the chopper section solenoid 2 matches the beam into the acceptance of the chopper, whereas downstream of the section solenoid 3 catches the pulsed beam (Fig. II.5). The ExB-chopper is as much as flexible for providing different pulse length and duty cycle.

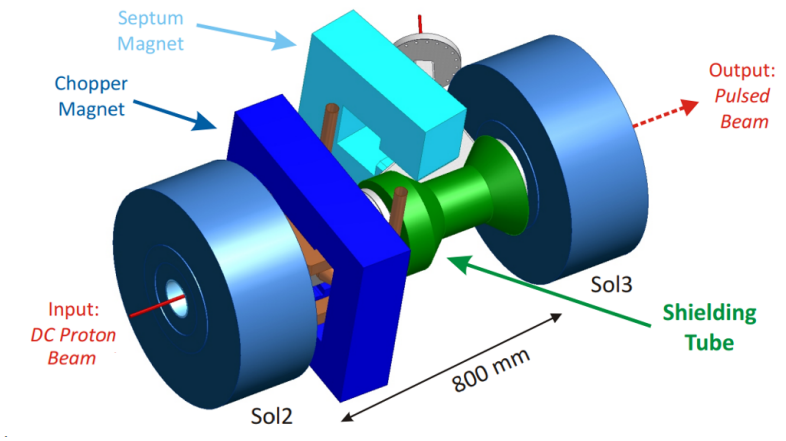

Figure II.5: *Schematic overview of the ExB chopper system enbedded between section 1 and 2 of the LEBT. (modified from [2]).*

It uses a static magnetic dipole field provided by the chopper magnet. An electrostatic deflector is embedded into the chopper magnet and provides a time dependent deflection of the proton beam.

When the proton beam passes the chopper magnet it will be deflected by the chopper magnet and from that results a transport of the beam in the high magnetic field region of the septum. Therefore, the beam will be guided in the beam dump (Fig. II.6). This operation forms the pulse breaks and can also be used to adjust the ion source after maintenance to minimize the unwanted species in the beam. When the the electric field in the deflector is applied by the fast switch the Wien-condition is fulfilled. The protons will not be deflected and consequently passes the field free region within the magnetic septum.

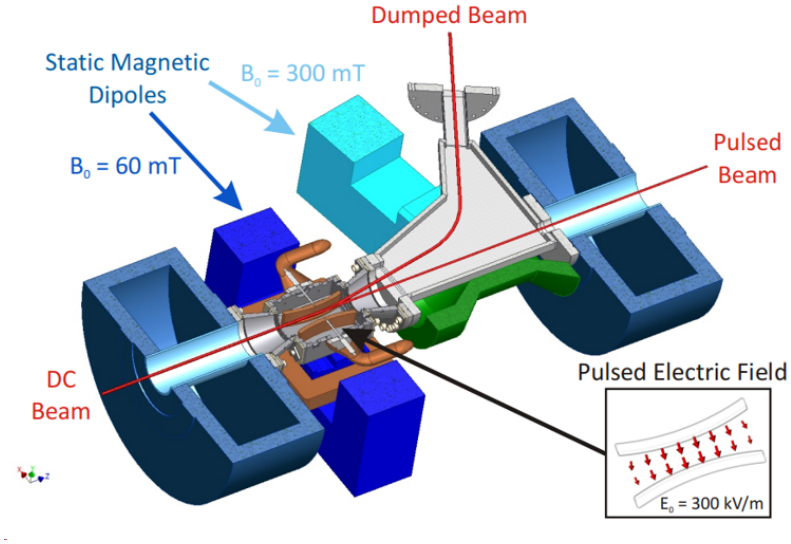

Figure II.6: *Cross sectional view of the ExB chopper with magnetic septum. (modified from [2]).*

Most ions of the unwanted species e. g. H_2^+ and H_3^+ are separated from the beam during the pulse formation and the following transport through section 2 of the LEBT.

II.2.4 Beam Instrumentation

A Faraday-cup is integrated in the first vacuum chamber of the LEBT for beam current measurements for commissioning and adjustment of the ion source. Furthermore it can be used to provide an emergency beam stop without interrupt ion of the source operation. The water cooled device can withstand a power deposition of P_{beam} = 27 kW. Downstream the chopper a fast current transformer will be used to measure the beam current and the shape of the formed beam pulses to ensure a proper functionality of the chopper. A dedicated vacuum chamber in LEBT section 2 provides beam tomography based on beam induced fluorescence. It is able to rotate around the beam with a maximum angel resolution of 1°.This delivers the proton density distribution in a volume of the beam, which can be used to evaluate the beam alignment or to reconstruct its 4D phase space distribution and emittance.

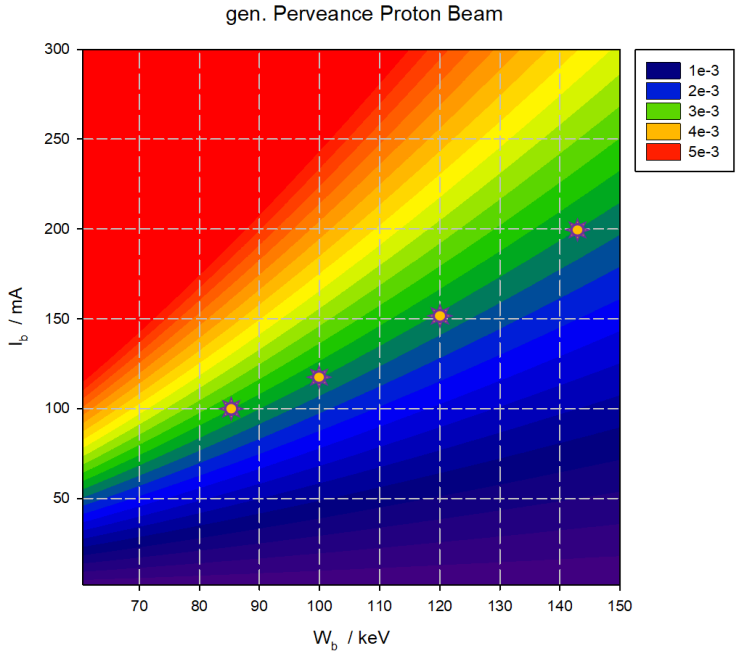

Figure II.7: *Generalized perveance of the proton beam as a function of beam energy and current, four scenarios were investigated.*

For the ion source does not exist an output emittance, so fare. Therefore, a start distribution of the proton beam was assumed under the assumption of a plasma temperature of about 30 eV and a matched extraction of the beam using a triode extractor. Therefore, the rms-emittance is given by the intrinsic momentum of the protons and is assumed to be $\epsilon_{\mathrm{rms,norm}} = 0.3\,\pi$ mm mrad. The beam dynamic is given by the KV-envelope equation under the assumption of linear electric field

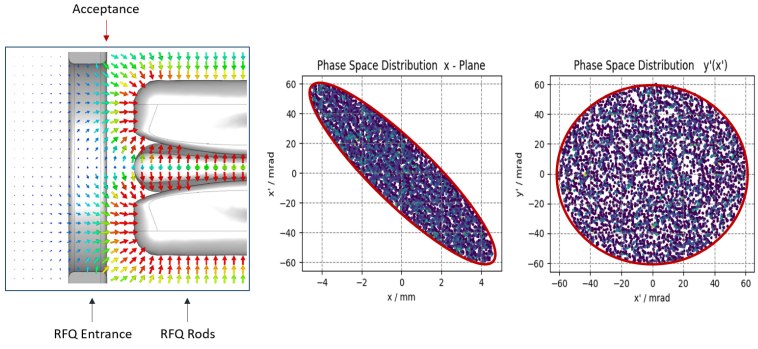

Figure II.8: *Position of the calculated acceptance (left), x-plane of phase space distribution (middle), transverse momentum distribution (right).*

of the proton beam and linear focusing strength. Space charge forces expressed by the generalized perveance are very important in LEBT sections because of the low beam energy and the resulting high proton density. The layout of the LEBT enables the possibility for future upgrades because it is possible to adjust the solenoids for an energy range from 60 to 150 keV of the proton beam. Keeping the generalized perveance below $K = 2 \cdot 10^{-3}$ allows a maximum beam current of about 200 mA.

Figure II.7 shows the generalized perveance as a function of beam energy W_b and beam current I_b. The marker represent possible operation modes. The beam dynamic was investigated for W_b = 120 keV and I_b = 150 mA as an intermediary scenario between actual design parameter and future upgrade of HBS.

The acceptance of RFQ-1 was calculated to guarantee a high transmission and low emittance growth during longitudinal compression and acceleration. Figure II.8 shows the position, where the acceptance was defined as well as the x-plane of the phase space and the transverse momentum distribution. The radial symmetric round beam should have a radius below 4.5 mm and an emittance below $\epsilon_{\text{rms,norm}} = 0.4\,\pi$ mm mrad. The transverse momenta should not exceed 60 mrad. The power density for this beam parameters is P_b = 13.36 kW cm^{-2}. Therefore, it is important to provide a stable and controlled beam injection into the RFQ-1.

II.3 Radio Frequency Quadrupole

H. Podlech, K. Kümpel, M. Schwarz, C. Zhang

Radio Frequency Quadrupoles (RFQ) are today the standard structures for focusing, bunching and accelerating a DC beam delivered by an ion source. Regardless of the used RF structure, 4 electrodes (rods, vanes) are periodically charged by RF fields and generate a time varying electric quadrupole field. As the particles pass through the RFQ, a chain of alternating electric quadrupoles acts as a strong electric focusing device in both transverse planes. Subsequent drift tube cavities require a bunched beam with a small phase and energy width to ensure high transmission and good beam quality. The bunching process has to be done very carefully to catch almost 100 % of the particles and to preserve longitudinal beam quality. In addition, the energy must be increased in the RFQ so that the length of the acceleration cells in the drift tube cavities becomes sufficiently large at a given frequency. Bunching and acceleration are achieved by longitudinal fields generated by a characteristic mechanical modulation of the electrodes. The electrode geometry is determined by the modulation m, the minimum aperture a, and the cell length $l_c = \beta\lambda/2$ (Fig. II.9). The course of these parameters essentially determines the beam dynamics properties of the RFQ. Since most of the

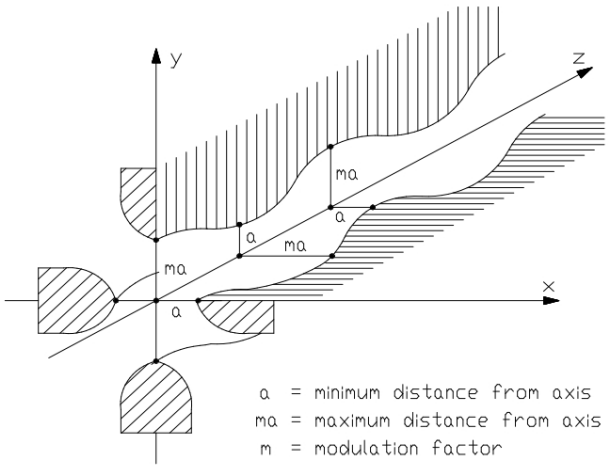

Figure II.9: *Schematic view of RFQ electrodes with definition of the modulation parameters.*

field energy is used for transversal focusing, RFQ accelerators are relatively inefficient with respect to the required RF power and length. Therefore, the transition to more efficient drift tube cavities should be made as early as possible. For beam dynamic reasons, the higher the beam current, the higher the final energy. The lighter the particles or the smaller the mass-to-charge ratio, the higher the frequency is usually chosen. For beam currents that are not too high, typical frequencies are between 300 and 400 MHz. For higher beam currents (100 mA) or high duty cycles, a lower frequency of about 200 MHz is often used to reduce the required electrode voltage.

II.3.1 RF Structure

There are different resonator types to load the electrodes to the desired quadrupole potential. The two most common RFQ structures are the 4-Vane RFQ (Fig. II.10) and the 4-Rod RFQ (Fig. II.11). The

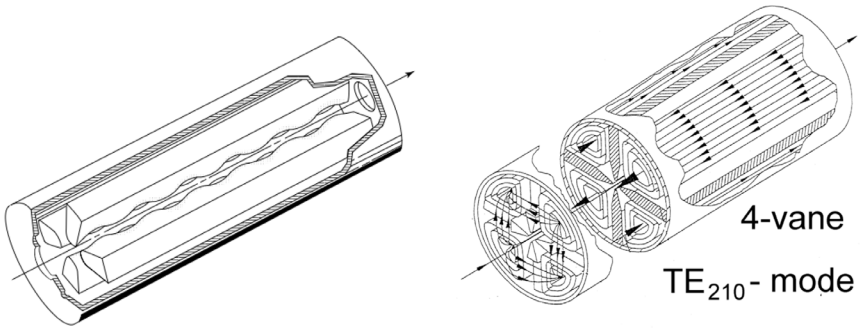

Figure II.10: *Schematic view of a 4-Vane RFQ.*

4-vane cavity is mostly used in the high frequency range above 200 MHz, for example at ESS or SNS. It is the most common structure for light ions, especially protons. The cavity consists of four vanes symmetrically placed within a cavity and is operated in TE_{21}-mode. The magnetic field is localized longitudinal in the four quadrants of the cavity. Its transverse electric field is localized near the vane tips. The resonant frequency scales with the geometric size of the cavity. Below a frequency of 100 MHz the dimensions of a 4-Vane type RFQ becomes unpractically large and the 4-Rod RFQ results in smaller structures. The 4-Vane RFQ requires perfect quadrupole symmetry to provide the necessary field quality. As a result, the tolerances for a 4-Vane RFQ are very tight. This leads to high capital costs. In addition, the technological risk for this structure is considerably high.

The 4-Rod RFQ is a well proven RF-structure. A 4-rod RFQ consists of a chain of $\lambda/4$ resonators operated in π-0-mode. The $\lambda/4$ resonators are capacitively shortened by the electrodes (see Fig. II.11. The connection of the electrodes is made by the stems and the tuning blocks representing the inductivity. Since the 4-Rod RFQ is a transmission line resonator, its tank has only minor influence on the RF behavior. 4-Rod structures have been built for frequencies up to 216 MHz. The main advantages are tuning possibilities, easy access for repair and maintenance, smaller sensitivity against tolerances and lower capital costs. The required RF power is typically slightly higher than for 4-Vane RFQs.

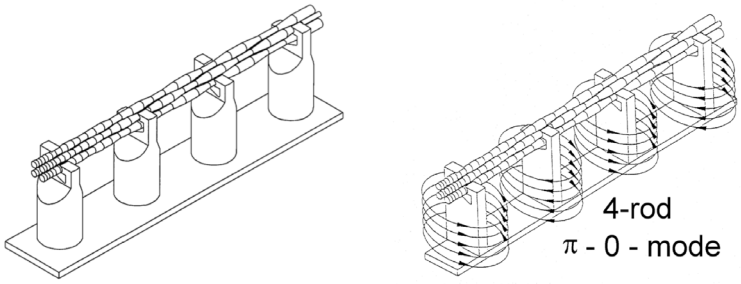

Figure II.11: *Schematic view of a 4-Rod RFQ.*

However, clear advantages are seen for the 4-Rod RFQ and therefore it is proposed as RF structure

for HBS. Cooling optimization is a major issue especially for high duty cycle or even cw operation. In the past, there were major issues with high power operation of 4-Rod RFQ structures. A prominent example is the SARAF-RFQ. Although this RFQ has shown cw operation with power levels of about 47 kW/m, several weak points have been identified. It turned out that the quality of RF contacts of the tuning plates and the cooling capabilities of the stems were not sufficient. In recent years, the 4-Rod RFQ has been significantly improved in terms of high current acceleration at high duty cycle up to cw operation. These developments were driven by various projects such as MYRRHA, FRANZ or GSI-HLI. Novel cooling methods and technologies have been developed and experimentally validated to handle high thermal loads up to 100 kW/m. Especially the cooling of electrodes and stems has been improved. This was important to minimize the frequency shift during operation and the geometrical distortions due to inhomogeneous heating, respectively. For that reason, a new technology has been developed. Cooling channels are milled into the massive copper parts and filled with dielectric material. Then the copper parts are copper plated with a very thick layer. Finally the dielectric material is removed. As a result, a 3-dimensional structure of optimized cooling channels can be obtained. Figure II.12 shows the geometry of a stem, an electrode and the tuning plates with optimized cooling channels. Another important topic is the design of the RF contacts between tuning plates and stems.

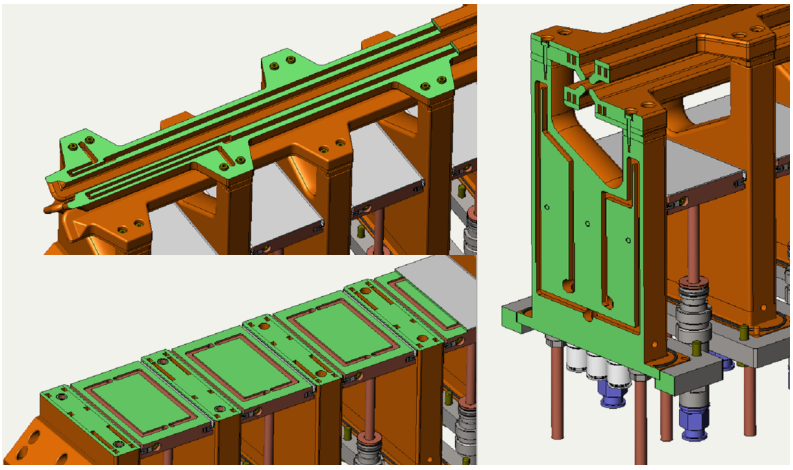

Figure II.12: *Optimized cooling channels of the HBS 4-Rod RFQ.*

Formerly, RF spring contacts have been used. But it turned out that the current density is sometimes too high for spring contacts. For the new generation of high power 4-Rod RFQs, massive silver plates are used. The required pressure between plates and stems is provided by special shaped shims. As material for the vacuum tank aluminum with 5 cm thickness will be used. The main advantages are the higher thermal conductivity and the possibility to dispense with copper plating of the whole inner tank surface because of the very small fraction of RF losses.
Another concern is the dipole component which is in general present in the 4-Rod RFQ. The center of an ideal quadrupole is field-free. The dipole component is the result of an asymmetrical quadrupole in which the field free region and therefore the position of the beam axis is shifted. The voltage between the electrodes of a 4-Rod-RFQ depends on the length of the current paths since the RFQ RF cells are $\lambda/4$-resonators. The current path for the upper electrodes is higher compared to the lower electrodes resulting in a different potential for lower and upper electrodes (see Fig. II.13). The dipole component should be as small as possible because the resulting shift of the beam axis increases higher order field components to the beam because of the non-hyperbolic profile of the electrodes. This dipole component can reach more than 20 % of the quadrupole field strength. The most common method for the compensation of the dipole component is the stem cutting. This involves the

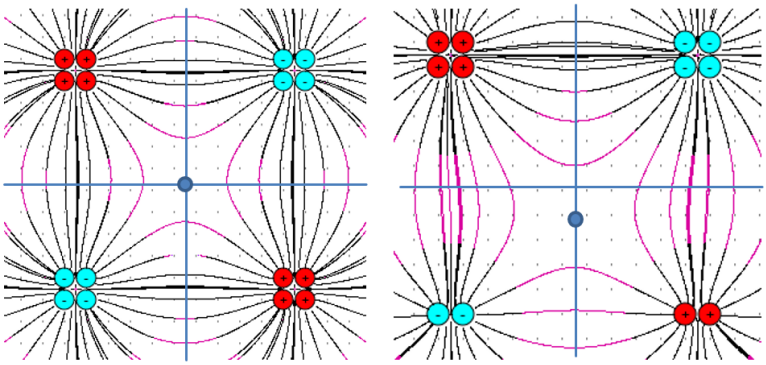

Figure II.13: Influence of the dipole component on the position of the beam axis.

variation of the angle of the cut between the mountings for the upper and the lower electrode of one stem. The disadvantage of this method is that the sharpness of the angle is limited. Once the angle gets smaller the range of the tuning plates decreases. Also the design of the cooling channels inside the stems are more complicated with a larger stem cut. RF simulations with MICROWAVE STUDIO have shown that the dipole component can be almost completely compensated or even over-compensated by widening the stems alternately so that the current path of the lower electrodes is increased (see Fig. II.14). This new method of dipole compensation was realized for the time

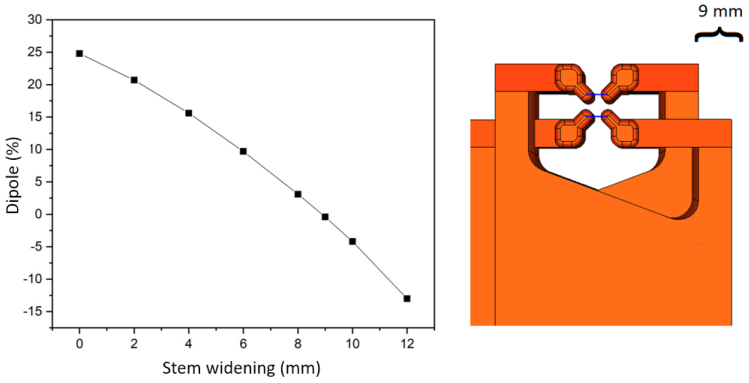

Figure II.14: Dipole component as function of the stem widening.

within the development of the MYRRHA-RFQ. RF measurements have validated that the method can compensate the dipole component in 4-Rod RFQs for the first time without having a negative impact on mechanical, thermal or RF properties [KKL^{+}18].

The MYRRHA RFQ was the first RFQ which has been developed using the new design approach for high power 4-Rod RFQs. The HBS-RFQ will have exact the same RF structure as MYRRHA. Figure II.15 shows the RFQ-structure of the MYRRHA-RFQ and the installation of the RFQ for the high power and beam tests. Essential differences are in the electrode modulation due to changed beam parameters as well as in the length of the structure. However, this has no significant influence on efficiency and frequency.

An important aspect is the transition energy between the RFQ and the drift tube Linac. This should be

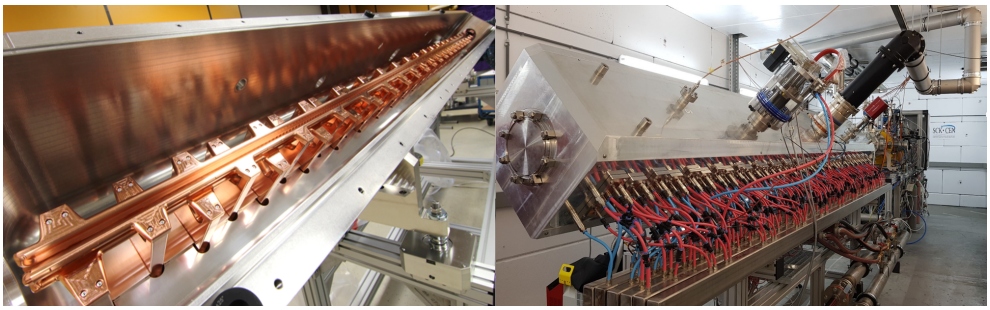

Figure II.15: RF structure of the MYRRHA RFQ (left) and installation of the RFQ for high power and beam tests (right).

high enough to enable a good beam transport along the subsequent Medium Energy Beam Transfer (MEBT). For a current of 100 mA, values between 2 and 3 MeV are a good choice. The exact value must be determined using beam dynamics simulations. For energies above 2 MeV, the length of the RFQ reaches a value that makes production and tuning considerably more difficult. In addition, the required power is then very high requiring a very large amplifier. Therefore, it is planned to divide the RFQ into two independently phased structures. In addition, a short MEBT (MEBT-1) is then used between the individual RFQ accelerators to match the beam from one RFQ to the other. Simulations showed that an electrode voltage of 85 kV is a good choice. With the expected shunt impedance of 72 kΩm, this corresponds to a specific RF peak power of 100 kW/m. The maximal thermal load is 25 kW/m with an RF duty cycle of 25 % which is comparable to the MYRRHA RFQ. This value is considered to be safe since the MYRRHA RFQ has been tested with 145 kW (36 kW/m) in cw operation without any problems [GBD+21] and a prototype cavity has reached even power levels of more than 100 kW/m (cw).
The lengths of the two RFQ-structures have been determined by beam dynamics simulations. It turned out that an output energy of about 1.25 MeV for the first RFQ is reasonable for the beam transport in MEBT-1. The second RFQ delivers a beam energy of 2.5 MeV. The length of the first RFQ is 3.64 m and 3.28 m for the second RFQ, respectively. The shunt impedance of 72 kΩm and the electrode voltage of 85 kV lead to RF power losses of 370 kW and 330 kW. The required RF power including the beam loading is about 500 kW and 460 kW, respectively. To keep the frequency constant during operation, each RFQ is equipped with a dynamic tuner that can influence the fields inside the resonator and thus adjust the frequency. Figure II.16 shows a sketch of a dynamic Tuner and its main components on the left and the tuner in the MYRRHA RFQ on the right. Figure II.17 shows the two RFQ structures with matching sections (MEBT-1/2) in between.

II.3.2 RFQ Beam Dynamics

The beam dynamics in an RFQ is determined by its electrode geometry. The alternating field on the electrodes leads to a transverse focusing of the particles with constant velocity. In order to accelerate and to bunch particles, electric fields in longitudinal direction are required. Therefore, a sinusoidal shape (sometimes trapezoidal), the modulation, is applied on the electrodes causing this longitudinal field component. This shape can be described by the aperture a and the modulation factor m (see Fig. II.9). The aperture is the minimum distance of the electrodes to the beam axis. The maximum distance to the beam axis is a·m. The ratio between the maximum and the minimum distance is called modulation parameter m. m=1 means there is no modulation. The length of an accelerating cell is defined a distance between a minimum and the following maximum of the modulated electrode. Corresponding to the required Wideröe condition, the cell length is correlated to the particle velocity.

Figure II.16: *Left: Overview of the component of a dynamic tuner. Right: Dynamic tuner inside of the MYRRHA RFQ.*

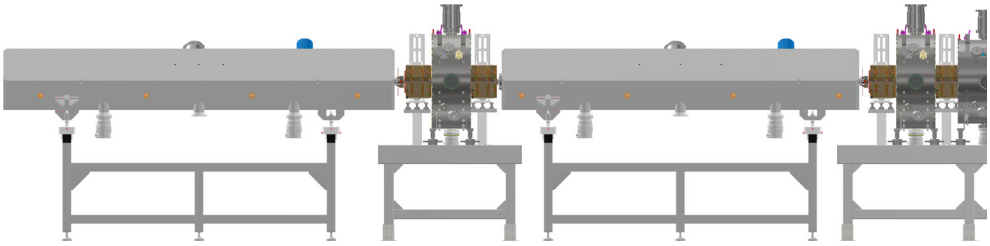

Figure II.17: *View of the 2 RFQ-structures with matching sections (MEBT-1/2).*

To overcome strong space charge effects, a high inter-vane voltage is preferred, but this is not favorable for achieving high reliability especially with high duty cycle or longer RF pulsed. Therefore, to increase the duty cycle will also bring space charge challenges, but indirectly. The design of the HBS RFQ is based on the work and experience of recent years to develop unconventional beam physics concepts and new techniques developed to realize efficient high current RFQs with high beam quality [Zha22].
There are different approaches to design RFQ structures depending on different boundary conditions. Two of them are already well known:

- The Four-Section Procedure (FSP), which was developed by LANL on the basis of neglecting space charge forces.
- The Equipartitioning Procedure (EP), which aims to minimize space-charge-induced emittance growth by avoiding longitudinal-transverse coupling.

Allowing emittance transfer, two different approaches are being proposed:

- The MEGLET (Minimizing Emittance Growth via Low Emittance Transfer) approach tries to hold the ratio of longitudinal emittance to transverse emittance in the range of 0.9–1.4 for keeping the emittance transfer at low levels and to use two emittance-transfer periods (in which the emittance transfer is in opposite directions) for achieving almost zero net emittance growth.
- The SEGLER (Small Emittance Growth at Larger Emittance Ratios) approach is another solution for achieving small emittance growth when a larger emittance ratio (beyond the optimum range required for MEGLET) is inevitable due to some given conditions.

For using the MEGLET approach, one needs to hold the emittance ratio inside the optimum range i.e. $0.9 \leqslant \epsilon_l/\epsilon_t \leqslant 1.4$. At given conditions, which kind of ϵ_l/ϵ_t values can be achieved is determined by the bunching process. Generally speaking, the RFQ bunching needs to achieve the following goals:

- To capture as many particles as possible and reduce the beam phase spread to a suitable value for efficient acceleration e.g. $\pm 30^\circ$.
- To minimize energy spread during the bunching.
- To avoid a too long structure for the bunching.

In a linac beam bunch, the particles perform synchrotron oscillations with respect to the synchronous particle. Such oscillations can be described using the well known following equations:

$$\frac{d}{ds}\Delta\varphi_{i,s} = \omega\left(\frac{dt_i}{ds} - \frac{dt_s}{ds}\right) = \frac{\omega}{c}\left(\frac{1}{\beta_i} - \frac{1}{\beta_s}\right) \approx -\frac{\omega}{\beta_s c}\frac{\Delta\beta_{i,s}}{\beta_s} = -\frac{\omega\Delta W_{i,s}}{m_0 c^3 \beta_s^3 \gamma_s^3} \tag{II.2}$$

$$\frac{d}{ds}\Delta W_{i,s} = qE_0T(\cos\varphi_i - \cos\varphi_s) \tag{II.3}$$

If a minimum energy spread is required, the change in $\Delta W_{i,s}$ should be small (like for adiabatic bunching). In this case, the variation of $\Delta\varphi_{i,s}$ is inversely proportional to $\beta_s^3\gamma_s^3$. For RFQs with $\gamma \approx 1$, the length of such a bunching section is proportional to β_s^3. In addition, the length of a bunching cell is longer at a higher β_{in}. Clearly, a lower W_{in} is usually more favorable to avoid a too long structure for bunching. If a high beam current is needed for an RFQ, however, usually one should also have a high W_{in} because of space charge forces being lower at higher energies. The formula for the space-charge electric field limits in ion sources is known as the Child-Langmuir law. For a planar electrode geometry with a gap spacing d between the two plates and an applied voltage U_0, the limiting current density J is determined by:

$$J = 1.67 \cdot 10^{-3}\left(\frac{q}{m_0c^2}\right)^{1/2}\left(\frac{U_0^{3/2}}{d^2}\right) \tag{II.4}$$

where q and m_0 are the charge and mass of the particle, respectively, and c is the speed of light in vacuum (all in MKS units). Applying Eq. (2-38) to a round uniform beam emitted from a circular area with radius r_s, one gets the beam current limit due to space charge as follows:

$$I = 1.67\pi \cdot 10^{-3}\left(\frac{q}{m_0c^2}\right)^{1/2} U_0^{3/2}\left(\frac{r_s}{d^2}\right) \tag{II.5}$$

Equation II.5 implies that W_{in} is a limiting factor for increasing I_{in}. Besides the above-mentioned factors, many other parameters e.g. the input emittance, the intervane voltage, the resonant frequency, and the required RFQ structure length can also influence the bunching quality and the length of the bunching section. In reality, therefore, one needs often to make trade-offs in choosing the design parameters for an RFQ accelerator and it is possible to reach larger emittance ratios, which are beyond the optimum ϵ_l/ϵ_t range required by the MEGLET method. Figure II.18 shows the Hofmann charts for the emittance ratios ϵ_l/ϵ_t larger than 2. Due to the remarkable $\sigma_l/\sigma_t = 1$ resonance peak, the "safe rectangle" used by the MEGLET method is not available any more. On these $2.0 \leqslant \epsilon_l/\epsilon_t \leqslant 4.0$ Hofmann charts, however, a relatively large safe area for tune footprints (see the 1/4 ellipse marked in orange in figure II.18) can be still found. The semi axes of this "safe 1/4 ellipse" cover the σ_l/σ_t ratio between [0,1] and σ/σ_0 ratio between [0.25,1] so the area of the "safe 1/4 ellipse" is smaller than that of the "safe rectangle". With several resonance peaks inside, this "safe 1/4 ellipse" is also not as clean as the "safe rectangle". Nevertheless, the most remarkable $\sigma_l/\sigma_t = 0.5$ resonance peak is fortunately relatively weak, so to use this area is a good compromise for achieving small emittance

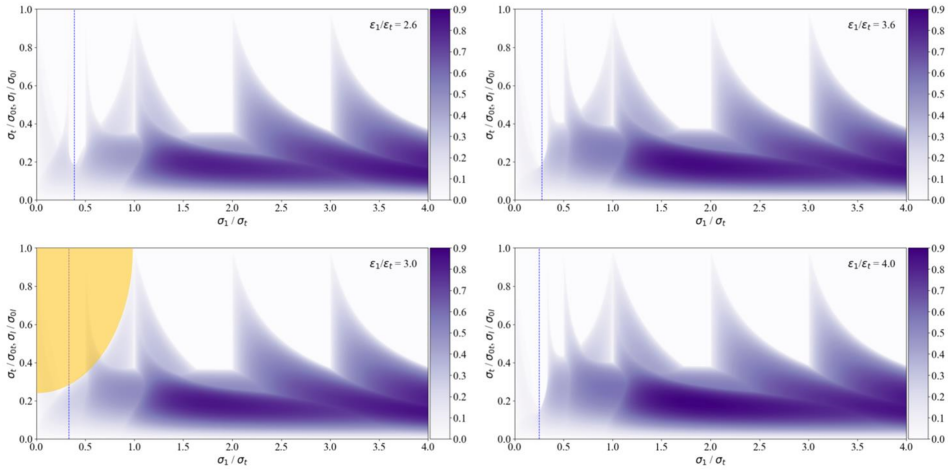

Figure II.18: *Hofmann charts for larger ϵ_l/ϵ_t ratios. The 1/4 ellipse marked in orange covers a relatively safe area for tune footprints.*

growth at larger emittance ratios $2.0 \leqslant \epsilon_l/\epsilon_t \leqslant 4.0$. This method is therefore named as "SEGLER" (Small Emittance Growth at Larger Emittance Ratios). When applying the SEGLER method, it is important to keep $\sigma_l/\sigma_t \leqslant 1.0$, which means that the longitudinal focusing strength should be smaller than the transverse one. One can tune different dynamics parameters to realize this. For example, a smaller electrode modulation can provide larger transverse electric field components and smaller longitudinal electric-field components. This method has been applied for the redesign of the FRANZ (Frankfurt Neutron Source at the Stern-Gerlach-Zentrum) RFQ and for the design of the HBS RFQs. The following list shows the main considerations behind the design of the HBS RFQ-accelerators.

- With some safety margins, the design current I_{in} and the design input emittance $\epsilon_{\text{in,t,n,rms}}$ have been chosen as 105 mA and as 0.4 π mm mrad, respectively.
- Compared to the 5 mA MYRRHA RFQ, the 105 mA HBS RFQ will need to use much higher beam energies both at the input (according to the Child-Langmuir law) and at the output (for an injection into the DTL part with less strong space charge effects). Therefore, these two values were taken as 100 keV and 2.5 MeV, respectively.
- To benefit from IAP's extensive expertise in the 4-Rod RFQ development over decades, the 4-Rod structure typically operating at about 200 MHz was adopted.
- Due to the good experience with the design, construction, and operation of the MYRRHA RFQ and its reasonable shunt impedance (measured value) 73 kΩm, the same frequency i.e. 176.1 MHz has been adopted.
- For ensuring a reliable operation at the RF duty cycle of up to 25 %, the inter-vane voltage of the HBS RFQ has been conservatively chosen as U = 85 kV in order to keep the Kilpatrick factor lower than 1.8, a safe value proven by the LEDA experiments for CW operation.
- Based on all above-mentioned choices, the estimated length of the HBS RFQ would be much longer than 4 m. To avoid demanding RF tuning and a large power amplifier, it was decided to develop a MUSIC-style RFQ (two cavities with an MEBT in between) for the HBS project. The MEBT can also provide free parameter for some operational flexibilities and matching.

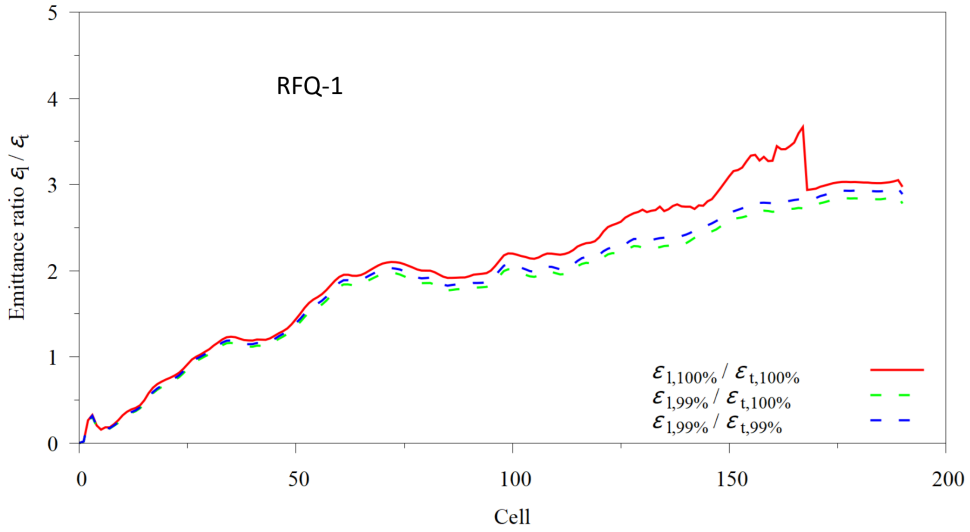

Figure II.19: *Evolution of emittance ratio along RFQ-1.*

As mentioned earlier, the SEGLER method was used for the design of the HBS RFQs. Figure II.19 shows that the emittance ratio is about 2.0 after the pre-bunching and about 3.0 at the exit of RFQ-1. The average emittance ratio for the main part of the RFQ is 2.5. On the Hofmann chart for ϵ_l/ϵ_t=2.5 the tune footprints of the HBS RFQ Cavity-1 have been confined inside the "safe 1/4 ellipse" as required by the SEGLER method (Fig. II.20). As the "safe 1/4 ellipse" is not as clean as the "safe rectangle" (parts of the $\sigma_l/\sigma_t = 1/2$ and $\sigma_l/\sigma_t = 1/3$ resonance peaks are inside), the tune trajectories especially the longitudinal one touched the two resonance peaks and some emittance growths occurred. The

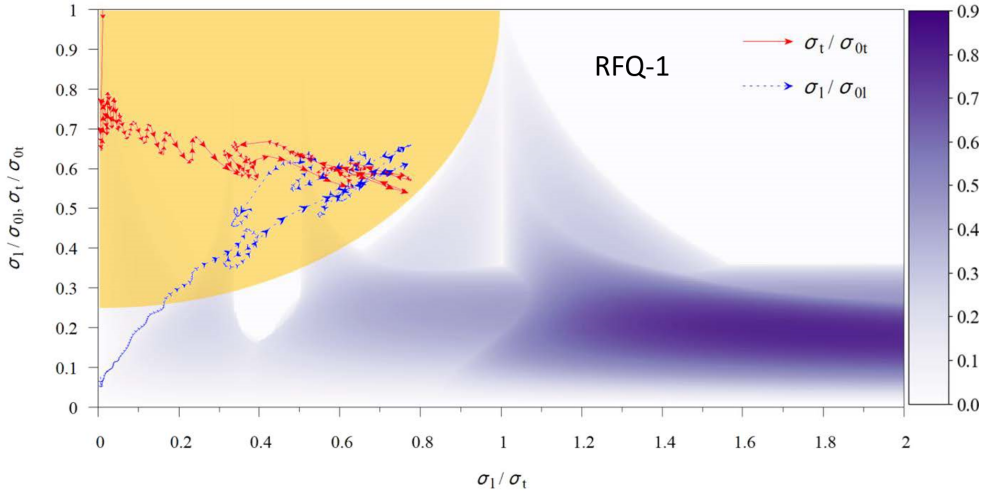

Figure II.20: *Tune chart for RFQ-1 (overlapped with the Hofmann chart for* $\epsilon_l/\epsilon_t = 2.5$.

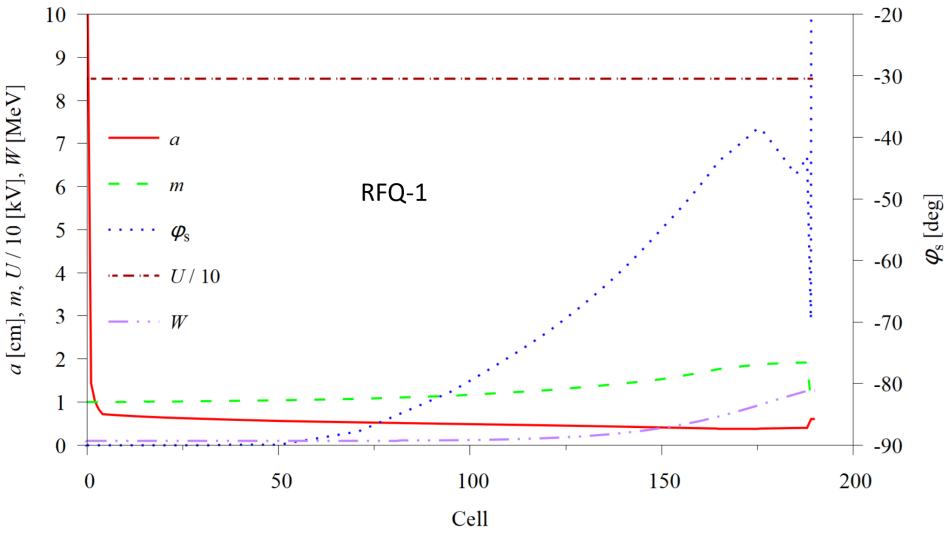

Figure II.21: *Parameters of RFQ-1 as function of the cell number.*

output particle distribution of RFQ-1 is still concentrated (see Fig. II.25). The Medium Energy Beam Transfer (MEBT-1) gives the possibility to handle this beam and to match it into the acceptance of RFQ-2. Figure II.21 shows the parameters of RFQ-1 as function of the cell number.

The design of the HBS RFQ-2 is still based on the SEGLER method. The $\sigma_l/\sigma_t = 1/3$ resonance peak vanishes gradually from ϵ_l/ϵ_t=2.0 to ϵ_l/ϵ_t=3.0. Therefore, the tune trajectories of the HBS RFQ-2 only touched the $\sigma_l/\sigma_t = 1/2$ resonance peak very shortly (see Fig. II.22). Figure II.23 shows the

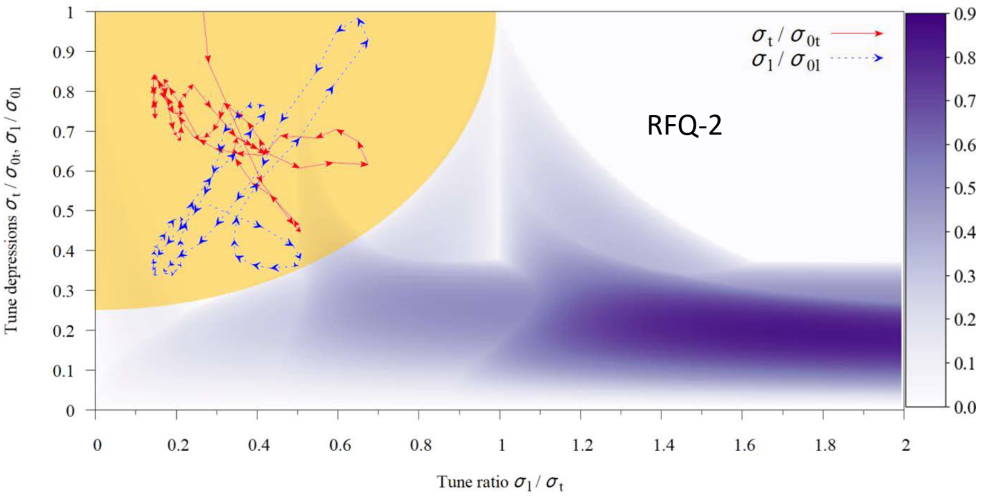

Figure II.22: *Tune chart for RFQ-2 (overlapped with the Hofmann chart for* $\epsilon_l/\epsilon_t = 3.0$.

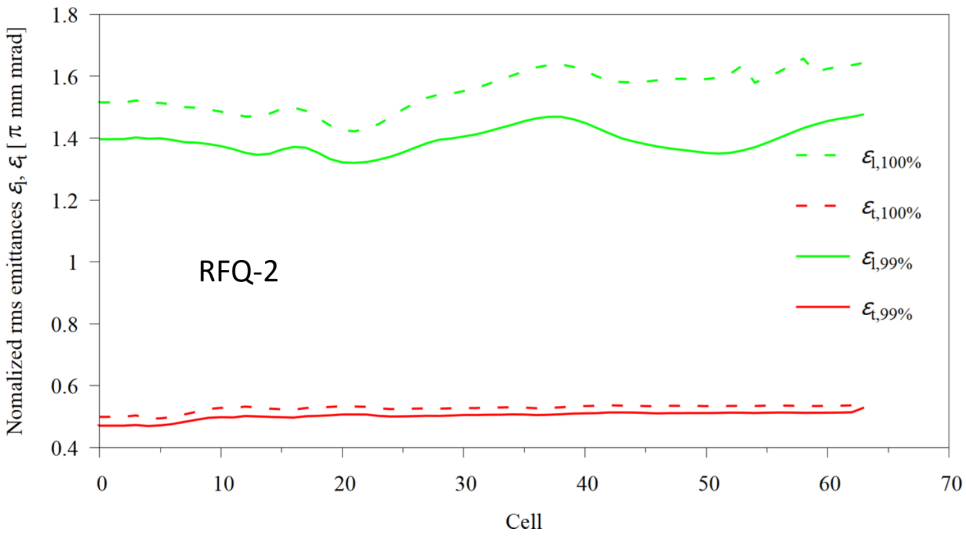

Figure II.23: *Evolution of emittance along RFQ-2.*

emittance evolution along RFQ-2. It can be seen that all emittance curves are quite flat and the emittance ratio is about 3.0 throughout RFQ-2. Figure II.24 shows an overview of the parameters of the RFQ-2 as function of the cell number.

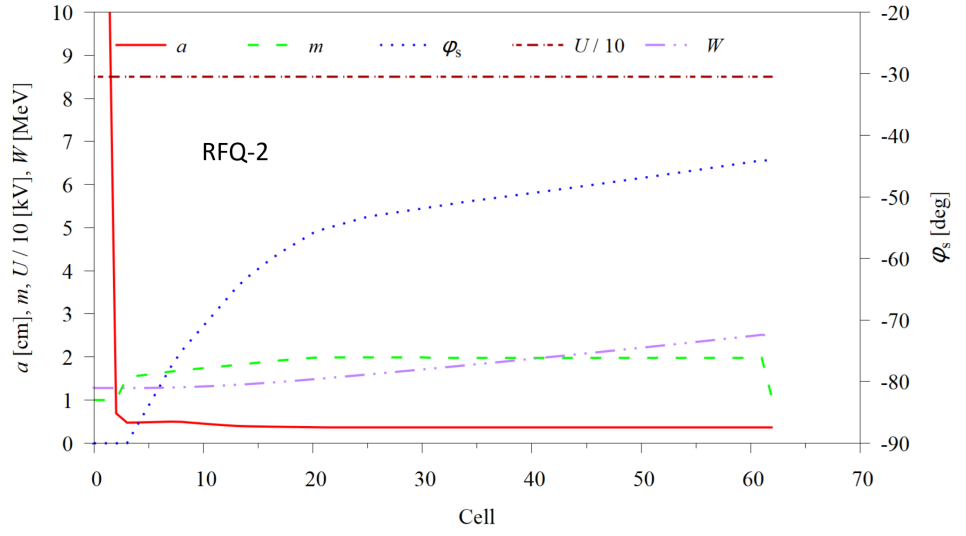

Figure II.24: *Parameters of RFQ-2 as function of the cell number.*

Table II.2 summarizes the parameters of the two RFQ accelerators.

Parameter	RFQ1	RFQ2	Unit
RF Structure	4-Rod	4-Rod	N/A
Frequency	176.1	176.1	MHz
Particles	protons	protons	NA
Beam current (real/sim)	100/105	100/105	mA
RF Duty factor (max)	25	25	%
E_{in}	100	1272	keV
E_{out}	1.272	2.5	MeV
R_p	72	72	kΩm
RF losses	360	330	kW
Specific power loss	100	100	kW/m
Thermal load (max)	25	25	kW/m
Beam power	117	125	kW
RF losses (peak)	361	330	kW
Total peak power	478	455	kW
Amplifier power	600	600	kW
Electrode voltage	85	85	kV
Kilpatrick factor	1.51	1.51	N/A
Length	3.60	3.28	m
$\epsilon_{t,out,n,rms}$	0.46	0.56	π mm mrad
$\epsilon_{l,out,n,rms}$	0.27	0.33	π MeV deg
Transmission (sim.)	99.83	98.6	%

Table II.2: *Parameters of RFQ 1+2.*

II.4 Medium Energy Beam Transfer

M. Droba, H. Podlech, S. Reimann, M. Schwarz

There are two Medium Energy Beam Transfer (MEBT) sections in the HBS-Linac. The first one (MEBT-1) matches the beam from the first RFQ into the acceptance of the second RFQ. The second section (MEBT-2) is used for matching the beam into the acceptance of the drift tube Linac (DTL).

II.4.1 MEBT-1

The Medium Energy Beam Transfer Line 1 (MEBT-1) provides beam matching of emittance after RFQ-1 into the acceptance of the RFQ-2 at a proton energy of $1.272\,\mathrm{MeV}$. Because of high current condition (I=104.8 mA) and beam emittance size in both transversal and longitudinal planes after passing of the RFQ-1 (projections of the phase space particle distribution are shown in Fig. II.25), it should be very compact.

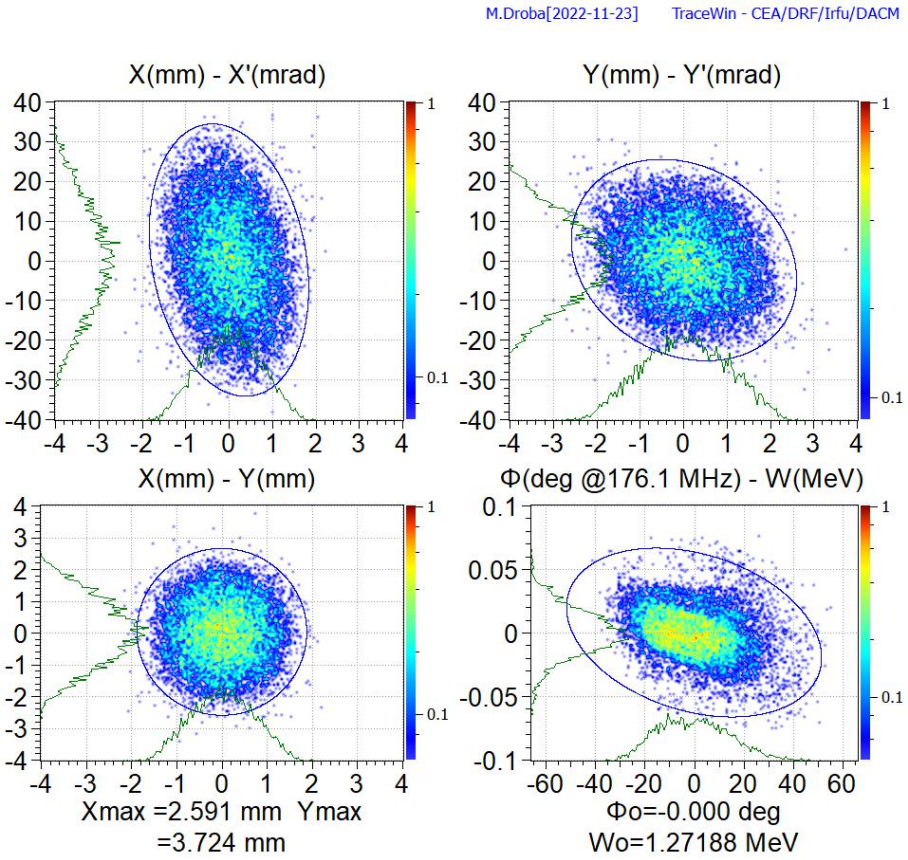

Figure II.25: *Simulated RFQ1-Output phase space.*

Difficulties in technical realisation of focusing and rebunching devices, especially in a first half of the MEBT-1-beamline, will present challenges in order to meet design parameters and to avoid beam degradation.

II.4.2 Resulting Design

The optimum design consists of two magnetic quadrupole triplets (QT1, QT2) for transversal beam focusing and 1 re-bunching RF-cavity (CH-type) for longitudinal phase space handling. Multi-particle beam transport simulation were done with a simulation tool TraceWin [UDP22] and beam projections are shown through the whole MEBT-1 in Fig. II.26. Length of the whole beam line is L=1.03 m.

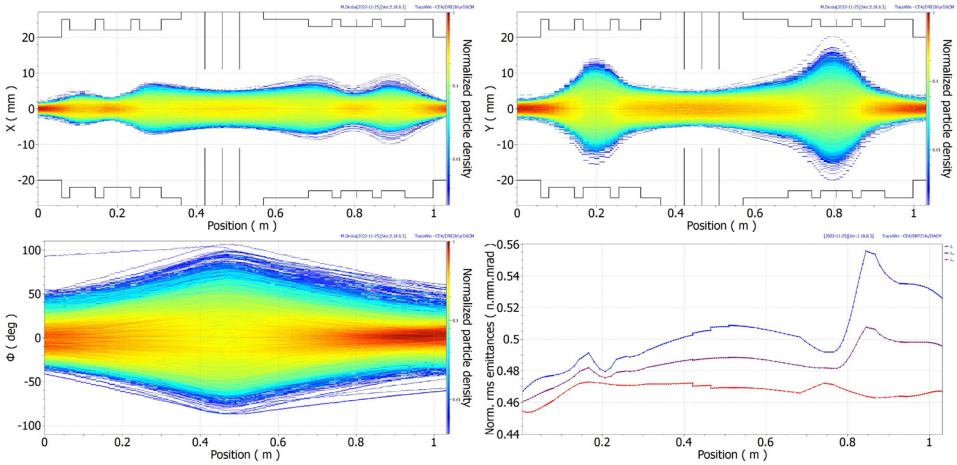

Figure II.26: Simulated beam transport along MEBT-1 with given parameter.

The simulation started at the inner wall of the RFQ-1 and finished at inner wall of the RFQ-2. The geometrical aperture is shown by a black line. The longitudinal re-bunching of the proton bunch in 3-gap-cavity was calculated by a thin gap approximation, the centers of the RF-gaps are depicted by three vertical lines. The first quadrupole triplet (QT1) is positioned 80 mm beam upwards from the starting point, behind inner wall of the RFQ1, and will be equipped with a beam position monitor (BPM). The QT1 will have an optimized design with a pole tip magnetic field not exceeding $B \leqslant 1\,\mathrm{T}$, with a variable pole lengths. Vanadium Permendur will be used as magnetic material. Main parameters are given in the table II.3.

QT1			
Gradient / (T/m)	Pole length / mm	Radius / mm	Pole-tip magnetic field / T
+43.5	64.5	22	0.957
−44.02	68	22	0.968
+32.89	55	22	0.724
QT2			
+23.83	60.0	22	0.524
−33.21	80.0	22	0.73
+37.88	60.0	22	0.83

Table II.3: Main parameters of the QT1 and QT2. Longitudinal distance between poles is 22 mm.

The re-bunching cavity of the CH-type has 3 gaps, operating at f=176.1 MHz with a power consumption of about 40 kW. Main parameters of the cavity are given in Tab.II.4. The first gap of the cavity is

Re-buncher 1				
Gap Nr.	$\beta\lambda/2$ / mm	Aperture / mm	phase / °	eff. gap voltage E_0TL / kV
1.	44.3	22	−90.0	38.9
2.	44.3	22	−90.0	71.2
3.	44.3	22	−90.0	38.9

Table II.4: Main parameters of the re-buncher1.

positioned Δz = 110 mm behind QT1. There is the possibility of fine tuning of the gap voltage and of the RF-phase to optimize longitudinal beam parameters for the injection into the RFQ-2. The QT2 will have less extreme parameters (pole tip field, length, construction). The position is flexible in some distance and could be adjusted in ± 1 cm interval along beam axis, to reach optimum injection into RFQ-2 in transversal planes.

The power consumption is supposed to be 20 kW for both triplets. Additionally, two x,y-window-frame-steerer for beam offsets compensation and diagnostics elements (2xBPMs, 1xBCT) will be used. The first steerer will be integrated in the tank wall of RFQ1 and will be able to compensate up

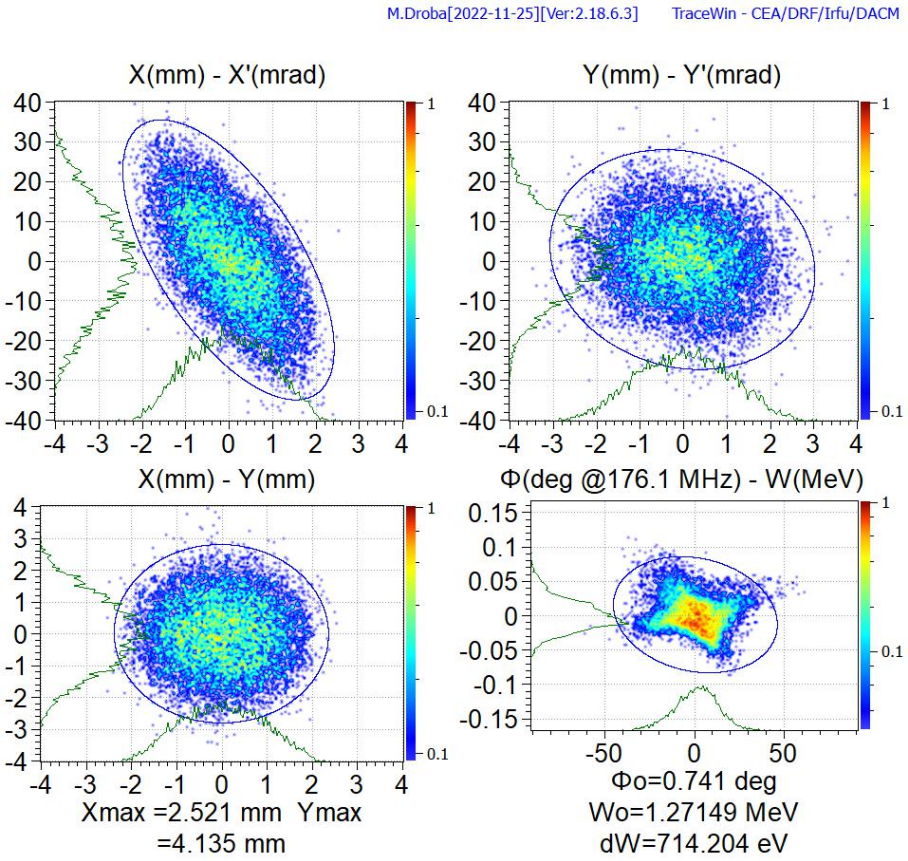

Figure II.27: Calculated MEBT-1-Output phase space distribution.

to $\Delta x\prime, \Delta y\prime = \pm 5$ mrad of the transversal momentum offsets. The second steerer will be placed just in front of QT2. Both steerer will have a length of 20 mm. Simulation showed moderate emittance

Emittance	Input Value	Output Value
$\epsilon_{rms,n,x}$	0.454 mm mrad	0.467 mm mrad (+2.9 %)
$\epsilon_{rms,n,y}$	0.467 mm mrad	0.526 mm mrad (+12.6 %)
$\epsilon_{rms,E}$	4.26 keV ns	4.73 keV ns (+11.1 %)

Table II.5: *Input and output emittance values.*

growth as listed in Tab.II.5. The particle phase space projections at the end of the MEBT-1 are shown in Fig. II.27.

II.4.3 MEBT-2

The proton beam energy after passing RFQ-2 was set to W=2.52 MeV and the simulated beam current is I=103.53 mA. The main task of MEBT-2 is matching of the beam parameters into the ac-

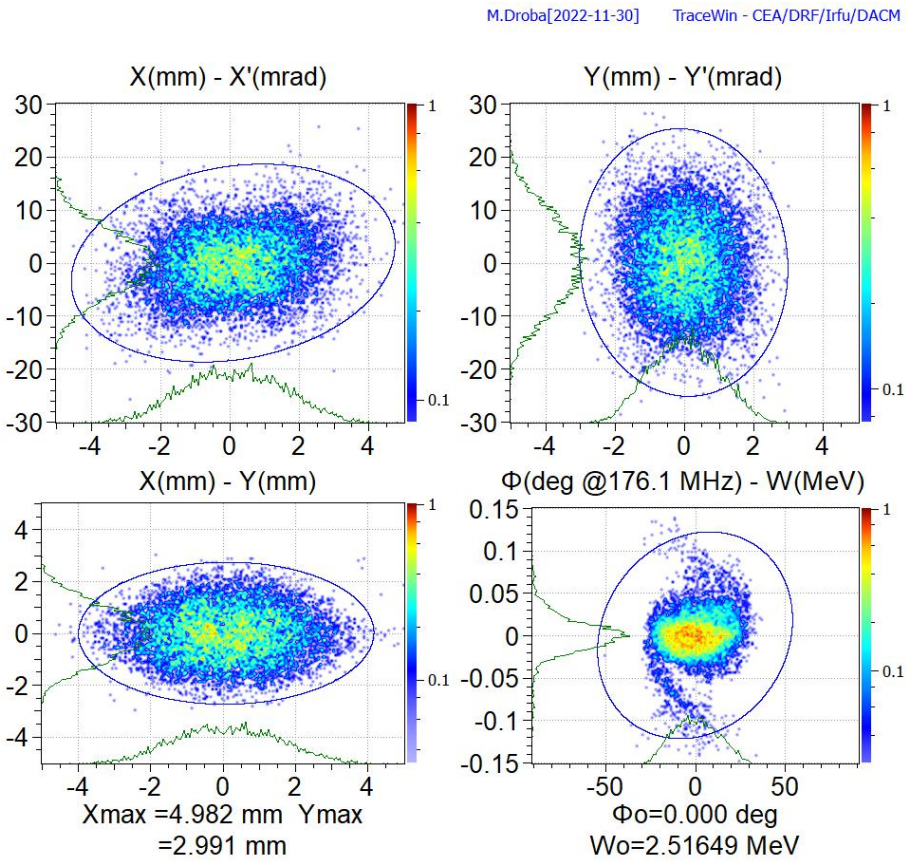

Figure II.28: *Calculated MEBT-2-Input phase space distribution.*

ceptance of the following drift tube linac (DTL) section. The following linac requires a convergent beam in both transverse planes, while the RFQ provides a beam convergent in one plane and divergent in the other one (Fig. II.28). The transverse matching is done by means of magnetic quadrupole triplets (QT3, QT4). In addition, the beam must be longitudinally matched to reduce the phase width, otherwise nonlinear effects in the subsequent drift tube cavities lead to emittance growth and possibly uncontrolled particle losses. To minimize phase width of the proton bunch, re-buncher2 is used in the present design. It will operate at rf-frequency f=176.1 MHz and synchronous phase of $\varphi_s = -90^\circ$. The MEBT2 was designed in such a way, that there is sufficient free space for various beam diagnostic elements (BPM, ACCT). The design is similar to the MEBT-1 with 2 quadrupole triplets, 1 rf-cavity, 2 steerer and diagnostics with overall length of L=1.39 m. The MEBT-2 ends direct behind QT4, where the beam emittance is matched into the acceptance of the following DTL-section. Field strengths, element size, the distance between the elements and construction are more relaxed as in a case of MEBT-1. Overall 50 kW electric power consumption is planned.

II.4.4 Resulting Design

Multi-particle beam transport simulations through the whole MEBT-2 were performed with simulation tool TraceWin [UDP22] and results are shown in Fig. II.29. The simulation started at the inner wall of the RFQ-2 and finished immediately behind the QT4. The geometrical aperture is shown by a black line. The first quadrupole triplet (QT3) is positioned 252 mm upwards from the starting point, behind inner wall of the RFQ-2. The QT3 and QT4 will have standard and equal design with a pole tip magnetic field not exceeding $B \leqslant 0.8$ T, with a constant pole lengths. Main parameters for both quadrupole triplets (QT3, QT4) are given in Table II.6.

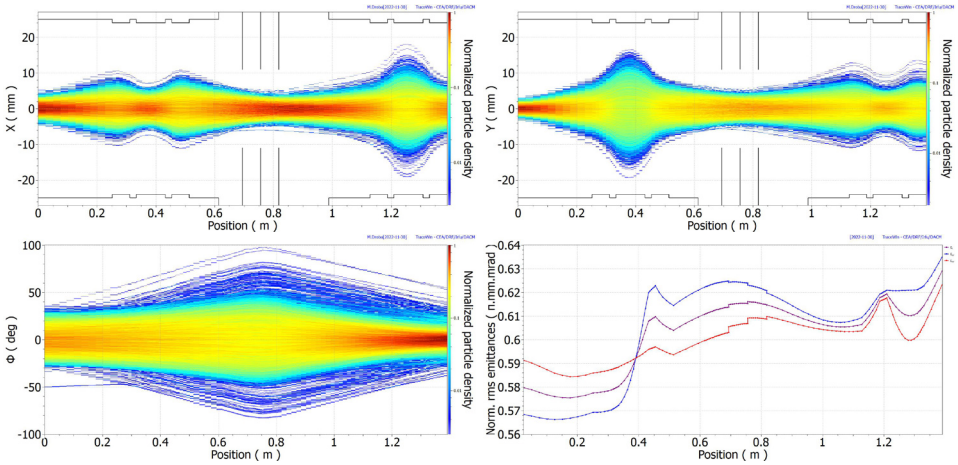

Figure II.29: *Calculated beam transport along MEBT-2 with given parameter.*

The power consumption is supposed to be 20 kW for both triplets. The re-bunching cavity-2 will be of the CH-type with 3 gaps and power consumption of about 50 kW. Main parameters of the cavity are given in Tab.II.7. The first gap of the cavity is positioned Δz = 180 mm behind QT3. There is possibility of fine tuning of the gap voltage and of the RF-phase to optimize longitudinal beam parameters necessary for the injection into the following DTL section.

The position of all elements is flexible in some distance and could be adjusted in $\pm 1cm$ interval along beam axis, to reach optimum injection into the DTL-section, if necessary. Additionally, two x,y-window-frame-steerer for beam offsets compensation and diagnostics elements (2xBPMs, 1xBCT) will

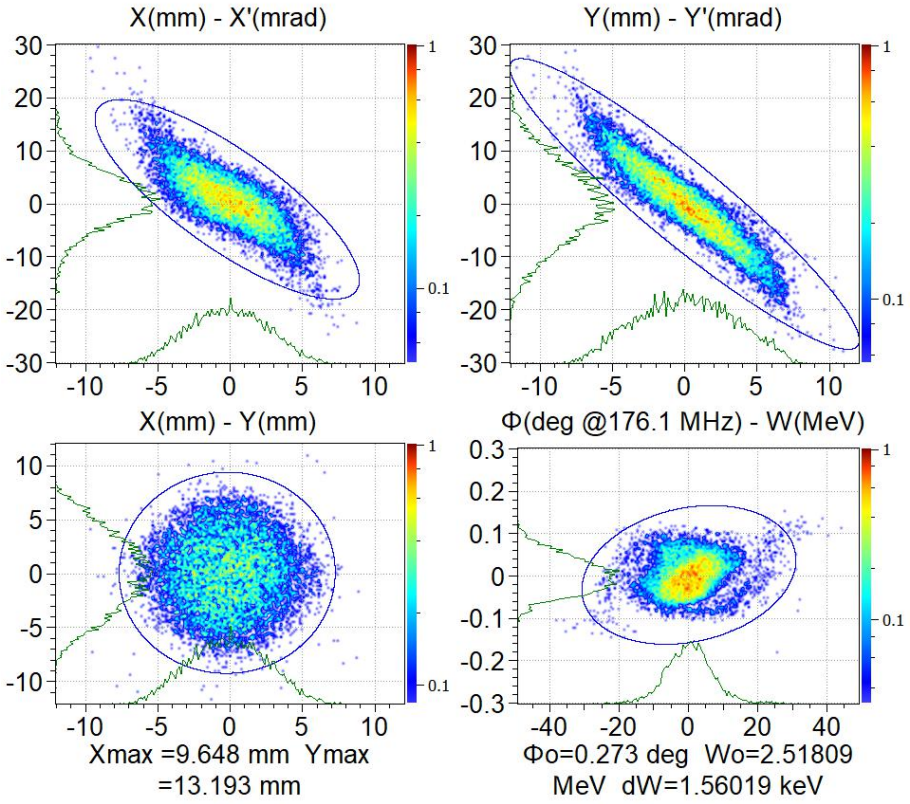

Figure II.30: Calculated MEBT-2-Output phase space distribution.

QT3			
Gradient / (T/m)	Pole length / mm	Radius / mm	Pole-tip magnetic field / T
+29.3	59.5	24	0.703
−30.1	99.0	24	0.722
+31.0	59.5	24	0.744
QT4			
−26.9	59.5	24	0.646
+28.2	99.0	24	0.677
−28.5	59.5	24	0.684

Table II.6: Main parameters of the QT3 and QT4. Longitudinal distance between poles is $22\,mm$.

be used. Similarly to the MEBT-1, first steerer will be integrated in the tank wall of the RFQ-2 and will be able to compensate up to $\Delta x\prime, \Delta y\prime = \pm 5$ mrad of the transversal momentum offsets. The second steerer will be placed just in front of QT4. Simulation showed small emittance growth as listed in

Re-buncher 2				
Gap Nr.	$\beta\lambda/2$ / mm	Aperture / mm	phase / °	eff. gap voltage E_0TL / kV
1.	62.2	22	−90.0	86.6
2.	62.2	22	−90.0	121.0
3.	62.2	22	−90.0	86.6

Table II.7: Main parameters of the re-buncher2.

Emittance	Input Value	Output Value
$\epsilon_{rms,n,\,x}$	0.591 mm mrad	0.623 mm mrad (+5.4 %)
$\epsilon_{rms,n,\,y}$	0.568 mm mrad	0.635 mm mrad (+11.8 %)
$\epsilon_{rms,\,E}$	5.2 keV ns	4.84 keV ns (−7 %)

Table II.8: Input and output emittance values.

Tab.II.8. The particle phase space projections at the end of the MEBT-2 are shown in Fig. II.30. The simulated particle distribution fit well in the acceptance of the following DTL-section.

III.

DRIFT TUBE LINAC

H. Podlech, K. Kümpel, S. Lamprecht, N. Petry, M. Schwarz

The Drift Tube Linac (DTL) has to accelerate the proton beam from 2.5 MeV to 70 MeV. The design of the DTL is a complex process between the beam dynamics and cavity design. There are a number of requirements or boundary conditions for the DTL with respect to beam dynamics. These include:

- RF frequency
- Beam current
- Required maximum duty cycle
- Minimum emittance growth
- Minimum particle losses

From the beam dynamics point of view, longitudinal drift distances (e.g. inter tank sections) should be as small as possible. On the other hand, there must be sufficient transverse focusing and space for beam diagnostics and assembly. The beam dynamics simulations initially make reasonable assumptions regarding the spacing, RF fields, gradients and voltages in each cavity. The design of the cavities incorporates these results of the beam dynamics simulations. Further boundary conditions such as maximum length of the cavities, peak fields, thermal load or maximum RF power have to be considered in the design of the cavities. This leads to an iterative process of optimization of beam dynamics, cavities and inter tank sections. For the cavities, the following boundary conditions have been identified:

- Maximum specific power loss: 120 kW/m
- Maximum specific thermal load: 30 kW/m
- Maximum cavity length: 1.6 m
- Maximum RF amplifier size per cavity: 500 kW

III.1 Beam Dynamics Concept

There are many different design concepts for developing the beam dynamics of Linacs. Probably the most common is the **constant-phase** approach, in which a constant design phase of for example $\varphi_s = -30^\circ$ is used at each gap within one multi-gap cavity (see Fig. III.1). This leads to gap center distances of $l = \frac{\beta\lambda}{2}$ with $\lambda = \frac{c}{f}$ being constant within one cavity and with the particle velocity $\beta = \frac{v}{c}$. The gap-to-gap distance thus increases successively with increasing particle velocity to ensure a constant synchronous phase.

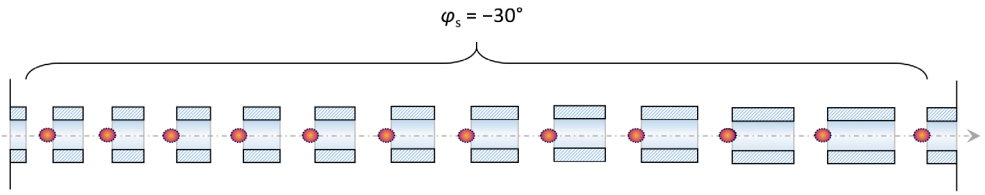

Figure III.1: *Schematic illustration of a constant-phase acceleration scheme showing a bunch in subsequent gaps, each at the time of the formation of the maximum electric field within the gap. The distance between the gap centers increases to ensure a constant synchronous phase φ_s while the bunch is accelerated.*

However, depending on the application, other concepts can be advantageous. This includes the three concepts KONUS[1], APF[2] and EQUUS[3].

KONUS is a beam dynamics concept for efficient acceleration with a minimum number of magnetic focusing elements. A KONUS section usually starts with a triplet lens and a short rebunching section around $\varphi_s = -35^\circ$, followed by the main multigap acceleration starting near a synchronous phase of $\varphi_s = 0^\circ$ with an excess energy compared to a hypothetical zero degree synchronous particle. Therefore, it moves towards more negative phases with each gap and the difference between the excess energy and the hypothetical reference energy for each gap decreases (see Fig. III.2). While KONUS and EQUUS have the similarity of the most negative phases at the start and end of the section, the gap center distance within a cavity changes for KONUS while it remains constant for EQUUS. Further details on KONUS and corresponding in-depth studies can be found in [RHT+19, TRP+08, Hä17].

APF [OMY+16, MRS99, YHOY04] uses its DTL cavities not only for longitudinal but also for transverse focusing and therefore gives the possibility to be operated without magnetic lenses which could save costs and reduce the linac length. It has been developed since the 1950's but has only been used to a limited extent due to a decisive feature and disadvantage: As the transverse focusing is (only) depending on the phase position of the particles (in contrast to the use of magnetic lenses for transverse focusing) there is a strong coupling between transverse and longitudinal motion. This inevitably leads to emittance growth (especially at low energies where the bunch usually has a larger phase width) and to a significantly reduced energy acceptance at the entrance of the respective cavity.

The **EQUUS** concept was first named and studied in detail in 2009 by Minaev et al. [MRP+09]. Prior to that, there were first approaches with multi-gap constant-β DTLs already in 1994 by R. von Hahn *et al.* [vGH+93] and in 1998 by H. Podlech *et al.* [PGvH+98, Pod99]. Even earlier in history, the Argonne Tandem Linac Accelerator System (ATLAS) at Argonne National Laboratory (ANL) in the USA can be considered as the origin of a cw-capable superconducting heavy ion linac [SZ83, Bol86, BPS+93].

[1] Acronym for ger. *Kombinierte Null Grad Struktur* (*Combined Zero Degree Structure*)
[2] Acronym for *Alternating Phase Focusing*
[3] Acronym for *Equidistant Multi-Gap Structure*

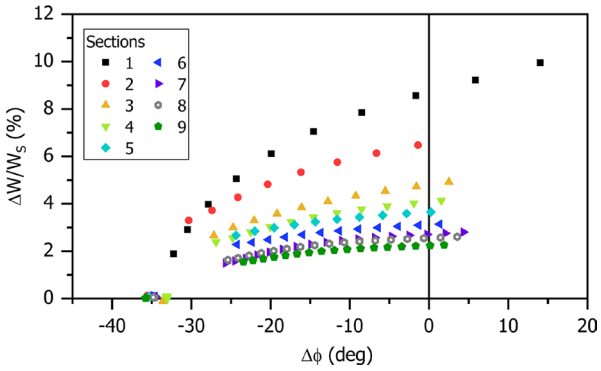

Figure III.2: *Exemplary bunch center motion of a KONUS design. [RHT+ 19]*

Superconducting split-ring resonators (3 gaps, constant-β design) were used here.
EQUUS features an efficient acceleration with some similarity to KONUS and special advantage for variable final energies. In contrast to KONUS, at EQUUS the beam is usually injected with an energy *deficiency*[4] at a synchronous phase of $\varphi_s \ll 0^\circ$ into the cavity (see Fig. III.3).

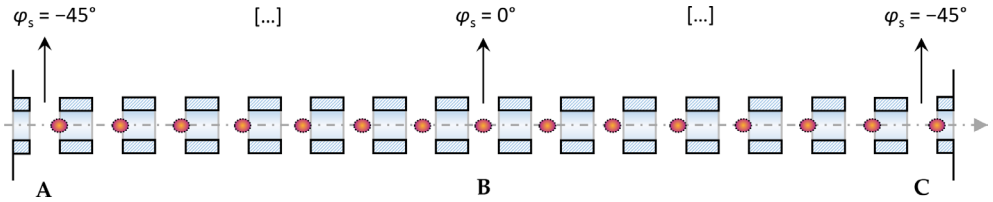

Figure III.3: *Schematic illustration of an EQUUS acceleration scheme with a bunch in subsequent gaps, each at the time of the formation of the maximum electric field within the gap. While the bunch crosses the center of the gap with $\varphi_s \ll 0^\circ$ for both the first (**A**) and the last gap (**C**) at the time of a rising E-field and therefore is depicted at the end of the gaps, the bunch is located within the middle of the cavity (**B**) in the center of the gap ($\varphi_s = 0^\circ$).*

The basic principle of the design can be described as follows:

- The beam is injected into the cavity with an energy deficiency of $-5\,\%$ to $-20\,\%$ to the reference energy of the cavity, defined by its geometrical parameters, namely the $\beta\lambda/2$ distance of neighboring gap centers. The value that is reasonably taken for the design depends, among other things, on the achievable gap voltage, the length of the cavity, the selected input synchronous phase (in the first gap) and the particle distribution. At the same time, the synchronous phase in the first gap is chosen within the range of about -55° to -25° ensuring longitudinal stability through the focusing effect in this phase region.
- Based on the previously selected parameters, the accelerated bunch now performs a sliding movement in the longitudinal phase space (Fig. III.4), as in KONUS partly, but starting in the third quadrant (see Fig. III.5) moving towards a positive synchronous phase direction near the coordinate system's origin. The acceleration efficiency increases with each gap, while the bunch is still slower than the reference particle. Finally, the synchronous phase approaches

[4] *energy deficiency* in relation to the cavity's design energy (also *reference energy*) defined by the gap center to gap center distance $\beta\lambda/2$. When $\beta\lambda/2$ is kept constant within a cavity, it is also called *constant-β cavity*.

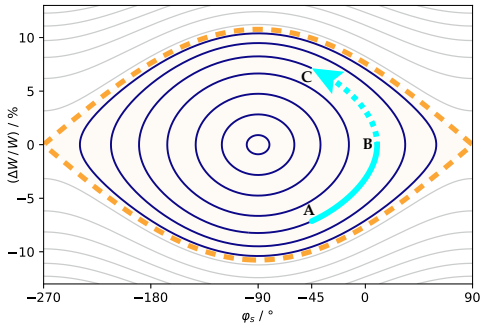

Figure III.4: *Schematic illustration of the typical movement of an accelerated bunch in an EQUUS-section in the longitudinal phase space. The stable region is within the dashed orange so-called Separatrix.*

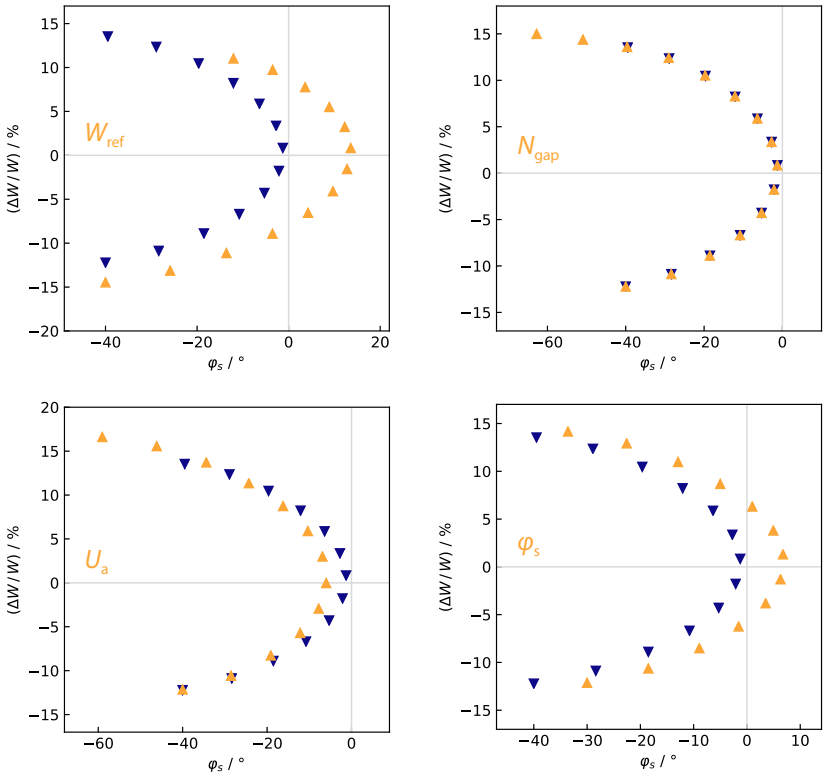

Figure III.5: *Exemplary variation of the four main equidistant structure design parameters reference energy W_{ref}, number of gaps N_{gap}, effective cavity voltage U_a and synchronous phase φ_s of the first gap.*

$\varphi_s \approx 0^\circ$ and the cavity's reference energy at the same time. The cavity could now end at this point and the beam could be extracted.

- It is also possible to accelerate the beam further in a cavity with enough gaps. In this case, the beam would become faster than the reference energy and with each gap slide back to more negative synchronous phases as it arrives earlier than the reference particle in each gap. This slightly lowers the acceleration efficiency again but ensures longitudinal stability one more time.

To increase the flexibility with this beam dynamics approach, the EQUUS movement can be split up on two separate cavities at the point where the reference energy of the cavity is reached, and the bunch continues to accelerate to higher energies and again to synchronous phases of $\varphi_s \ll 0^\circ$. In recent beam dynamics designs as for HELIAC at GSI (Darmstadt, Germany) both approaches have been used. Furthermore, the main structure design parameters for EQUUS are given in III.5.

III.1.1 Underlying Conditions

The HBS drift tube linac will accelerate the $100\,\mathrm{mA}$ proton beam coming out of the MEBT2 section with an initial energy of $2.5\,\mathrm{MeV}$ up to an end energy of $70\,\mathrm{MeV}$.
For a beam current of $100\,\mathrm{mA}$, the beam dynamics concept has to be handled with special care, as the occurrence of space charge forces that come with such a high current can lead to considerable emittance growth along the beam line. Therefore, one of the main challenges of the beam dynamics design is to keep the emittance growth as low as possible, while efficiently accelerating the beam.

Besides the required end energy, several boundary conditions have to be taken into account concerning the choice of the design parameters for the cavities and focusing elements. To ensure feasibility, the cavities should not be longer than $1.6\,\mathrm{m}$, which limits the possible number of gaps, especially for higher energies. The magnetic field strength of the focusing elements should not exceed $1.2\,\mathrm{T}$, also for reasons of feasibility. The RF power is provided by solid state amplifiers with a maximum output of $500\,\mathrm{kW}$. Assuming a safety margin of 20 % leaves $400 - 450\,\mathrm{kW}$ overall power available for each cavity.

The power required to accelerate the beam inside the cavity can be divided into two parts: the power loss P_L required to build up the electromagnetic fields inside the accelerating structure, and the energy used to actually accelerate the beam, which is called the beam load P_B. With an overall available power P_{ges} of $400\,\mathrm{kW}$ per cavity, the maximum achievable effective voltage $U_{\mathrm{eff}} = U_0 \cdot T$ for the structure is determined:

$$P_{\mathrm{ges}} = P_{\mathrm{L}} + P_{\mathrm{B}} = \frac{U_{\mathrm{eff}}^2}{R_{\mathrm{eff}}} + I \cdot U_{\mathrm{eff}} \cdot \cos\varphi_s, \tag{III.1}$$

with the effective voltage U_{eff}, the shunt impedance R_{eff} and the beam current I.

While for low current accelerators beam loading does not play an important role for the power calculation, for a beam current of $100\,\mathrm{mA}$ it is an considerable amount of power that goes into beam acceleration, limiting the electric field strength that can be achieved with a certain amount of power.

Another important observation that needs to be considered is that at low energies, the phase spread of the beam after an accelerating cavity grows to an extend so that the acceptance of the next accelerating cavity is not met. Therefore, three rebunching cavities are necessary to guarantee efficient acceleration in the other cavities, as well as longitudinal stability. A buncher is a cavity that is used not to accelerate the injected beam, but to focus the beam in the longitudinal plane. A buncher cavity is operated with a design phase in the range around -90°. The reference particle is not affected, but slower particles are accelerated, while faster ones are decelerated, decreasing the phase spread.

Another conclusion from the observed increase of the phase spread is that the distance between cavities should be kept as short as possible. Therefore, the lengths and longitudinal geometry of the quadrupole triplets are chosen to be identical and as short as technically feasible.

III.1.2 Resulting Design

The DTL beam dynamics design consists of 45 normal conducting CH-type cavities, of which the second, fifth and eighth are rebunchers. The whole DTL section is $66.7\,\mathrm{m}$ long. The effective voltages of the accelerating cavities have been set to the maximum, while the voltages of the rebunching cavities are optimized to avoid overfocusing.

There are no losses and the beam envelopes show no abnormalities, the longitudinal envelope becomes increasingly smooth along the linac. It can be observed that the emittances show an moderate, but expectable growth for such a high beam current machine. The input and output rms emittance values can be found in Table III.1. The beam envelopes are visualized in Figure III.6 and III.7.

Emittance	Input Value	Output Value
$\epsilon_{rms,\,x}$	$1.67\,\mathrm{mm\,mrad}$	$2.27\,\mathrm{mm\,mrad}$ $(+35.93\,\%)$
$\epsilon_{rms,\,y}$	$1.82\,\mathrm{mm\,mrad}$	$2.48\,\mathrm{mm\,mrad}$ $(+36.26\,\%)$
$\epsilon_{rms,\,E}$	$18.64\,\mathrm{keV\,ns}$	$23.74\,\mathrm{keV\,ns}$ $(+27.36\,\%)$

Table III.1: Input and output emittance values.

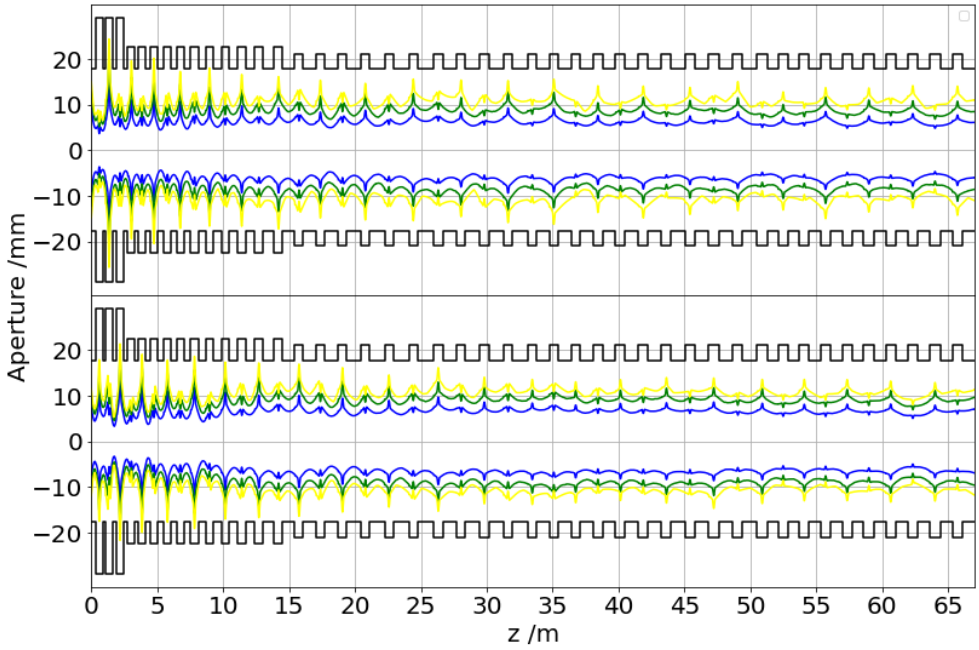

Figure III.6: The transversal beam envelopes from the first to the last cavity.

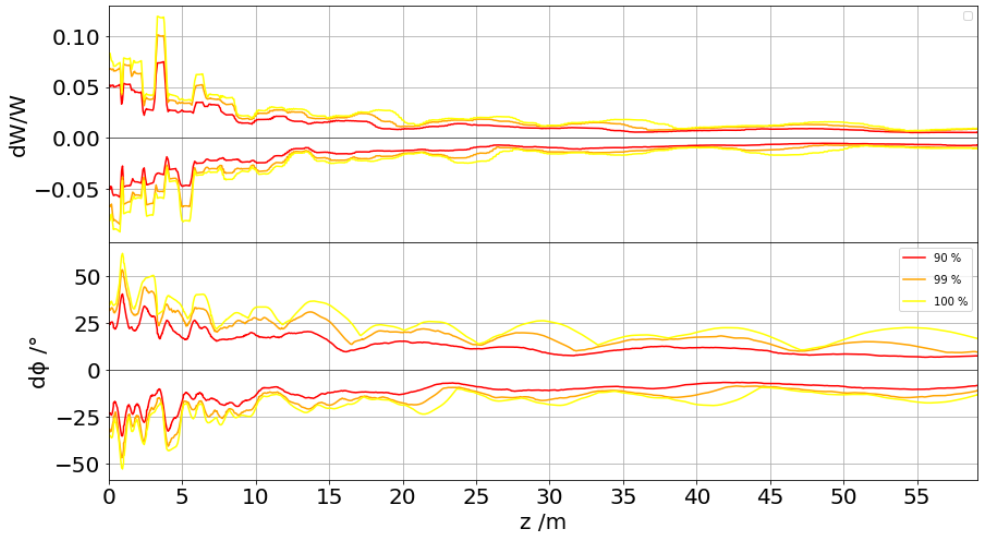

Figure III.7: *The longitudinal beam envelopes from the first to the last cavity.*

The beam dynamics parameters of the resulting design for all 45 cavities can be found in the Tables III.2 and III.3 and are visualized in Figure III.8. The beam emittance input and output values are listed in Table III.1, the corresponding phase space portraits are shown in Figure III.9.

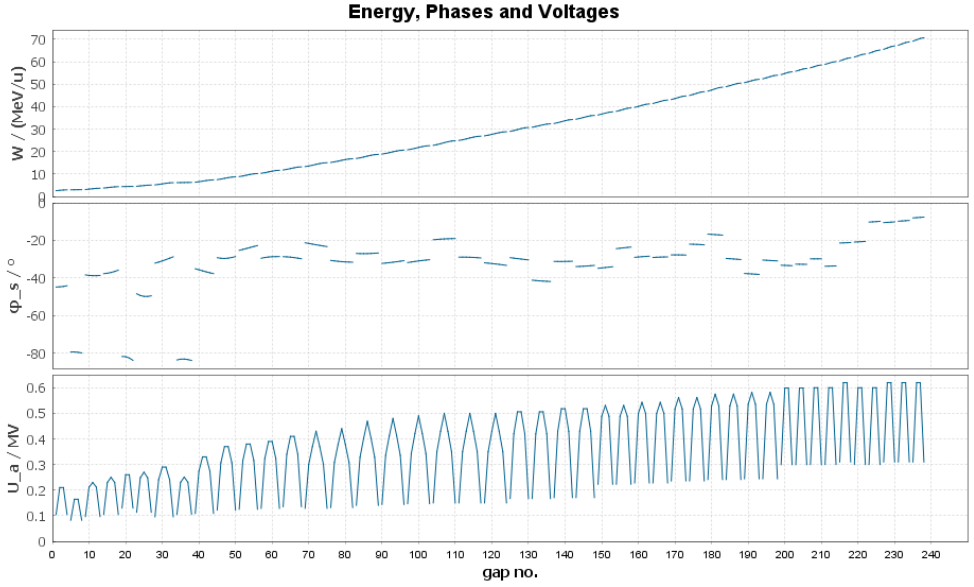

Figure III.8: *The energy gain (top), phases (middle) and gap voltages (bottom) of all 45 cavities of the current DTL design.*

The current design has been tested with Tracewin and the results are consistent with the LORASR

CH	Phase / deg	Energy Gain / MeV	Gaps	Length / cm	Effective Voltage / MV
1	-45	0.45	4	47.8	0.63
2	-83	0.06	4	49.0	0.49
3	-39	0.66	5	57.7	0.85
4	-39	0.71	5	61.2	0.92
5	-89	0.02	4	54.7	0.78
6	-45	0.71	5	64.5	0.99
7	-30	1.08	6	77.7	1.25
8	-89	0.02	5	70.6	0.92
9	-37	1.14	6	82.9	1.43
10	-26	1.43	6	88.4	1.6
11	-25	1.49	6	94.1	1.64
12	-34	1.4	6	99.3	1.68
13	-44	1.27	6	103.8	1.77
14	-24	1.86	7	123.2	2.03
15	-30	1.79	7	129.5	2.08
16	-25	2.01	7	135.7	2.21
17	-31	1.95	7	141.7	2.27
18	-43	1.7	7	147.0	2.31
19	-33	1.98	7	152.1	2.36
20	-33	1.97	7	157.3	2.36

Table III.2: *Beam dynamics parameters for the DTL section, CH 1 to CH 20.*

results. Preliminary error studies are shown in Chapter III.1.5. Advanced error studies with 1000 runs of 100000 particles are planed as further steps.

CH	Phase / deg	Energy Gain / MeV	Gaps	Length / cm	Effective Voltage / MV
21	-35	1.94	7	162.2	2.36
22	-30	1.89	6	146.2	2.19
23	-40	1.69	6	149.8	2.19
24	-29	1.95	6	153.3	2.24
25	-32	1.9	6	156.9	2.24
26	-34	1.62	5	137.1	1.95
27	-25	1.77	5	139.6	1.95
28	-31	1.72	5	142.1	2.0
29	-32	1.69	5	144.5	2.0
30	-31	1.77	5	146.9	2.07
31	-25	1.87	5	149.3	2.07
32	-19	2.0	5	151.8	2.12
33	-31	1.82	5	154.3	2.12
34	-38	1.68	5	156.4	2.14
35	-30	1.85	5	158.6	2.14
36	-32	1.52	4	132.9	1.8
37	-31	1.54	4	134.3	1.8
38	-28	1.59	4	135.7	1.8
39	-32	1.52	4	137.1	1.8
40	-30	1.61	4	138.5	1.86
41	-25	1.63	4	139.9	1.8
42	-29	1.57	4	141.3	1.8
43	-30	1.62	4	142.7	1.86
44	-27	1.66	4	144.0	1.86
45	-20	1.74	4	145.4	1.86

Table III.3: *Beam dynamics parameters for the DTL section, CH 21 to CH 45.*

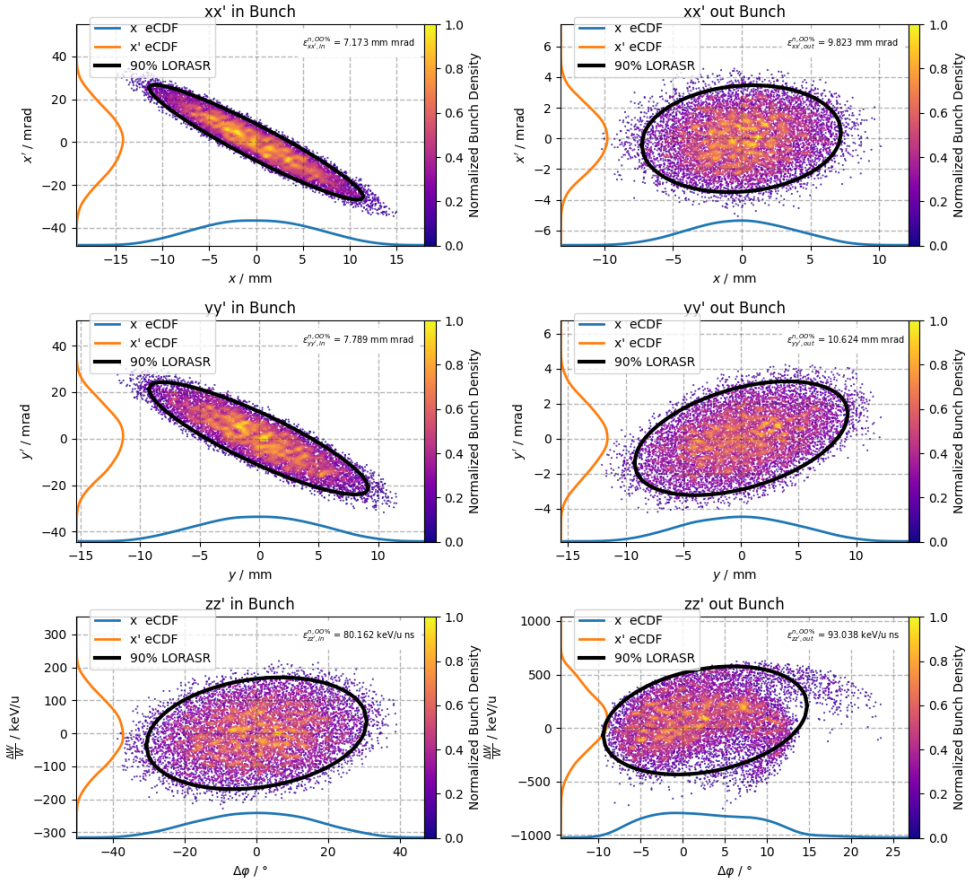

Figure III.9: *The phase space portraits of the input and output distributions.*

III.1.3 Focusing Lattice

The quadrupole lenses for transversal focusing will consist of two outer lenses of $5\,\mathrm{cm}$ effective length and a center lens of $8.5\,\mathrm{cm}$ effective length, with $1.5\,\mathrm{cm}$ gaps separating them. The quadrupole dimensions are effective lengths used for the simulations, since the absolute geometric dimensions have not yet been finalized. A schematic overview of this set-up between two cavities can be found in Figure III.10. The field strength, diameters and resulting gradients are listed in Tables III.4 and III.5. The focusing scheme is that of alternating triplets, as this proved to be the choice that results in the lowest emittance growth and overall smoothest envelopes.

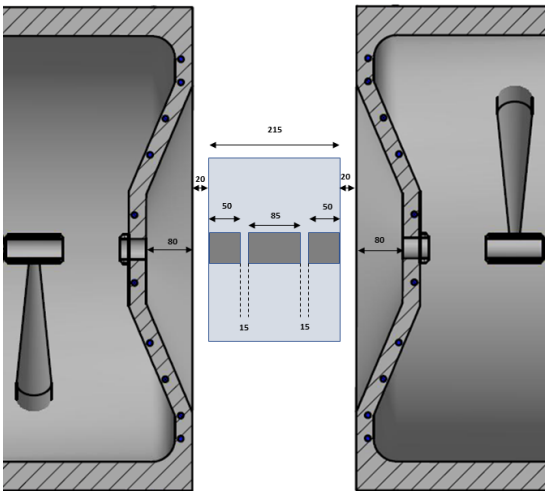

Figure III.10: The geometry of the quadrupole triplet lenses between two cavities. All effective lengths are in mm.

No.	Diameter / cm	Q_1 / (G/cm)	Q_2 / (G/cm)		B_2 / T
1	5.8	3658	3723	1.06	1.08
2	5.8	3790	3826	1.1	1.11
3	5.8	3651	4012	1.06	1.16
4	4.5	4183	4268	0.94	0.96
5	4.5	3731	4132	0.84	0.93
6	4.5	4275	4421	0.96	0.99
7	4.5	4055	4392	0.91	0.99
8	4.5	4081	4401	0.92	0.99
9	4.5	4130	4601	0.93	1.04
10	4.5	4403	4718	0.99	1.06
11	4.5	4207	4686	0.95	1.05
12	4.5	4018	4523	0.9	1.02
13	4.5	3966	4488	0.89	1.01
14	4.5	3948	4507	0.89	1.01
15	4.2	4244	4779	0.89	1.00
16	4.2	4568	5222	0.96	1.10
17	4.2	4920	5550	1.03	1.17
18	4.2	4702	5366	0.99	1.13
19	4.2	4687	5334	0.98	1.12
20	4.2	4567	5236	0.96	1.10

Table III.4: *The parameters for the quadrupole triplet focusing elements 1 to 20. Listed are the gradients Q_1 of the outer lenses, the gradients q_2 of the inner lens, as well as the corresponding field strengths.*

No.	Diameter / cm	Q_1 / (G/cm)	Q_2 / (G/cm)	B_1 / T	B_2 / T
21	4.2	4384	5039	0.92	1.06
22	4.2	4604	5342	0.97	1.12
23	4.2	4607	5286	0.97	1.11
24	4.2	4786	5549	1.01	1.17
25	4.2	3850	4489	0.81	0.94
26	4.2	4672	5456	0.98	1.15
27	4.2	4235	4868	0.89	1.02
28	4.2	4941	5799	1.04	1.22
29	4.2	4515	5230	0.95	1.10
30	4.2	4642	5459	0.97	1.15
31	4.2	4330	5047	0.91	1.06
32	4.2	4491	5320	0.94	1.12
33	4.2	4634	5438	0.97	1.14
34	4.2	4802	5676	1.01	1.19
35	4.2	4924	5804	1.03	1.22
36	4.2	4632	5560	0.97	1.17
37	4.2	4533	5445	0.95	1.14
38	4.2	4686	5642	0.98	1.18
39	4.2	4231	5112	0.89	1.07
40	4.2	4610	5549	0.97	1.17
41	4.2	4664	5594	0.98	1.17
42	4.2	4753	5725	1.0	1.20
43	4.2	4570	5508	0.96	1.16
44	4.2	4753	5725	1.0	1.20

Table III.5: *The parameters for the quadrupole triplet focssing elements 20 to 44. Listed are the gradients Q_1 of the outer lenses, the gradients q_2 of the inner lens, as well as the corresponding field strengths.*

III.1.4 Debunching Section

The intermediate design approach for the debunching sections consists of three cavities: two cavities with a positive phase of around 90° and one cavity with a negative phase of around -90°. When the beam enters the first two cavities, the earlier particles (concerning the longitudinal phase space) get more energy then the reference particle and are therefore faster, while the later particles get decelerated and become therefore slower.

After these two cavities there is a drift of several meters, in which, because of the energy profile that has been imprinted, the longitudinal emittance ellipse is "stretched": while drifting, earlier particles, which are faster, will drift away from the reference particle, resulting in an even lower negative phase. The opposite is true for slower particles. The longer the drift, the higher the achieved phase spread. The beam thus prepared is then injected into the last cavity. Here, with a negative phase of -90°, the longitudinal phase space ellipse is tilted, finally minimizing the energy spread.

The simulations for the HBS debunching section have been performed for an input distribution of $\pm 600\,\mathrm{keV}$ energy spread with a beam end energy of $70\,\mathrm{MeV}$. It is $16.5\,\mathrm{m}$ long and consists of three 4-gap CH-type cavities. Table III.6 shows the properties of the debunching section. The energy spread is minimized to approximately $\pm 150\,\mathrm{keV}$, i.e to about $\pm 0.2\,\%$ of the beam energy. The longitudinal envelope is shown in Figure III.11, the input and output emittance ellipses are shown in Figure III.12.

CH	Phase / deg	Gaps	Length / cm
1	86	4	146.7
2	85	4	146.8
3	-86	4	146.8

Table III.6: Parameters of the debunching section.

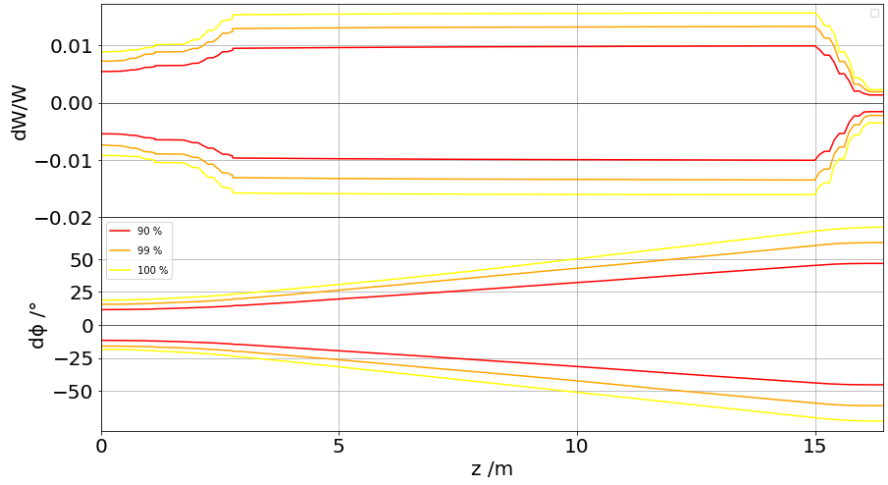

Figure III.11: The longitudinal beam envelopes of the debuncher section.

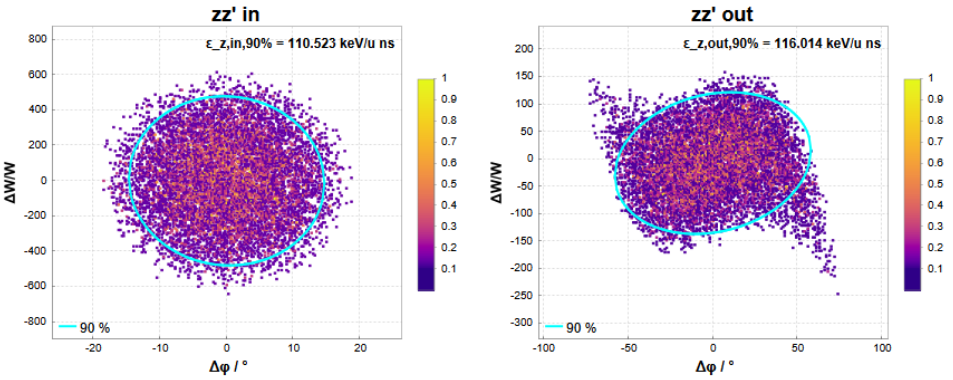

Figure III.12: The longitudinal input and output phase space portraits of the debuncher section.

III.1.5 Preliminary Error Studies

With LORASR, error studies can be performed using gaussian distributed machine errors. This way, many different combinations of possible machine errors can be studied, each run containing a different combination of error values for several parameters. The parameters passed to LORASR are the assumed maximum errors, where the gaussian distribution of the possible error values is cut of at 2σ.

First error studies have been performed with a number of 100 runs for 10000 particles, implementing errors for the voltages, quadrupole positions and cavity phases. The implemented errors are shown in Table III.7. An averaged loss rate using all 100 runs is calculated. The growth in rms-emittance is shown in Figure III.13. It can be observed that the additional emittance growth due to assumed errors is only moderate, with a maximum of around $3\,\%$ for the transversal plane and for most cases under $15\,\%$ longitudinally. Figure III.14 shows the positions along the beam line where the averaged losses occur. It can be observed that a possible "hot spot" for losses occurs at approx. $30\,\mathrm{m}$.

Error	Value
Quadrupole lens translations ΔX_i, ΔY_i (each singlet separately)	$0.1\,\mathrm{mm}$
Gap voltage amplitude error $\Delta\ U_{i,j}$ (each gap j separately)	$5\,\%$
Tank voltage amplitude error $U_{fact,i}$ (equal for all gaps belonging to the same tank i)	$1\,\%$
Tank phase error: $\Delta\Phi_i$, applied at entrance (first gap) of tank i	1°
Quadrupole lens rotation (x-y-plane)	$1\,\mathrm{mrad}$
Quadrupole lens rotation (x-z-plane)	$1\,\mathrm{mrad}$
Quadrupole lens rotation (y-z-plane)	$1\,\mathrm{mrad}$

Table III.7: Assumed errors for the preliminary error studies.

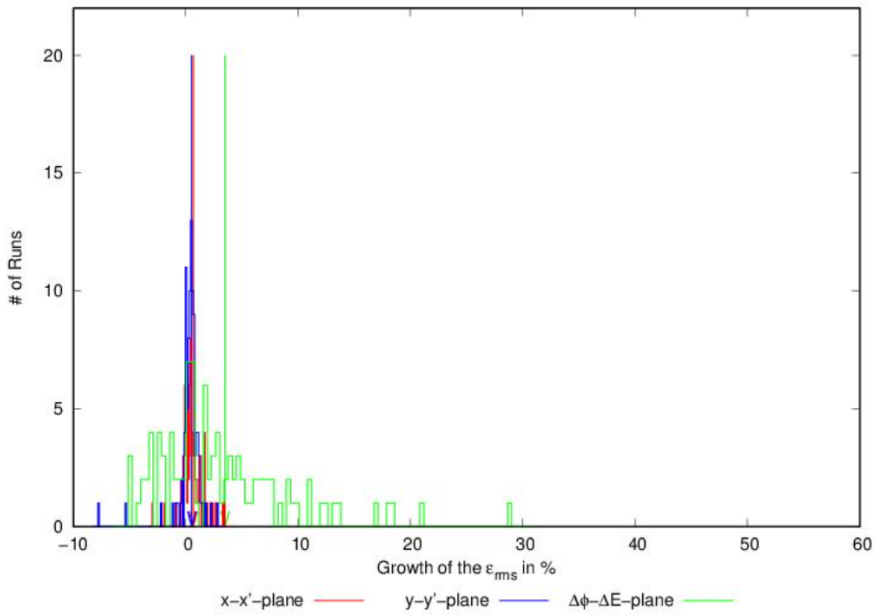

Figure III.13: *The additional rms emittance growth.*

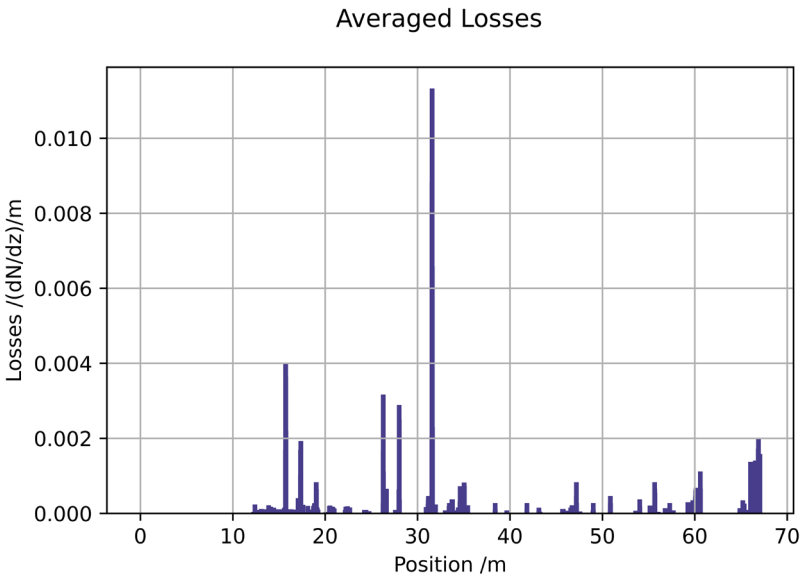

Figure III.14: *Simulated averaged particle loss for all error study runs along the beam line.*

III.2 Drift Tube Linac: Cavity Design

III.2.1 Types of acceleration structures

To bring ions in a particle accelerator to the desired energy, the ions must be accelerated by a force. The Lorentz force, formula III.2,is responsible for the electromagnetic interaction.

$$\vec{F}_{\mathrm{L}} = q\left(\vec{E} + \vec{v} \times \vec{B}\right) \tag{III.2}$$

Structures used to accelerate particles are usually designed according to two concepts. The first concept is called the Wideroe accelerator (see III.15). For the particles to be effectively accelerated, the length of the cylinders and the gaps must be matched to the velocity of the particles and the frequency of the radio frequency field. The resulting condition is called the Wideroe condition:

$$l_{\mathrm{Wi}} = \frac{\beta\lambda}{2} \tag{III.3}$$

In the Wideröe condition, the cylinders are alternately negatively and positively charged, resulting in

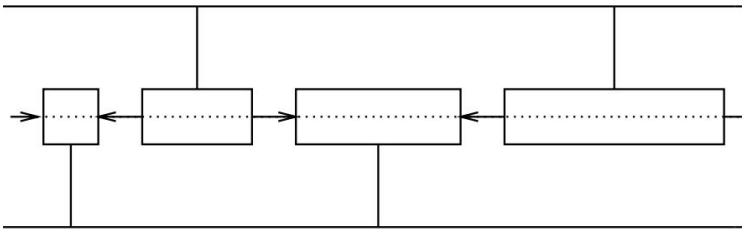

Figure III.15: *Illustration of a Wideröe accelerator. The second and fourth drift tubes are positively charged and the first and third drift tubes are negatively charged.*

an alternating electric field direction along the beam axis from gap to gap. The second concept are Alvarez accelerators. Largely analogous to Wideröe accelerators, the main difference is the charge on the cylinders. A drift tube is positively charged towards one gap side and negatively charged towards the other gap side. As a result, the electric field along the beam axis always points in the same direction. This concludes in the Alvarez condition:

$$l_{\mathrm{Al}} = \beta\lambda \tag{III.4}$$

Due to this difference, the particle bunches have to travel a longer drift distance within the drift tubes in order not to be decelerated in the alternating electric field. Depending on the requirements of the accelerator, it is usually advantageous to prefer a Wideröe accelerator to an Alvarez accelerator, e.g. because of the higher shunt impedance. Common examples of Wideröe accelerators are RFQs, IH (interdigital H-mode) and CH (crossbar H-mode) structures. The IH structure (see III.16), consists of drift tubes, stems, two girders, the tank and tuners. The stems alternately connect the drift tubes to a girder, which connects the stems to the tank. The girder has a so-called undercut for a more even field distribution between the gaps. The undercut describes the hollowing out at the narrowing part of the girder. IH structures are operated in the H_{111}-mode. With $n = 1$, the current in an IH structure flows over half the tank surface from an upper to a lower support. If the index is increased to $n = 2$, the H_{211}-mode is obtained, which represents the operating mode of the CH structure.

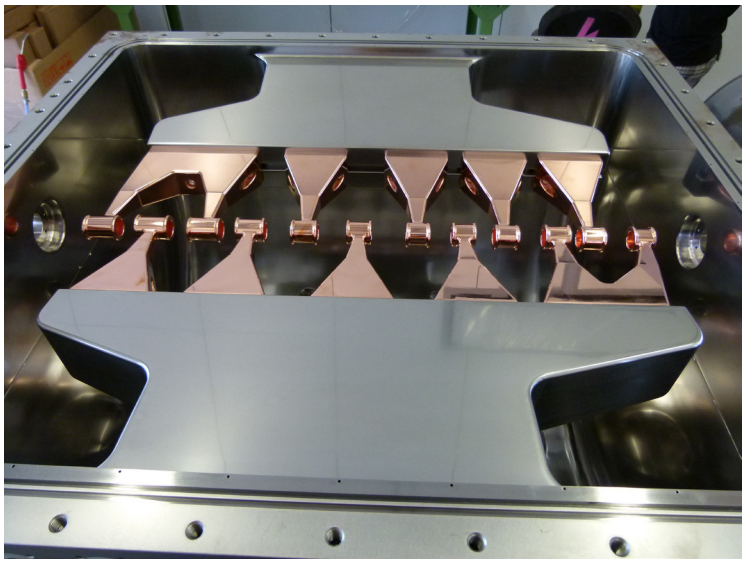

Figure III.16: Picture of the inside of an IH cavity.

III.2.2 CH-structure

The CH structure, shown in Figure III.17, unlike an IH structure, has continuous stems that house the drift tube in the center. The stems are alternately fixed in the tank with each drift tube. This creates an angle of 90° rotated about the beam axis between two consecutive stems. The CH structure is composed of drift tubes, stems, tank and tuners.

In general, IH and CH structures could be used for the HBS Linac. The stems inside the CH structure and also the drift tubes can be cooled more effectively with water. Furthermore the CH structure has negligible dipole term interference due to the symmetrical support design. The main advantage is the fact that with the MYRRHA Injector an already proven technology has been developed which can be adopted for HBS with limited R&D effort.

2.2.1 Operation in TE mode

The basis of electrodynamics and thus also for cavities are Maxwell's equations. From these equations, by applying the rotation, the wave equation for the electric field and the magnetic field can be derived in vacuum. For real complex systems like the CH structure, the wave equations can only be solved numerically. A numerical program that is a suitable choice for solving the wave equations for real cavities is, for example, CST Studio Suite. For simple constructions, such as rectangular waveguides or cylindrical cavity resonators, an analytical solution can be derived starting from the wave equations.Looking at the solution for the pillbox, we can deduce that the frequency is inversely proportional to the root of the radius. For the operation of a CH structure, the H_{211}-mode is needed, which does not contain longitudinal electric field components in the pillbox (see III.18).

Operated in this mode, a CH structure would not be able to accelerate particle bunches. By introducing the stems and drift tubes, and thus differing from the simple cylindrical cavity resonator, electric field can also be focused on the beam axis in the H_{211}-mode. The resulting electric field distribution of the E_z-component on the beam axis and the magnetic field distribution is shown in figure III.19. The frequency of the H_{211}-mode drops from $615.1\,\mathrm{MHz}$ for the pillbox by the factor of 0.29 to

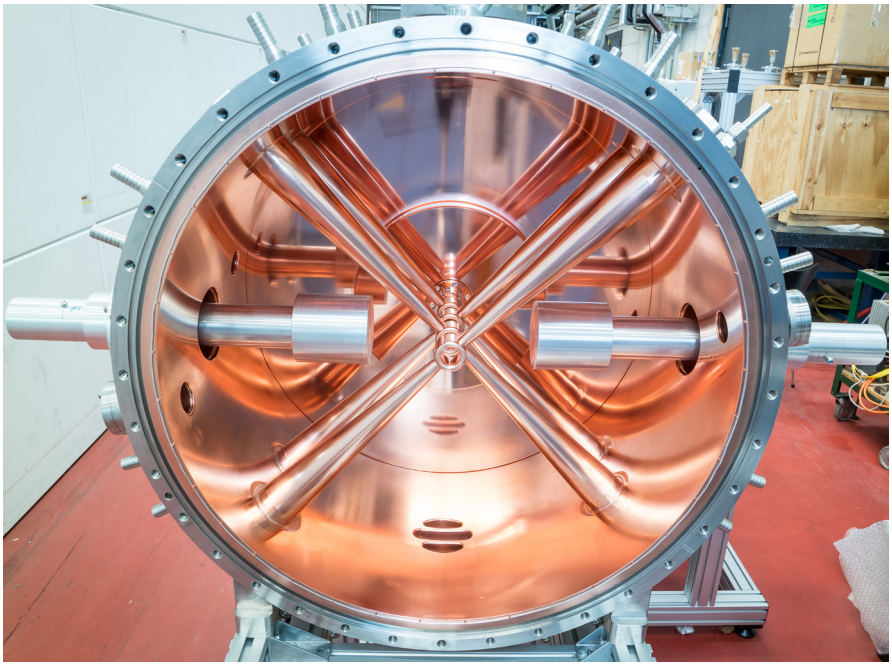

Figure III.17: *Picture of the inside of a CH cavity.*

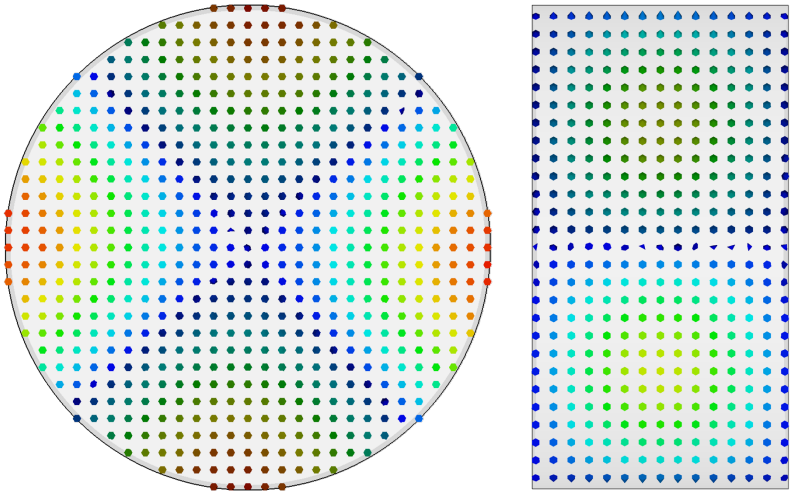

Figure III.18: *The picture shows the field distribution of the H_{211}-mode inside a pillbox cavity. On the left side you can see the magnetic field for the cut through the z axis. On the right side you can see the electric field for the cut through the x-axis.*

$176.1\,\mathrm{MHz}$ for the CH cavity with very similar radius and length.

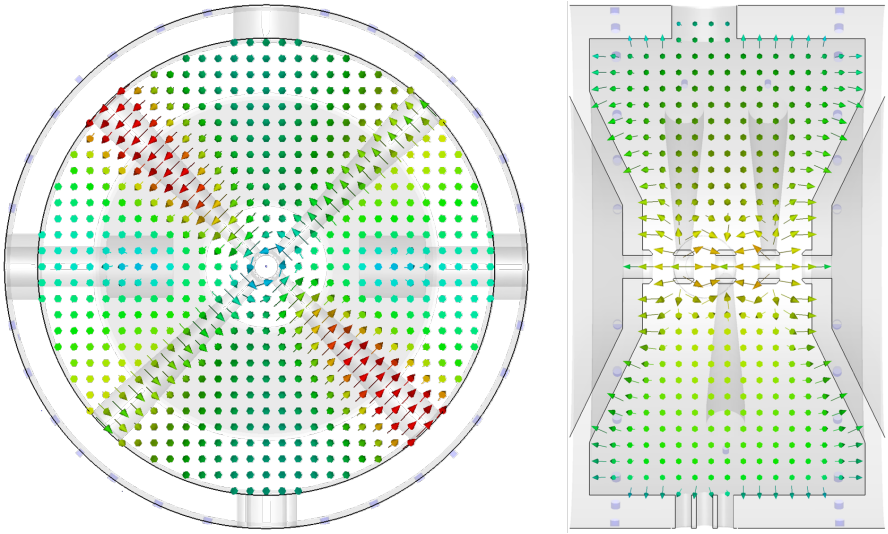

Figure III.19: The picture shows the field distribution of the H_{211}-mode inside a CH cavity. On the left side you can see the magnetic field for the cut through the z axis. On the right side you can see the electric field for the cut through the x-axis

2.2.2 Parameter for characterization

In order to be able to describe and compare resonators in a meaningful way, the relevant high-frequency parameters for cavities are now explained.

Voltage and field gradient. Integrating the electric field along the beam axis from the center of one drift tube to the center of the next drift tube yields the applied voltage of the gap between the drift tubes.

$$U_{0,k} = \int_{-\frac{L_k}{2}}^{\frac{L_k}{2}} E_z\left(z\right) \mathrm{d}z \tag{III.5}$$

If the speed of the particles is taken into account in addition to the time dependency, an effective voltage can be calculated. The relation of maximum voltage U_0 and effective voltage U_a is called transit time factor.

$$T\left(\beta\right) = \frac{U_a}{U_0} < 1 \tag{III.6}$$

The transit time factor is typically between 0.7 and 0.9 for H-mode accelerators. To obtain the total effective voltage of the cavity, the electric field can be integrated over the effective length of the cavity. The effective length l_{eff} is composed of the sum of the $\beta\lambda/2$-lengths of the individual columns.

$$U_a = \int_0^{l_{\mathrm{eff}}} E_z\left(z\right) \cos\left(\frac{\omega z}{\beta c}\right) \mathrm{d}z \tag{III.7}$$

$$E_a = \frac{U_a}{l_{\mathrm{eff}}} \tag{III.8}$$

To obtain the effective field gradient of the entire cavity, divide the total effective voltage by the effective length.

Quality factor. The measure of how long or how many oscillations a system can perform until the stored energy has dropped to the e-th part is called quality factor. The quality factor Q_0 is defined as follows:

$$Q_0 = \frac{\omega_0 W}{P_c} = \frac{\omega_0}{\omega_2 - \omega_1} \tag{III.9}$$

Shunt impedance. An essential parameter to describe a cavity is the shunt impedance. It is a measure that describes how effectively the electric field can be focused on the beam axis in relation to the coupled power. To ensure a fair comparison, the shunt impedance should be normalized to the effective length.

$$Z_a = \frac{U_a^2}{P l_{\text{eff}}} \tag{III.10}$$

R/Q value. This value represents the shunt impedance normalized to the quality factor. The R/Q value indicates how small the deviation of the electric field in the entire volume of the cavity is compared to the electric field on the beam axis.

$$\frac{R_a}{Q_0} = \frac{U_a^2}{\omega_0 W} \tag{III.11}$$

Electric peak fields. The ratio of the peak electric field E_{peak} inside a cavity to the acceleration gradient E_a must not be neglected in the design of a CH structure. The relationship depends strongly on the geometry of the structure. For the design of normal-conducting CH structures, which are also the basis for HBS structures, the ratio is in the range of:

$$8 < \frac{E_{\text{peak}}}{E_a} < 20 \tag{III.12}$$

The range of values was determined by numerical simulations. In 1957, W. D. Kilpatrick empirically determined a limit value of the electric field as a function of frequency for cavities, above which flashovers of the electric field can no longer be excluded. The formula for calculating this limit, called the Kilpatrick Limit, was reformulated by T. J. Boyd in 1982 and is as follows:

$$f(\text{MHz}) = 1.64 \cdot E^2\,(\text{MV/m}) \cdot e^{-\frac{8.5}{E\left(\frac{\text{MV}}{\text{m}}\right)}} \tag{III.13}$$

Nowadays, the Kilpatrick limit can be exceeded without sparking or break-downs due to better surface treatment and vacuum technology. Depending on the complexity of the structure, the ratio of E_{peak} to E_{Kil} should not exceed a certain limit. In the case of HBS, a value of 2 should not be exceeded. The combination of the ratio of E_{peak}/E_a and Kilpatrick limit represents one of the two limitations in the design of CH structures.

2.2.3 RF coupling

In order to couple power into a cavity or to make measurements on a cavity, one must interact with the electromagnetic wave, which represents the fundamental mode of the cavity. On the one hand, a capacitive coupling to the electric field can take place. The capacitive coupling is realized, for example, by a coaxial conductor[5], which is inserted into the cavity. The location of the cylinder should be a position at the edge of the cavity with the highest possible electric field strength to ensure effective coupling to the electric field. The other option is inductive coupling to the magnetic field. Analogous to capacitive coupling, an optimal position at the edge of the cavity should be chosen

[5] The length of the inner conductor in relation to the outer conductor influences coupling strength

for coupling to the magnetic field. The inductive coupling is realized by a loop[6], which is partially or completely immersed into the cavity. For the purpose of describing the influence of the coupling, the so-called coupling factors β are defined, where β_e is the coupling factor of the inbound coupling and β_t is the coupling factor of the outbound coupling.

$$\beta_e = \frac{Q_0}{Q_e} = \frac{P_e}{P_c} \tag{III.14}$$

$$\beta_t = \frac{Q_0}{Q_t} = \frac{P_t}{P_c} \tag{III.15}$$

Using these definitions, the equation for the loaded quality factor can be rewritten as:

$$Q_0 = Q_L \left(1 + \beta_e + \beta_t\right) \tag{III.16}$$

The coupling factor is divided into three ranges:

weak coupling with $\beta < 1$ In the case of weak coupling, the influence on the overall cavity system is minimized. In general, it is tried that the coupling factor of the decoupling β_t is as small as possible and ideally $\beta_t = P_t \approx 0$.

critical coupling with $\beta = 1$ In the case of critical coupling, the reflected power back from the coupling towards the power generator is minimal. Assuming negligible outcoupling, in the case of critical coupling, the loaded Q is twice as large as the unloaded Q.

strong coupling with $\beta > 1$ For this case, there is strong coupling with the electromagnetic wave inside the cavity. The amount of Q loaded is largely determined by the Q of this coupler.

Up to this point, only the cavity and its properties in operation have been considered. A missing point is the particle beam, which is to be accelerated inside the cavity. The beam represents an additional load for the cavity, which influences our coupling factors. Assuming that the decoupling is ideally set to $\beta_t = P_t \approx 0$, $\beta = \beta_e$ holds. Now, in order to further keep the reflected power with particle beam minimal, the following holds for an adjusted critical coupling:

$$\beta = 1 + \frac{P_b}{P_c} \qquad \text{with} \tag{III.17}$$

$$P_b = U_a I_b \tag{III.18}$$

Depending on the design of the individual CH cavities, a coupling factor with beam of 2 to 3.5 is required for HBS.

2.2.4 Construction details

To ensure sufficient mechanical stability and avoid unnecessary costs, the CH cavities are made of stainless steel. However, since steel has poor electrical conductivity, the interior of the CH cavities is copper-plated. The thickness of the copper layer, determined by the skin effect, is chosen in such a way that at each point the current is conducted through copper and not through steel. The typical copper layer thickness is between 50 and 100 μm. The design of the CH structures provides for a tapered lid, as shown in Figure III.20.

On the one hand, this shape of the lid offers the advantage of a more homogeneous voltage distribution between the individual gaps of a cavity. On the other hand, additional beam diagnostic elements can be installed between two cavities. Furthermore, the CH cavities have a flange for coupling, which is located on the upper side. The coupling is inductive via a loop (see Figure III.21). The

[6] The coupling strength is influenced by the size and angle of the loop

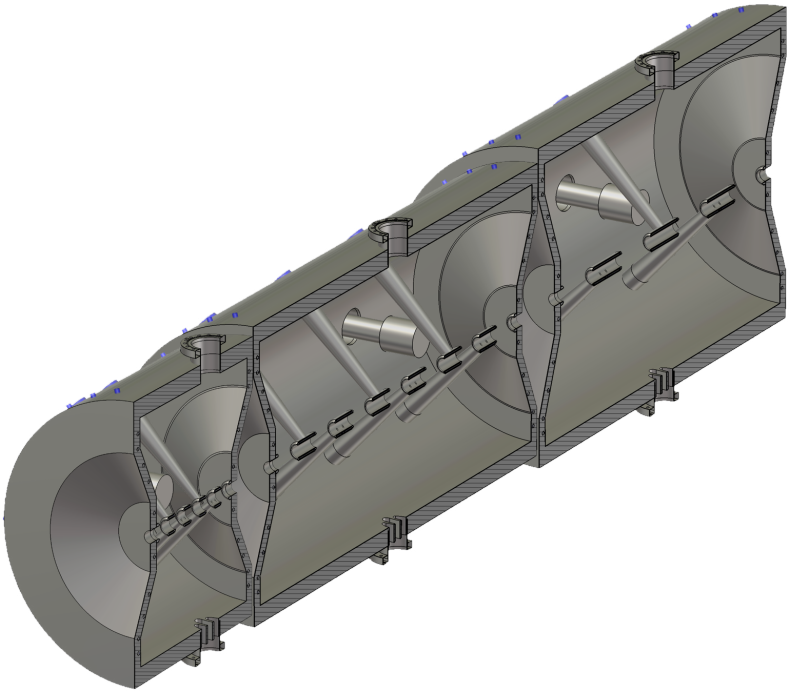

Figure III.20: *Assembly of three cavities for different energy sections cut along the beam axis. From left to right the first cavity represents the design for the low energy part, the second cavity the design for the medium energy part and the third cavity for the high energy part of the DTL accelerator.*

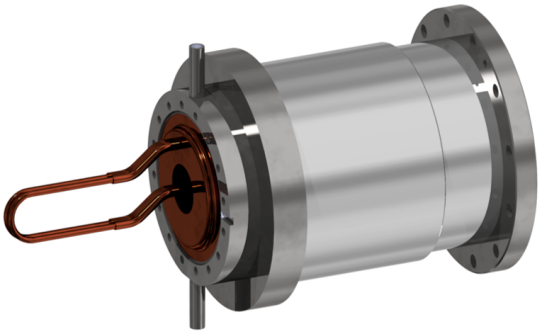

Figure III.21: *View of exemplary coupling loop.*

exact dimensions of the respective coupling loops differ from cavity to cavity depending on the beam load and the required coupling factor to minimize the reflected power und nominal operation.

In addition, there is a flange on the underside of the cavity, which is the connection for the vacuum via a built-in HF grid. There are also four small flanges for connecting a pressure gauge or a loop for coupling out a magnetic field for diagnostic purposes.

2.2.5 Tuning concept

Due to a variety of influences, the resonant frequency of a CH cavity does not remain constant during operation, which is why the installation of tuners is necessary. The basis for tuning is the Slater theorem. The principle behind this is based on introducing a disturbance body into the field of a cavity, which disturbs either the magnetic or the electric field, depending on the location and design. This disturbance leads to a shift of the resonance frequency. For the design of the CH cavities, two tuners with associated flanges are currently provided, which are positioned as shown in Figure III.22. One of the two tuners is used via a motor for dynamic frequency control, the other tuner is used to correct frequency deviations that occur due to manufacturing tolerances.

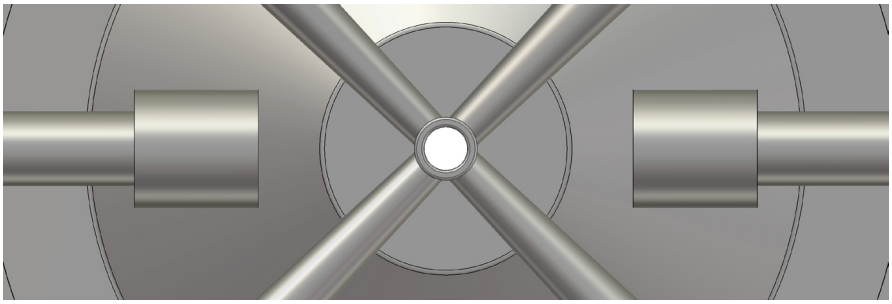

Figure III.22: *Position of tuner in relation to the drift tubes and stems.*

After fabrication and copper plating, a CH-cavity is subjected to low-level RF measurements. Part of these investigations is the determination of the positions of the two plungers - i.e. their operating points, as well as the tuning range of the dynamic tuner. For this purpose, the cavity is first fitted with two freely movable dummy tuners, which can be moved over a wide measuring range to the positions within the cavity. Under constant observation of the modes excited in the cavity with the aid of a connected network analyzer (NWA), the two tuners are symmetrically shifted into the cavity until the target frequency (including a margin for the so-called vacuum shift) is reached. In this process, the frequency range monitored by the NWA includes a range of at least 5 MHz around the target frequency. No parasitic tuner mode should be measurable within this range. If no parasitic mode is detectable, this position is the "operating point" of the two tuners and thus the fixed position of the static tuner. In a next step, one of the two tuners is now moved over a larger range and the change in frequency is measured, while it must still be ensured that no parasitic mode is measurable. Within the possible tuning range measured in this way, a range with a maximum tuner stroke of 80 mm is finally defined, which covers a range of at least ± 0.2 MHz around the target frequency. This procedure has to be performed individually for each cavity. Figure III.23 shows the measured frequency as function of the distance of the tuner tip with respect to the beam axis for the MYRRHA CH-1. Since the tuner acts capacitively, the frequency decreases with decreasing distance to the beam axis. If the distance is too small, there is a possibility that the electric field in the area of the tuner will increase too much. This must be taken into account when determining the operating point.

The plungers of the static and the dynamic tuner have basically the same geometrical design and only differ in length and in the mounting to the flange, or the dynamic tuner system (Fig. III.24. The plungers have to be water-cooled and are equipped with two G 3/8" bores for water connectors (thread depth $\leqslant$ 10 mm). A water flow rate of 10 l/min with a maximal pressure drop $\sim$ 5 bar has to be provided. All plungers have to be built out of copper plated stainless steel (1.4301 or 1.4401 with Ra = 0.8 and Rz = 6.3) to achieve the required stability and conductivity.

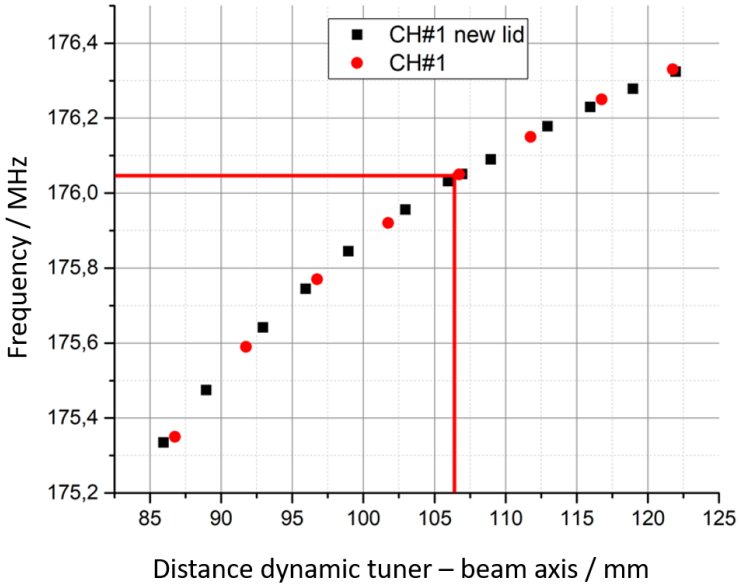

Figure III.23: *Measured frequency as function of the distance of the tuner tip with respect to the beam axis for the MYRRHA CH-1.*

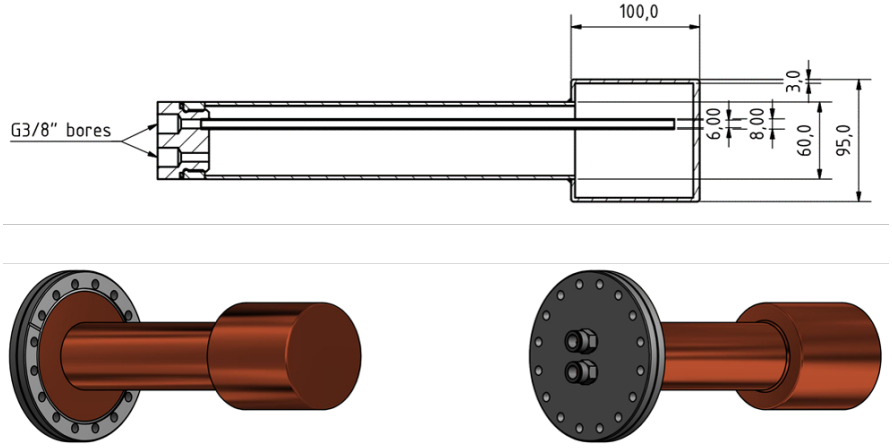

Figure III.24: *Layout of the tuners for the CH-cavities.*

2.2.6 Cooling concept

Good cooling is essential for a reliable operation. The cooling design of the CH cavities consists of 24 cooling channels for the tank, two cooling channels for the lids, one cooling channel for the coupling loop, one cooling channel per tuner and one cooling channel per stem (see Figure III.25). This design was successfully tested for high acceleration gradients during the MYRRHA project. A minor change to the design for the HBS project is the introduction of an additional water volume at the beginning and end of each stem. With the help of this volume, the thermal load on the weld seam at the stem is reduced. Figure III.26 shows an ANSYS simulation using flow dynamics and the power distribution with 120 % of the nominal power. In this simulation, the tank lid was because of numerical reasons not cooled and shows therefore the highest (unrealistic) temperature. Every

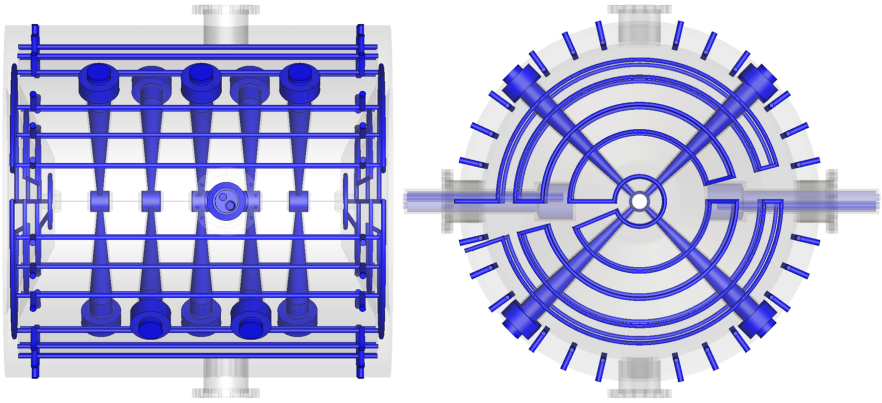

Figure III.25: *Side (left) and front (right) view of the cooling channels inside a CH-cavity.*

cooling channel is equipped with a PT-100 sensor to monitor the water temperature continuously. The data are provided the control and machine protection system which will turn off the power in case of an anomalous behavior of a cooling channel.

2.2.7 Further optimization

As already mentioned earlier, the RF and mechanical design is based on the approved MYRRHA design. However, some changes and optimization have been adapted to the HBS-cavities. Firstly, the inner drift tube radius for HBS was adjusted to $17.5\,\mathrm{mm}$. With a larger drift tube radius, the risk of beam losses within a cavity is reduced, but the shunt impedance also decreases, which increases the total power required (see Figure III.27). If further adjustments to the beam dynamics require a larger drift tube radius, both the amplifiers have sufficient power reserve and the cavities have sufficient cooling to be able to cool the additional power loss.

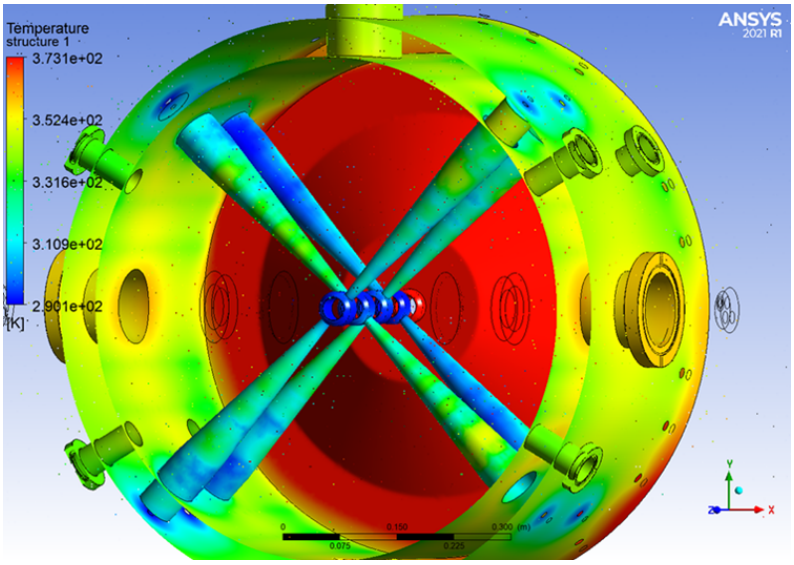

Figure III.26: *ANSYS simulation using flow dynamics and the power distribution with 120 % of the nominal power. In this simulation, the tank lid was because of numerical reasons not cooled and shows therefore the highest (unrealistic) temperature.*

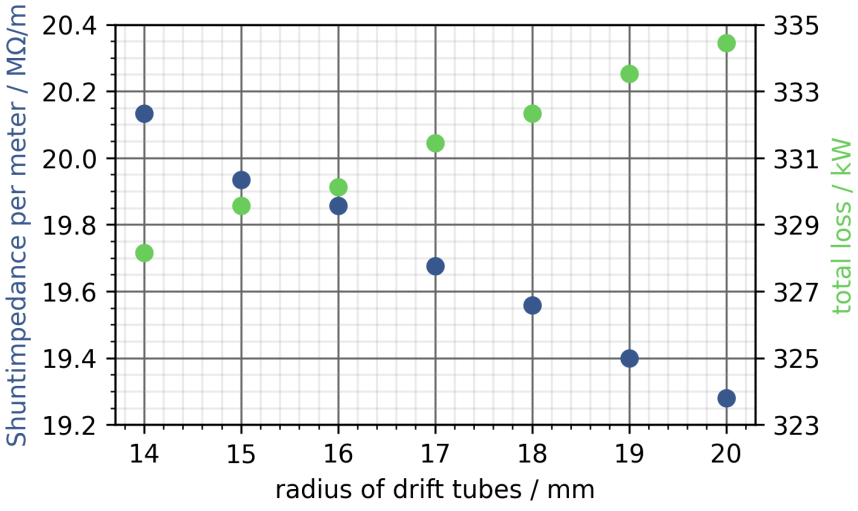

Figure III.27: *Shuntimpedance per meter plotted as a function of the drift tube radius exemplary for cavity CH-43.*

Secondly, the radius of the stem at the transition to the drift tube was adjusted. In the low energy range, the radius cannot be increased due to the small length of the drift tubes. Above an input energy of $20\,\mathrm{MeV}$, the stem radius at the drift tube is increased to $16\,\mathrm{mm}$. Despite an approximately $4\,\%$ lower shunt impedance (see Figure III.28), the enlargement has two advantages. First, the transition between the stem and the drift tube including the weld located there is cooled more efficient and second, the mechanical stability of the drift tubes is improved.

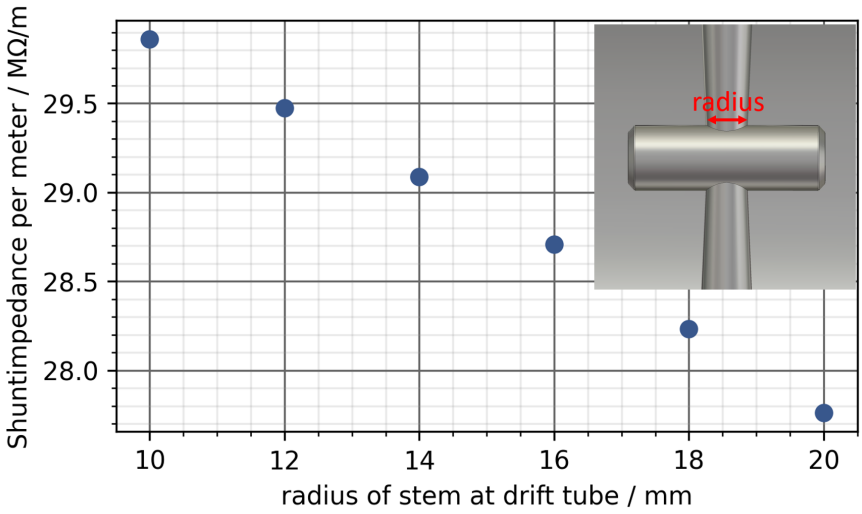

Figure III.28: *Shunt impedance per meter plotted as a function of the stem radius at the transition to the drift tube exemplary for cavity CH-43.*

To improve the ratio of the electrical peak field to the field gradient, the rounding radii of the drift tubes were adjusted (see Figure III.29). By reducing the rounding inwards, marked in green, and increasing the rounding outwards, marked in red, the ratio of E_{peak} to E_a was reduced and the Kilpatrick factor was lowered by approx. $10\,\%$ (see Figure III.30).

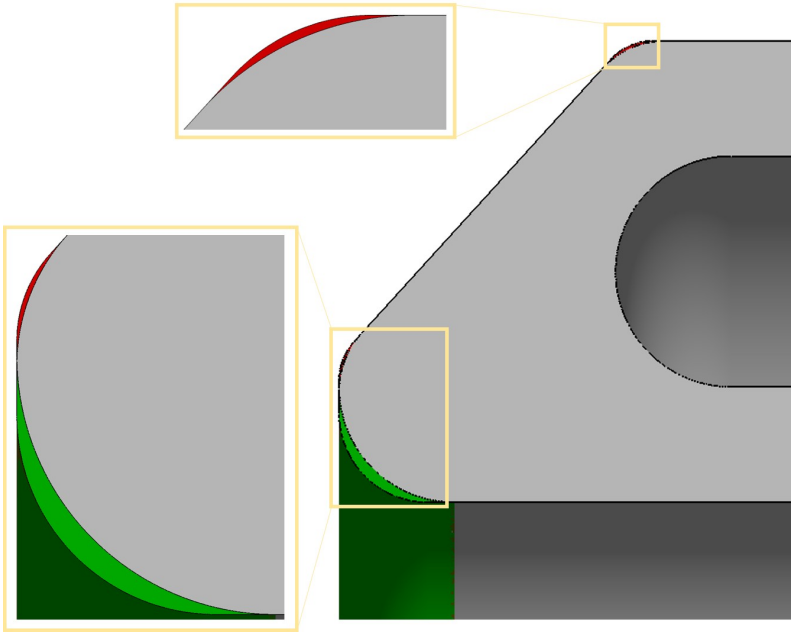

Figure III.29: Optimization of the rounding radii of the drift tubes. The parts in red will be cut away and the part in green will be added.

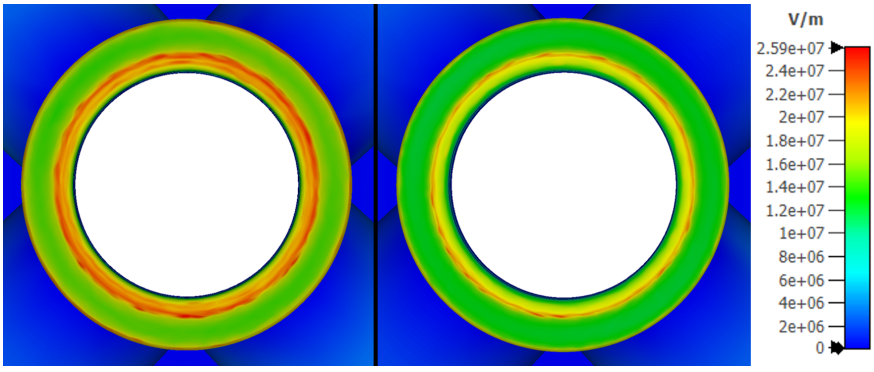

Figure III.30: Comparison between the non-optimized (left) and optimized (right) electrical peak field.

Each cavity differs from the other in terms of the gap structure. In order to be able to operate each cavity at a frequency of $176.1\,\mathrm{MHz}$, the resonance frequency of each cavity is set appropriately via the radius of the cavity (see Figure III.31). Further adjustments to optimize the design are currently

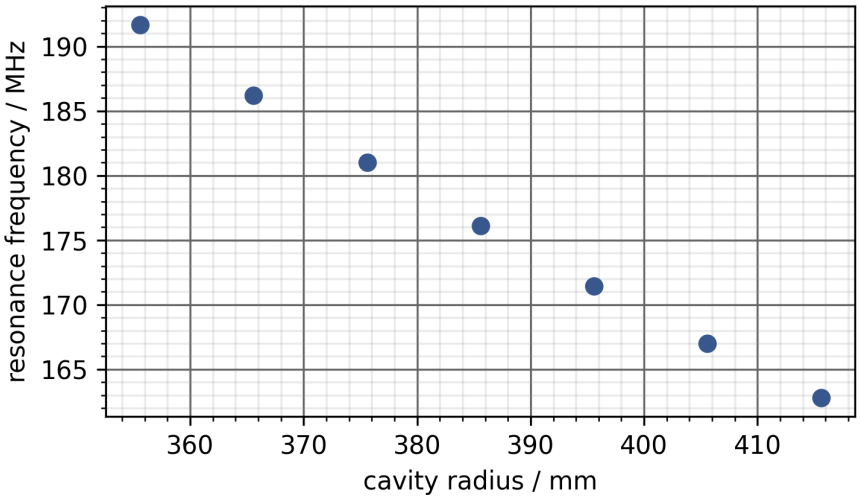

Figure III.31: *Resonance frequency plotted as a function of the radius of the cavity exemplary for cavity CH-43.*

being worked on.

2.2.8 CH-cavity design results

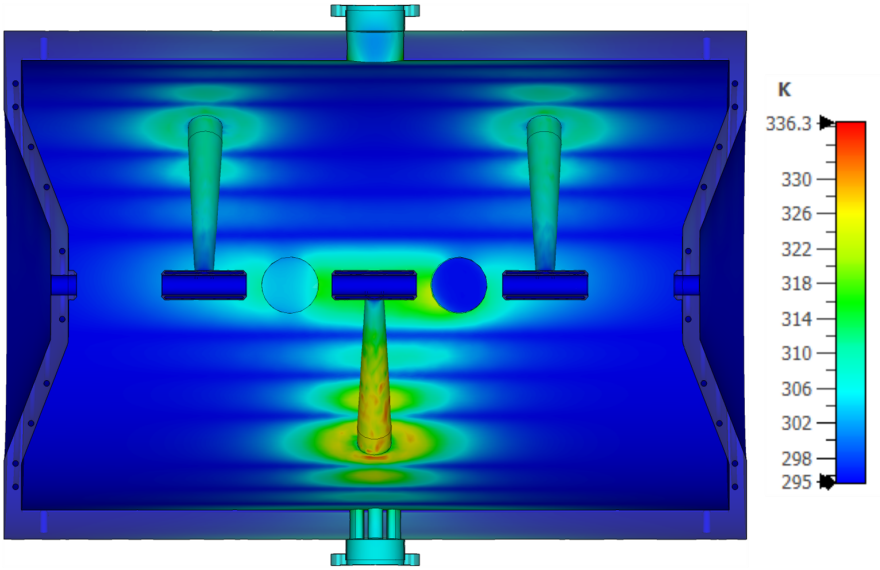

Figure III.32: Result of cooling simulation with 25 % duty cycle and 120 % of the nominal power. Plotted is the temperature distribution of the CH cavity with the hottest temperatures inside.

The cooling design is adequately sized to meet HBS requirements (see Figure III.32). The results of the DTL section are summarized in Table III.8. Furthermore, Figure III.33 to Figure III.37 graphically show the relevant parameters of the individual cavities.

Parameter	Specification	Unit
Cavity length	0.5–1.5	m
Radius of cavity	330–387	mm
Acceleration voltage U_a	0.5–2.4	MV
Duty factor (max)	25	%
Effective length	0.3–1.4	m
Shunt impedance	19–50	MΩ/m
Total power	70–375	kW
Cavity loss	20–153	kW
Thermal load (25 % duty factor)	10–30	kW/m
Amplifiers	150–500	kW
Aperture diameter	35	mm
Gradient	1.5–2.5	MV/m
No. of cavities	45	N/A

Table III.8: Summary of CH-cavities

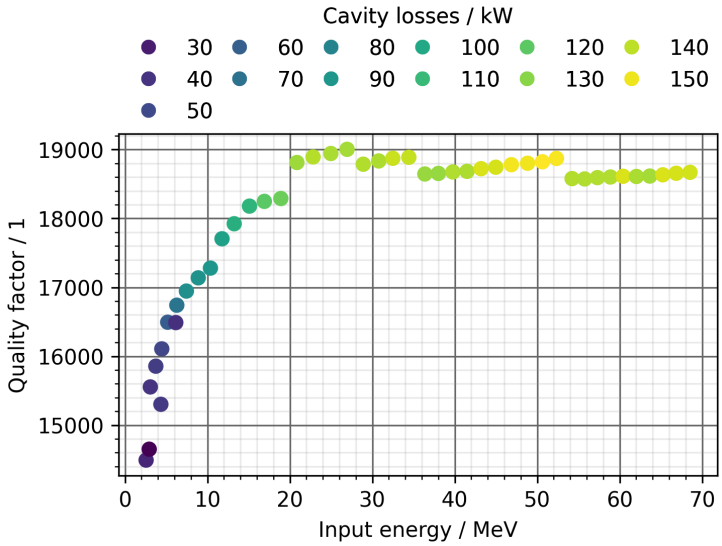

Figure III.33: *Quality factor and required cavity power plotted for each cavity as a function of the input beam energy of a cavity.*

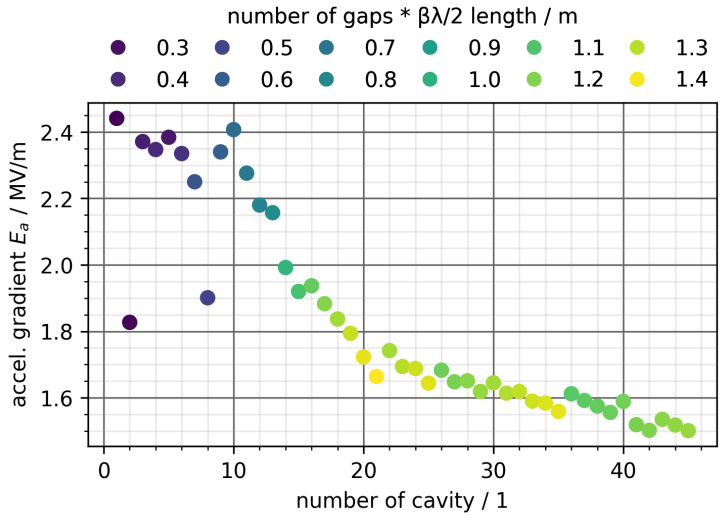

Figure III.34: *Acceleration gradient and effective length plotted for each cavity.*

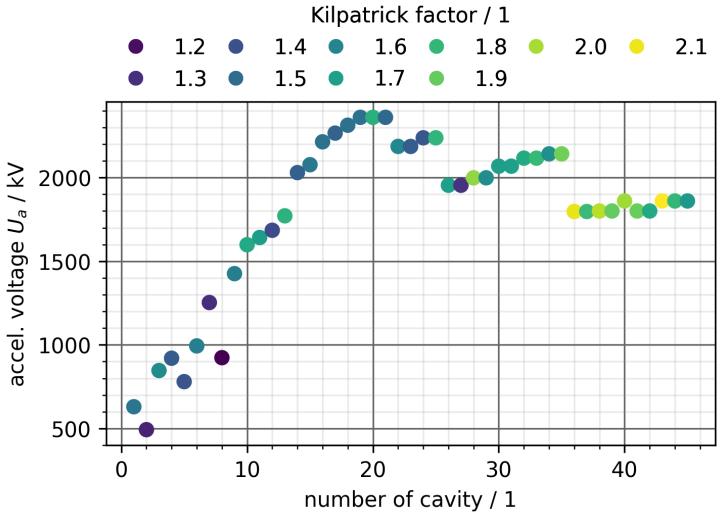

Figure III.35: *Acceleration voltage and Kilpatrick factor plotted for each cavity.*

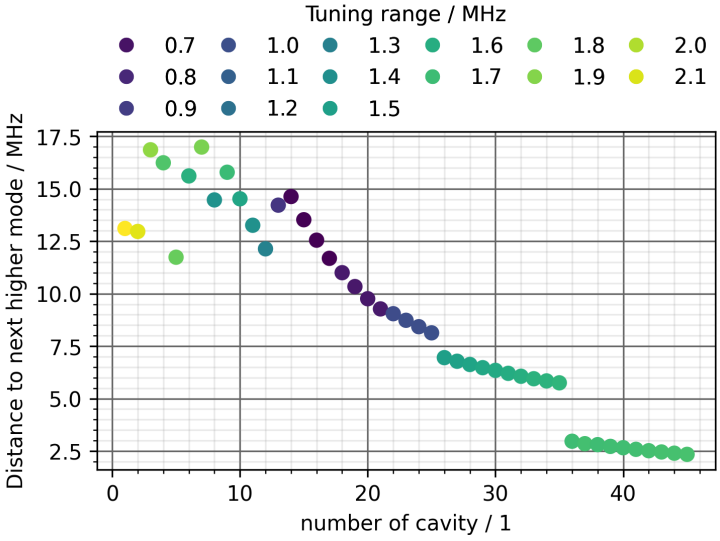

Figure III.36: *Frequency range to second mode and tuning range plotted for each cavity with a maximum tuner stroke of 80 mm.*

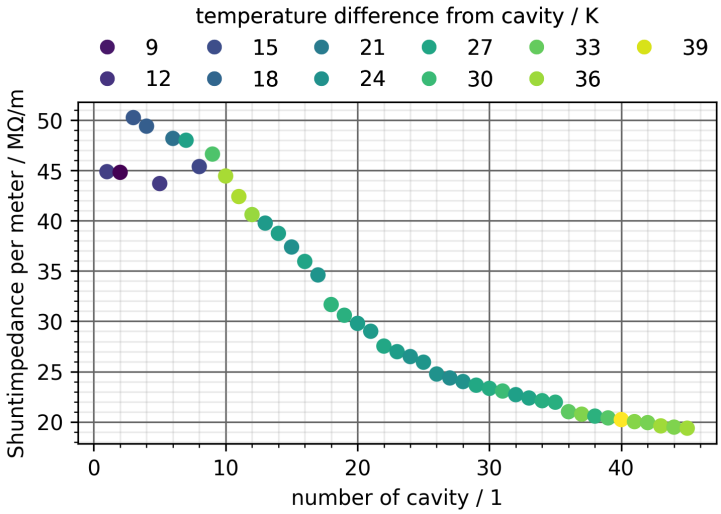

Figure III.37: *Shunt impedance per meter and maximum reached temperature inside cavity plotted for each cavity.*

IV.
RF SYSTEMS

H. Podlech

The RF system of a Linac is one of the most important sub-systems. It consists of the RF amplifiers and the Low Level RF system (LLRF) to control and stabilize the RF phase and amplitude. It has to be reliable as possible since the experience shows that the RF system is beside the proton source the main reason for down times of the accelerator. It is strongly advised to use a future-oriented technology with high reliability.

IV.1 RF power amplifiers

The RF system of the HBS-Linac must reliably provide the RF power for the cavities within certain parameters. The total power per cavity consists of the ohmic losses, the beam load, line losses and reserves. The reserves should be at least 30 % of the maximum nominal power in order to have sufficient margin for control and redundancy. The different cavities will have different power requirements. Therefore, amplifiers between 50 kW and 600 kW are required. Depending on the frequency, several amplifier technologies are available: Klystrons, IOTs, Tube Amplifiers and Solid State Amplifiers. Because of the relatively low frequency and the high peak power, only tube amplifier and solid state amplifiers are suitable for the HBS Linac. Solid state amplifiers offer some advantages. Several transistors, each delivering about 1 kW RF power, are combined into a so-called Pallet Amplifier. The required total power is finally obtained via several combiner stages.

In contrast to tube amplifiers, solid-state amplifiers can be designed redundantly. In the event of failure of one or more Pallet amplifiers, the entire system is still ready for operation. In addition, the power supplies should be operated parallel for further increase of redundancy. The reliability of the RF system is a critical issue since it is known that it causes typical the largest fraction of down times of Linac based facilities. Solid state amplifiers do not require high voltage and the foot print is much smaller compared with tube amplifiers. Furthermore, the market for these amplifiers is strongly determined by competition. Extremely reliable RF systems can be realized with solid state amplifiers. It is strongly recommended to use solid state amplifiers for HBS. The most critical issue for solid state amplifiers are the combiners. After failing of pallet modules it has to be avoided a decrease of the overall performance due to an imbalance of the remaining power in the combiner stages. A further major advantage of solid state amplifiers is the modular design using the same RF power modules and power supplies for all amplifiers which makes spare part management, maintenance and repair significantly easier. During the EU Project MYRTE (https://cordis.europa.eu/project/id/662186) a 176.1 MHz, 192 kW cw solid state amplifier has been developed for the MYRRHA RFQ. This amplifier showed very good performance and reliability. Figure IV.1 shows this solid state amplifier. Table IV.1 describes the present parameters of the amplifiers required for the HBS Linac.

Parameter	Value	Unit
Frequency	176.1	MHz
RF power	100–600	kW
RF Duty factor (max)	25	%
No of Amplifier	49	NA
Bandwidth 3 dB	$> \pm 1$	MHz
Input impedance	50	Ω
Output impedance	50	Ω
Input connector type	SMA female	NA
Nominal input level	<+10	dBm
Rise time (10–90 %)	<1	μs
Pulse length	100 .. 2000	μs
Repetition rate	1 ... 1000	Hz
Pulse over/undershoot	$< \pm 0.3$	dB
Phase linearity	<10	deg
Pulse droop	< 0.2	dB
Amplitude stability	$< \pm 0.2$	dB
Phase stability	$< \pm 0.2$	deg
Circulator	no	NA
Harmonics at nominal power	<–40	dBc
Overall efficiency	>50	%
EMC compliance	IEC 610000-6-2, IEC 60204-1	NA
Input connector position	front	NA
Output connector position	top	NA
Output connector size	4.5–9	inch
Amplifier technology	Solid state	NA

Table IV.1: *Requirements of RF power amplifiers.*

IV.2 Low Level RF System (LLRF)

The Low Level RF (LLRF) System is required to control and to stabilize the RF phase and the voltage in the individual cavities. Every deviation from the specified values will lead to a deterioration of the beam dynamics performance which can lead to emittance growth and finally to beam losses. In addition, the LLRF system controls the dynamic tuner of each cavity to keep the frequency at the reference frequency to minimize the reflected power. Due to thermal drifts caused by different cooling water temperatures, flow changes or change in power level, the frequency of cavities can vary. The required phase and amplitude stability is given by beam dynamics simulations.

The LLRF system is based on MicroTCA.4 (μTCA4) standard. It is designed to provide amplitude and phase stabilities for the accelerating cavities of $\leqslant 0.2$ % and $\leqslant 0.1^{\circ}$, respectively. The LLRF-system controls RF fields of accelerating cavities regarding a stable master RF reference. To control the accelerating fields, pickup probes are mounted into the accelerating cavities. To monitor the forward and the reflected power emitted by the high power amplifier directional couplers are installed in the RF coaxial lines. The RF signals from the pickup probes and the directional couplers are sampled by fast ADCs to determine the RF phases and amplitudes of the cavities and to monitor the power in the cavities. The LLRF system provides the RF input-drive to the high power amplifier feeding the

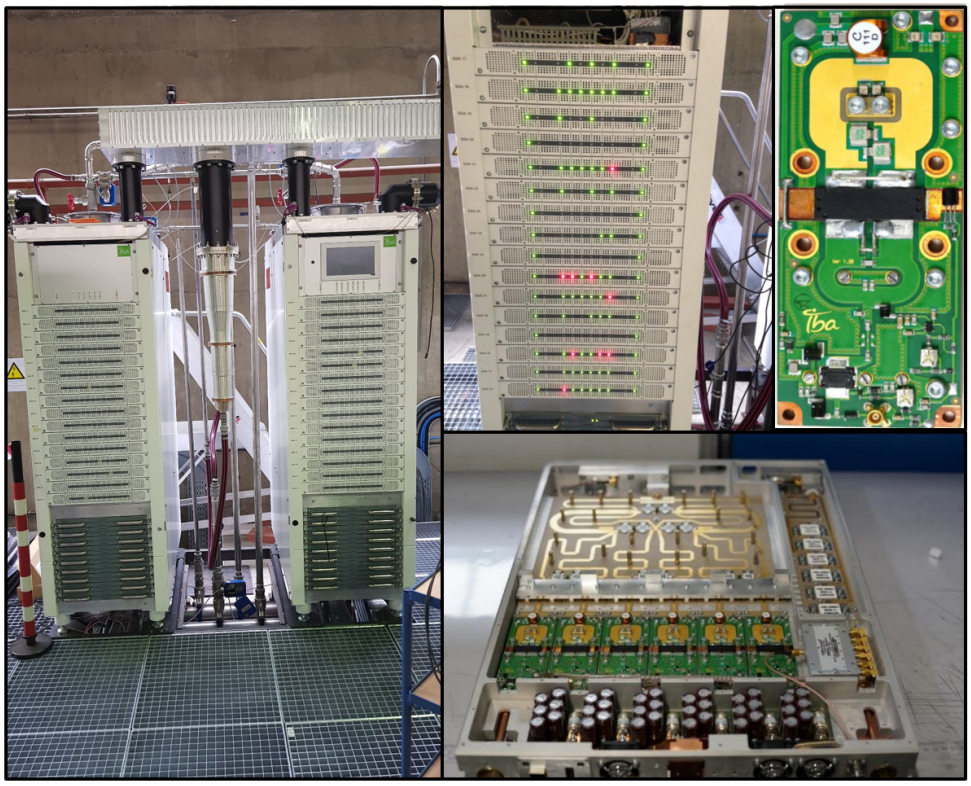

Figure IV.1: *192 kW, 176.1 MHz Solid State Amplifier (SSA) developed for the MYRRHA project.*

cavities. The layout of the LLRF system is depicted in Fig. IV.2. For commissioning of the accelerating structures, the drive power, the drive frequency and the repetition rate of the RF pulses are user adjustable. For accelerator operation, the cavity field gradients and phases can be user defined where the stability of the fields is ensured through digital real-time fast feed backs programmed in Field Programmable Gate Arrays (FPGAs).

For the HBS cavities the tuner driver system is controlled over ModBUS using Oriental Motors drivers and interfaces. Using identical systems with an identical technical base and concept will allow for a cross system spare-part-, handling, software-interface- and operational-concept. This will generate significant efficiencies during system integration into the control system for HBS as well as for the operation or any maintenance and hard- or software updates later.

A Rack Server running Linux connecting to the μTCA using PCIe runs the LLRF Software controls and allows for connectivity to the control system. Figure IV.3 shows the LLRF system for the first 5 cavities. What cannot be seen in these pictures are the individual driver approaches for the tuners which are a part of the LLRF system delivery. For communication of each LLRF system to the control system, minimum 2 Ethernet ports are required. The room temperature should be in the range +20 °C $\pm$ 5 °C. A temperature stability of $\pm$1 °C in the LLRF cabinet is desired to avoid uncontrolled phase drifts. The location should be dry, free of condensed water, clean and free of dust, mechanically stable, vibration and shock free. Access to the cabinet should be available from the front and the rear side. Strong air flows onto the RF cables have to be avoided. The system will be modularly built, with

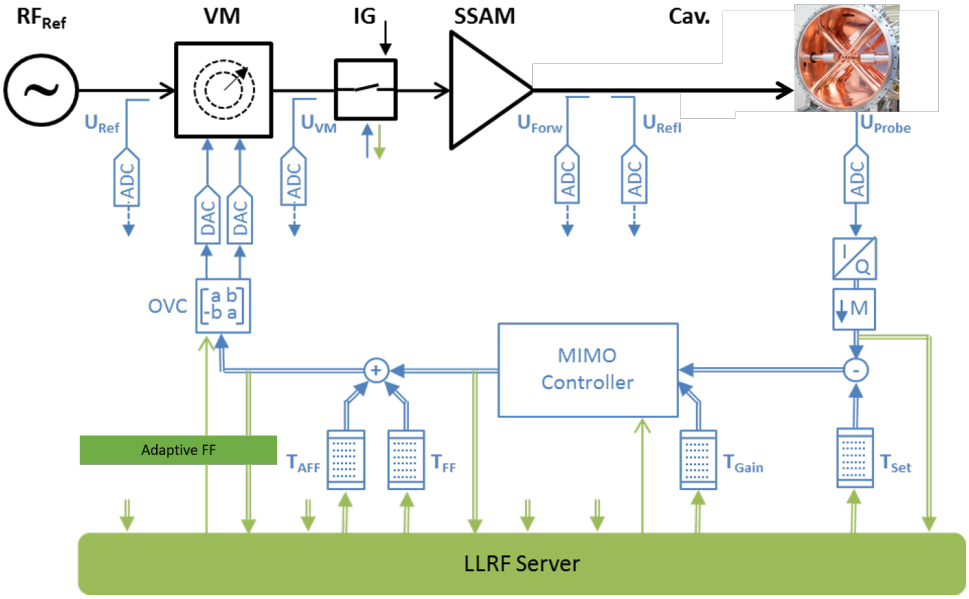

Figure IV.2: Scheme of the μTCA based LLRF system for HBS.

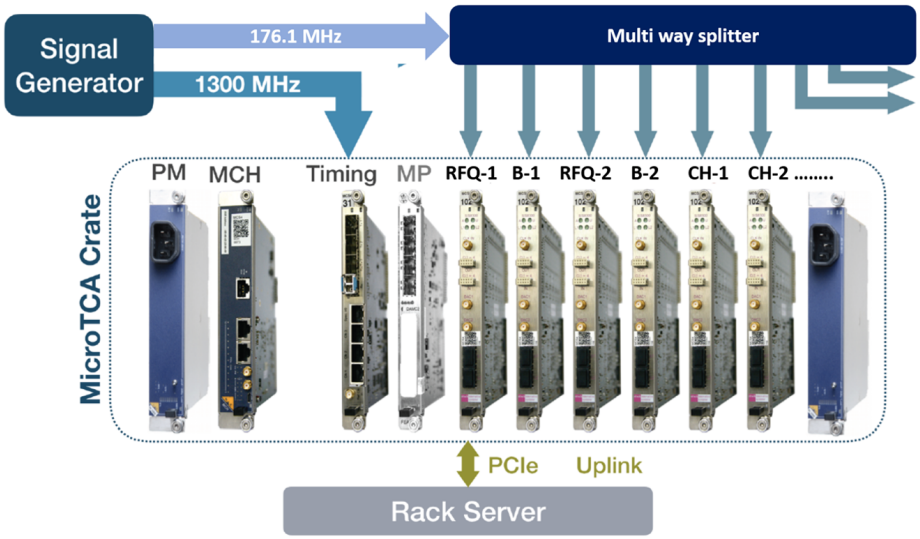

Figure IV.3: Schematic configuration of the LLRF system.

easy exchangeable hardware modules, and suited for future upgrades. Commercial-off-the-Shelf components are highly preferred. Table IV.2 summarizes the parameters of the LLRF-system.

Parameter	Specifications	Unit
Adjustable repetition rate	f_{rep}	0.5 Hz–1 kHz
Adjustable amplitude	dA/A	0.01 %–100 %
Adjustable Phase	φ	0 °–360°
Adjustable pulse duration (flat top)	Δ t_{top}	1 μs–10 ms
Adjustable filling time	Δ t_{fill}	0–200 μs
Adjustable start time RF pulse	t_0	0–10 ms
Stability amplitude	dA/A	$<$ 0.2 %
Stability phase short term	dφ	$<$ 0.1°
Stability phase long term	dφ	$<$ 0.5°
Master Oscillator (MO) RF signal	fMO	176.10 MHz
MO frequency stability (day)	Δ f/f	$<10^{-8}$/d
MO frequency stability (year)	Δ f/f	$<10^{-6}$/yr
Amplitude resolution rms	dA/A	$<10^{-4}$
Phase resolution rms	dφ	$<$0.02°
Max. amplitude drift with temperature	dA/A	$<2{\cdot}10^{-3}$/°C
Max. phase drift with temperature	dφ	$<$0.2°/°C

Table IV.2: *Requirements of the LLRF system.*

V.

BEAM DIAGNOSTICS, VACUUM & COOLING SYSTEMS

V.1 Beam Diagnostics

H. Kleines, O. Meusel, H. Podlech, M. Schwarz, J. Baggemann

The successful commissioning and operation of this Linac depends on the availability of suitable beam instrumentation. With a beam current of 100 mA, HBS places special demands on the diagnostic elements, both destructive and non-destructive. A fast commissioning phase and a smooth ramp-up to the maximum beam power require high quality beam measurements for comparison with the accelerator model. Safe and reliable operation in support of neutron research requires trustworthy systems that protect the accelerator hardware from beam-induced damage. The requirements for the HBS beam instruments were developed based on experience with similar facilities and Linacs, like pLinac at GSI (Darmstadt, Germany), ESS (Lund, Sweden) and MYRRHA (Mol, Belgium). The data of the beam diagnostics devices are permanently evaluated and embedded into the control and LLRF system. Every deviation from nominal parameters (e.g. beam position, beam current, phase width) can be corrected automatically to ensure optimal beam parameters. Additionally, the diagnostics system is connected to the Machine Protection System (MPS). In case of a registered anomalous beam behavior a emergency stop of the accelerator can be initiated. In our experience, there are space limitations for the placement of beam diagnostic elements in accelerators. This is also and especially true for HBS. These limitations are a result of optimizing the beam dynamics. The balance between the proper selection of beam diagnostic elements and the availability of sufficient redundancy must be carefully considered, especially for online beam diagnostics. On the other hand, sufficient bandwidth and computing capacity is required. Several devices can be used as beam position monitors, phase probes and current transformers. There is only a minor R&D effort for adapting the frequency or beam current. Most of the devices are available by commercial suppliers.

The first use of the beam diagnostic elements will be during the commissioning of the ion source (IS) and the low energy beam transport line (LEBT). Here, the main measurement parameters will be the beam current and the emittance. At HBS, two consecutive RFQs are used, including a MEBT (MEBT-1) in between for optimizing the matching into RFQ-2. Since the first RFQ has imposed a time structure on the beam pulses, Beam Posiion Monitors (BPMs) are used in MEBT-1 to determine the phase and the transverse bunch position. As the high beam current implies strong space charge effects and a corresponding beam divergence, compact elements and short longitudinal spacing of the beam guiding elements are crucial. The BPMs are therefore built into the magnetic quadrupoles of MEBT-1 to save space. Figure V.1 shows several Beam Position Monitors developed for the MYRRHA project.

These monitors can be used for HBS with some minor modifications.

Beam position monitors are an essential tool for the operation of a particle accelerator. As a non-destructive diagnostic device, they are used very frequently in nearly all linacs, cyclotrons and synchrotrons worldwide. Providing the beam's center of mass position as well as a monitor for longitudinal beam position and shape, the BPM is an indispensable component of beam diagnostic strategies. BPMs for several projects and a corresponding BPM test bench have already been developed by IAP and BEVATECH [SHK+19].

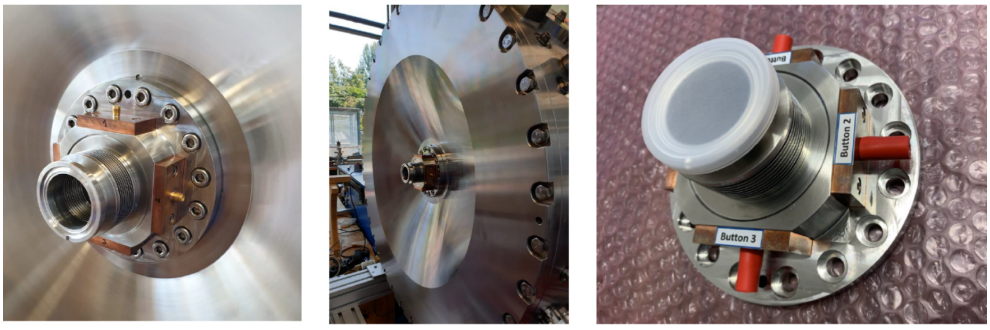

Figure V.1: *Beam Position Monitors developed for the MYRRHA project.*

V.2 Vacuum / Cooling system

J. Baggemann, O. Meusel, H. Podlech

The vacuum system has to ensure an appropriate pressure along the accelerator. The typical operating pressure is different for each section. The Low Energy Beam Transfer (LEBT) is normally operated at relatively high pressure between 10^{-5}–10^{-6} mbar. First, there is a certain gas flow from the proton source resulting in a higher pressure. Second, this higher pressure helps to suppress the space charge forces by space charge compensation. The optimum pressure has to be determined by simulations and hands-on optimization of the LEBT-section. In addition, it is possible to inject Argon or Xenon to improve the beam transport. The RF cavities require much better vacuum conditions to minimize the risk of sparking and ignition of discharges. While the RFQ needs an operation pressure of about $5{\cdot}10^{-7}$ mbar, the CH-cavities should be operated at $2{\cdot}10^{-7}$ mbar.

There are two possibilities to realize the vacuum system, a common vacuum line or individual vacuum pumps. Because of the extremely high reliability requirements a common vacuum line has been chosen for the MYRRHA project. This requires less vacuum pumps but leads eventually to a higher operation pressure. It also turned out, that the pumping speed is not sufficient to reach the required pressure using only one pumping port. Therefore, in case of HBS, it is recommended to use one turbo pump directly connected to the cavities. The RFQ requires 2 pumps with a pumping speed of 700 l/s. The CH-cavities require one pump with a pumping speed between 500 and 700 l/s depending on the cavity length.

The accelerator will have a closed cooling system using 1000 m^3 of deionized water. The tunnel, in which the accelerator is installed, will be equipped with the corresponding water supply, as well as a drainage system in case a pipe burst. The cavities will be heated to about 35 ^{o}C and on the hot spots, i.e. parts of indirect cooling, the temperature might reach 60 to 70 ^{o}C.

VI.
BEAM TRANSPORT AND MULTIPLEXING

A. Lehrach, J. Baggemann, O. Felden, R. Gebel

To achieve full performance with high beam brilliance at HBS, this facility simultaneously operates three neutron target stations in parallel with multiple neutron instruments attached. Each target station is operated efficiently to deliver different neutron pulse structures, which is achieved by generating an interleaved proton pulse structure that provides three different proton beam timing schemes. The distribution of the different proton pulse sequences to the target stations is accomplished by a proton beam multiplexing system that consists of a kicker magnet and a three-field septum magnet (TFSM). The integration of the multiplexer system at HBS including the design of a septum magnet is based on dedicated developments using a 45 MeV proton beam of the JULIC cyclotron at Forschungszentrum Jülich and scaled for the larger proton beam energy of 70 MeV at the HBS. In connection with the HBS multiplexer system, the HBS High-Energy Beam Transport (HEBT) beamline has been designed and the associated beam dynamics calculations performed [RFR+21].

VI.1 Multiplexer system

A test setup of the multiplexer system has been developed using the 45 MeV proton beam at JULIC. The focus was the development of a novel type of septum magnet based on permanent magnets, which has three different magnetic dipole field regions in close proximity. The conceptual layout of the multiplexer system is identical for both JULIC and HBS (Fig. VI.1). To separate the three different interleaved proton pulse sequences, a bipolar kicker magnet and a septum magnet with three different field regions have been developed and tested. The three field regions in the septum magnet are arranged so that the two outer field region deflects the particles further out to the left resp. right side. The middle region is a field-free region. The kicker magnet deflects the two lower frequency components towards the outer field regions of the septum magnet, while the higher frequency component passes through the system without beam deflection. This way, spatial separation of the three pulse trains is achieved. The angular separation of the resulting beam paths is achieved by the 17° deflection of the septum magnet and a 45° sector bending magnet (Fig. VI.1). The proton pulse scheme is realized by synchronizing the kicker magnet of the multiplexer setup with the Linac pulse generator.

In Fig. VI.2 the front face of the permanent magnet design for the three-field septum magnet (TFSM) can be seen. The final 3D design of the TFSM is displayed in Fig. VI.3. The design of this TFSM is scaled for higher beam energies of HBS by gradually adding additional permanent magnet layers.

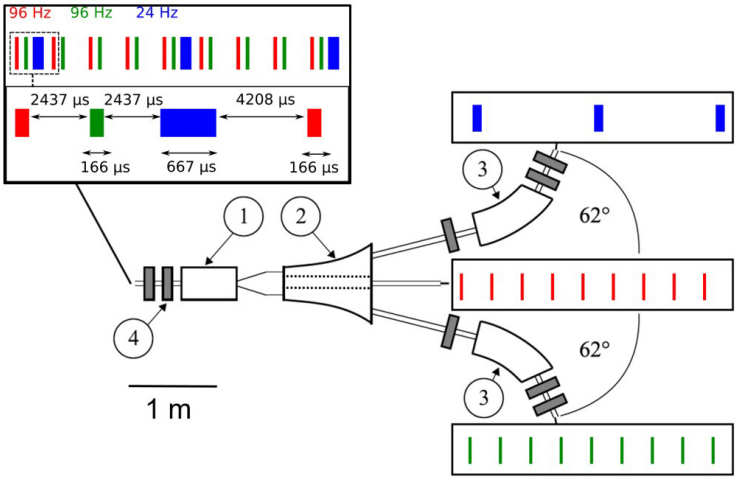

Figure VI.1: *Conceptual layout of the multiplexer system for HBS as partly realized at JULIC. 1: Bipolar kicker magnet, 2: Septum magnet with three different field regions, 3: 45° sector bending magnet, 4: Quadrupole magnet (all in gray). After the multiplexer system, the multiplexed pulse structure is unraveled into three beamlines inclined by 62° in total. The detailed timing scheme of the current pulse sequence is indicated with the two 96 Hz pulses with a length of 167 μs and the 24 Hz pulse scheme with 667 μs in red, green and blue, respectively.*

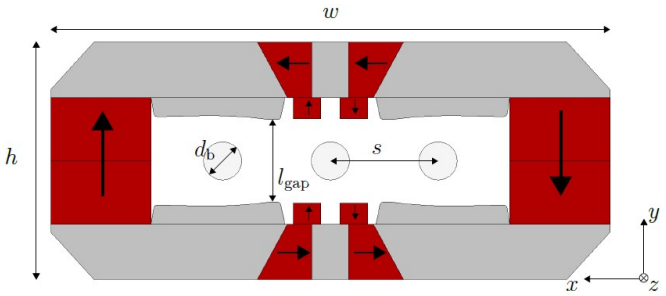

Figure VI.2: *Technical layout of the septum magnet front face. The width of the front face is ω = 353 mm and the height h amounts to 150 mm. The gap height l_{gap} = 52 mm, the beam diameter d_b = 24 mm with a beam spot separation of s = 68 mm. The red parts indicate SmCo magnets with B_r = 1.1 T, the gray parts show the magnet yoke. The direction of magnetization of the permanent magnets is indicated with arrows.*

A prototype of the first TFSM segment is shown in Fig. VI.4. It has been tested and shown the magnetization direction in the left, middle and upper part of the structure as simulated.

The TFSM is constructed to produce an integrated field of 306.5 mTm precisely without the necessity to consider potential manufacturing uncertainties. Obtaining $\int B_y dl$ = 306.5 mTm in the outer field regions as shown in Fig. VI.5 gives a deflection angle of $\alpha = \arcsin(\int B_y dl / B\rho)$ = 252 mrad. The field homogeneity in the outer field regions of the TFSM is 0.2%. In the centered zero field region,

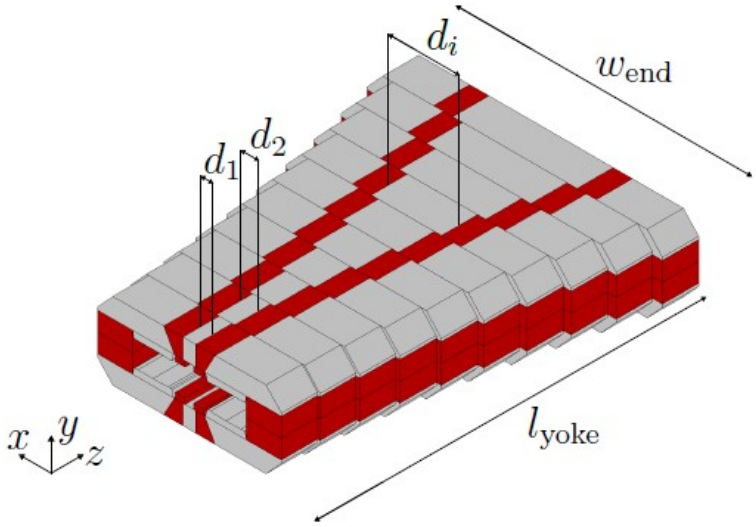

Figure VI.3: *3D drawing of the HBS septum magnet with yoke length l_{yoke} = 945 mm and maximum width at the end of ω_{end} = 676 mm. The septum magnet is segmented into 15 layers with a length of 63 mm each.*

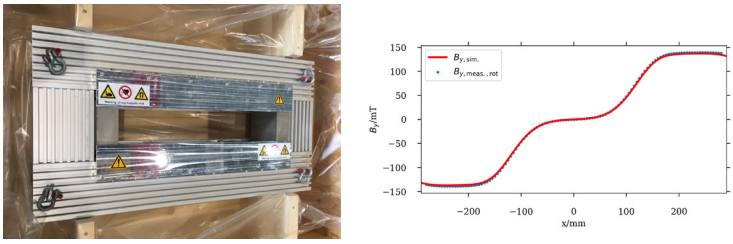

Figure VI.4: *Prototype of the TFSM segment (left) and simulated and measured magnetization within the TFSM (left).*

a maximum deviation of the integrated magnetic field of 2 mTm from zero is observed. Table VI.1 summarizes the parameter of the multiplexer system.

Table VI.1: *Parameter of the multiplexer, which includes a kicker magnet, and the TFSM.*

Parameter	Value
Deflection angle (kicker)	252 mrad (48)
Beam separation (front of TFSM)	68 mm
Yoke length TFSM	945 mm (15 layers)
Int. Field	306.5 mT m
Beam size	$\leqslant$ 25 mm

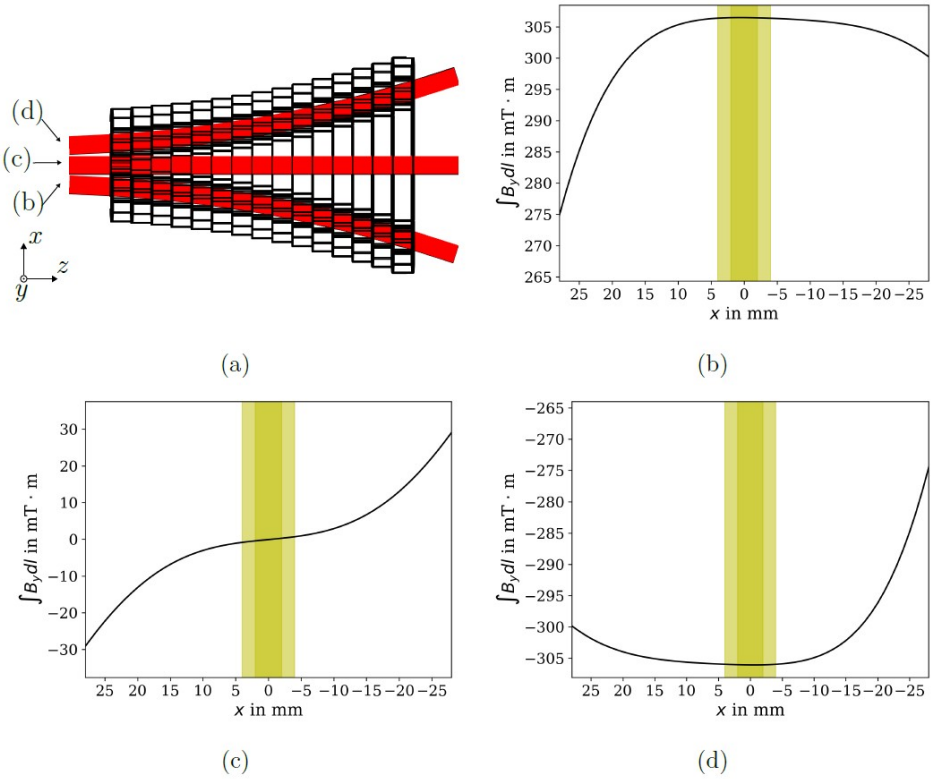

Figure VI.5: *(a): Integration planes for the calculation of the horizontal distribution of the integrated magnetic field of the HBS septum magnet. The integration planes follow the expected beam trajectories. The integration limits are set from z = -672 mm to z = 672 mm (z = 0 in the center of the magnet). (b)-(d): Integrated vertical magnetic field $\int B_y dl$ versus deviation along x from the center of the path following the different planes as indicated in (a). In each integration plane, a horizontally centered co-moving Cartesian coordinate system is used. The extent of the proton beam is indicated by the yellow shaded area: dark yellow: 2σ beam widths, light yellow: 4σ beam widths.*

During commissioning and step-wise beam energy enhancement, the number of TFSM layers can be gradually increased to roughly match the beam momentum/energy according to the values in Table VI.2. Fine adjustment of the beam rigidity has to be performed by adapting the beam energy at the exit of the Linac in the range of 3‰. The setup can be operated simultaneously with eight quadrupole magnets so that the two arcs sections of the multiplexer are achromatic, providing dispersion-free optics at the end of the magnet system.

Table VI.2: *Requirements for the three-field septum magnets with respect to beam momenta (beam rigidity and beam energy) for a certain number permanent magnet layers.*

Layer	Momentum / MeV/c	Rigidity /Tm	Energy / MeV
1	24,61	0,08	0,32
2	49,22	0,16	1,29
3	73,83	0,25	2,90
4	98,44	0,33	5,15
5	123,04	0,41	8,03
6	147,65	0,49	11,55
7	172,26	0,57	15,68
8	196,87	0,66	20,43
9	221,48	0,74	25,79
10	246,09	0,82	31,73
11	270,70	0,90	38,27
12	295,31	0,99	45,37
13	319,91	1,07	53,04
14	344,52	1,15	61,25
15	369,13	1,23	70,00

VI.2 High energy beam transport (HEBT)

The HEBT is the proton transport beamline that connects the Linac with the individual target stations at HBS (Fig. VI.6). It includes the multiplexer system that is part of the design of the HEBT and a beam dump.

VI.2.1 Beamline layout

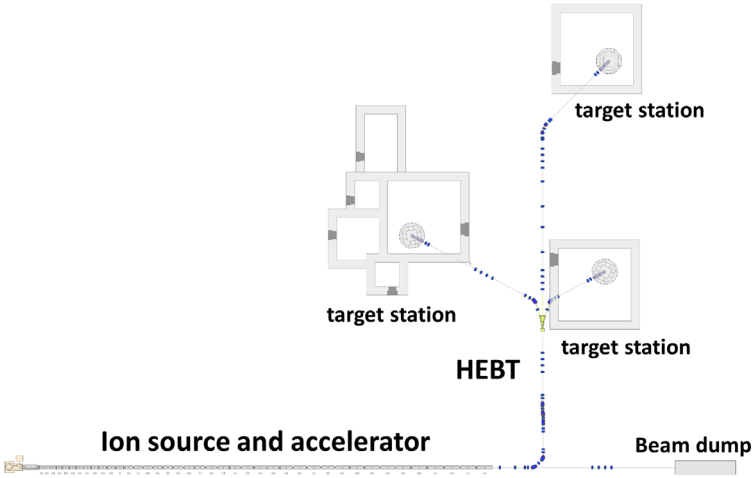

Figure VI.6: *Schematic top view of HBS, including the front end, Linac and High-Energy Beam Transport (HEBT) beamline to the individual target stations. The detailed location of magnets is shown in Figs. VI.7 and VI.8.*

The geometry of the HEBT is determined by the location and arrangement of the HBS target stations in the three experimental halls, based on the space requirements of the neutron targets, instruments and the corresponding building locations and dimensions. The HEBT can be structured into different sections. The first section bends the beam horizontally by 90° from the Linac towards the experimental section. The second section then deflects the beam vertically by 90° from the ground floor into the basement in order to increase radiation safety. Both sections consist of two double-bent achromats, based on two 45°-sector bending magnets, each equipped with five quadrupoles. At the basement, the beam is transferred to the third section of the straight HEBT beamline. Here, a quadrupole triplet with four quadrupoles is used to focus the beam into the multiplexer. The beam in the straight beamline passes only the first two quadrupoles of the multiplexer (Fig. VI.7).

To guide the beam trains also into the two outer field regions of the TFSM, a kicker magnet is used to apply an angle kick to the beam. The septum magnet separates the beams for delivery to the left and right target stations. The multiplexer section also provides an achromatic optics by adding three quadrupoles to the additional 45° bending magnet for the two outer beam lines. In the third section after the multiplexer, where the three beamlines are separated, a matching section consisting of a triplet with four quadrupoles is used to match the beam into the three beam transport sections. The straight beamline consists of two FODO (focusing-drift-defocusing-drift) structures. The cell length of each FODO cell is 5.6 m, resulting in a total length of roughly 11.2 m. The next triplet of the straight

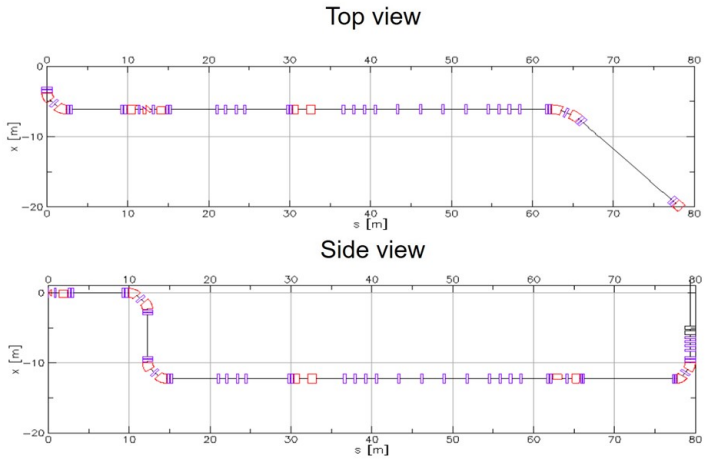

Figure VI.7: *Top and side view of the straight HBS High-Energy Beam Transport (HEBT) beamline. The drawing shows the three different sections and the respective quadrupole (pink), dipole (red), and scanner dipole magnets (black). The multiplexer is located at roughly 31m in this representation.*

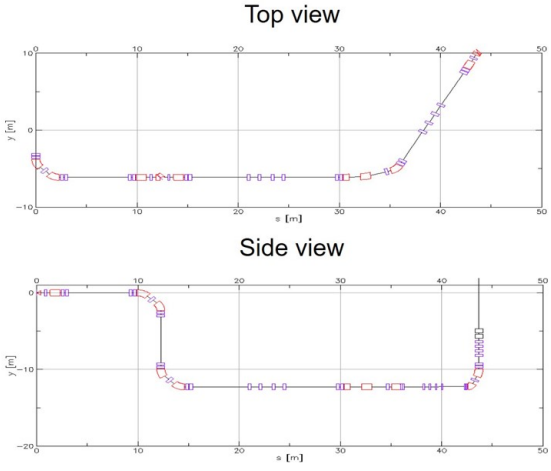

Figure VI.8: *Top and side view of the left HEBT beamline. The drawing shows the three different sections and the respective quadrupole (pink), dipole (red), and scanner dipole magnets (black). The multiplexer is located at roughly 31m in this representation.*

beamline focuses the beam into a 45° horizontal bending section, before the beam reaches the final achromatic section, which guides the beam vertically by 90° up to the neutron target station. In front of the targets, a quadrupole triplet is installed to adjust the focusing of the beam on target. Vertical and horizontal dipole scanner magnets are used to spread (beam painting) the beam equally over the neutron target for optimize heat distribution. From the last vertical bending section on the three beamlines are identical again. Since the right resp. left beamlines to the neutron target stations are significantly shorter than the straight beamline (Fig.VI.6), the FODO cells are removed. As an example, the top and side views of left beamline are plotted in Fig. VI.8.

In the present arrangement of the neutron target stations (Fig. VI.6), the right beamline looks basically the same as the left one, except that the third section is shorter. Therefore, the triplet at the entrance of the third section can be adjusted accordingly to focus the beam into the vertical bending section. If the position of the neutron target needs to be shifted again to further optimize the experimental setup, the beamline can easily be adopted by adding FODO cells in the third section and adjusting the final horizontal 45° bend in the straight beamline or the bending angle in the dipole behind the multiplexer in the two outer beamlines. The chosen beamline concept provides maximum flexibility to adopt to modified target positions.

VI.2.2 Beam optics

The beam optics of the straight (Fig. VI.9) and left beam line (Fig. VI.10) including the magnet arrangement are shown. The following beam parameters have been considered for all presented beam calculations at the entrance of HEBT:

- Beam current: I=100 mA protons
- Kinetic beam energy: T = 70 MeV; magnetic rigidity: bρ = 1,25 Tm,
- Transverse beam size: $\sigma_{x,y}(0)$ = 1,6 mm
- Geometric transverse beam emittance: $\epsilon^{g}_{x,y}$ = 2.54 mm mrad (rms),
- Normalized transverse beam emittance: $\epsilon^{n}_{x,y}$ = 1 mm rad (rms),
- Momentum spread: $\Delta p/p$ = 0.5 %,
- Beta function: $\beta_{x,y}(0)$ = 1,1 m,
- Dispersion function $\eta_{x,y}(0)$ = 0 m.

The reach the specified values, the Linac has to be adjusted accordingly. The beam emittance could eventually be reduced by a beam collimation system and the initial Beta functions and momentum spread adjusted by adding a matching section consisting of a quadrupole triplet and a bunch rotator between the Linac and the HEBT. As can be seen, the optics in front of the multiplexer is similar for both beamlines. It includes a horizontal 90° bend from the Linac into the experimental section and furthermore two vertical bends to transfer the beam to the basement floor. The left beam line has an additional bend in the TFSM at about 50 m and the straight beamline a 45° bend at roughly 79 m towards the neutron target. The last vertical 90° bend at roughly 67 m (left beamline) and about 100 m (straight beamline) transports the beam from the basement up to the neutron target stations.

The corresponding beam dynamics calculations for the different beam line sections have been performed with the Bmad library [Sag06] to optimize the optical setting.

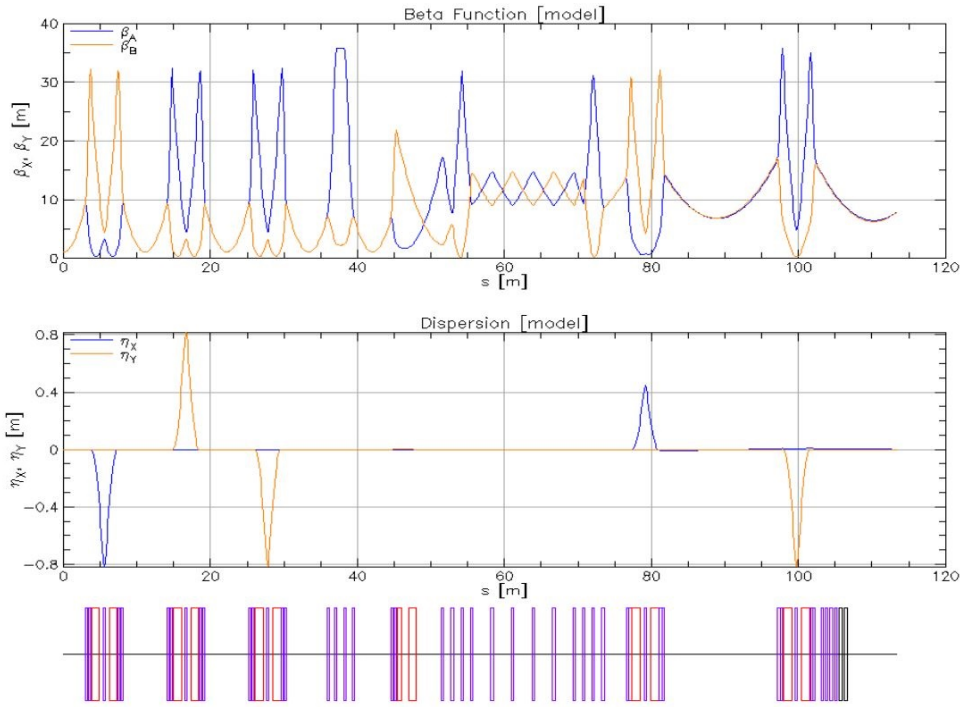

Figure VI.9: *Horizontal and vertical Beta function $\beta_{x,y}(s)$ (upper plot), and dispersion function $\eta_{x,y}(s)$ (middle plot) versus longitudinal position s along the straight HEBT beamline. The lower plot shows the magnet arrangement with quadrupoles in pink, dipoles in red, and scanner dipole magnets in black. The multiplexer is located at roughly 50 m.*

VI.2.3 Beamline acceptance

The geometric acceptance of the beamline can be estimated with the calculated Beta functions and dispersions along the beamline[RFR+21] . The aperture of the magnets have been chosen to be 60 mm. In regions without dispersion ($\eta_{x,y}$ = 0), the maximum Beta function is $\beta_{x,y}$ ⩽35 m, leading to a transverse beam size of $\sigma_{x,y}^{max}$ ⩽9,5 mm with a transverse emittance of $\epsilon_{x,y}^{g}$ = 2,54 mm mrad (rms). This corresponds to a 6σ beam that fits into the beamline. In regions with maximum dispersion ($\eta_{x,y}$ ⩽ 0.8 m), the maximum Beta function $\beta_{x,y}$ ⩽5 m. With a momentum spread of $\Delta p/p$ = 0.5 %, a 6σ beam also fits into the aperture of the magnets. The gap height of the TFSM is only l_{gap} = 52 mm thus offering a safety margin for the 24 mm beam. The actual 6σ beam has an elliptical shape with an extent of 24 mm in the vertical and 8 mm in the horizontal plane.

The effect of the field quality of the TFSM on the transmission through the HEBT has also been investigated in detail by particle tracking studies. The simulated beam transmission through all three field regions is close to 100 %. The dynamic acceptance of the beam line has also still to be further optimized including multipole corrector fields. So far, only artificial multipole distributions of magnets have been assumed without any optimization. An average beam loss in terms of power of 38 W m^{-1} is obtained before the TFSM. For the straight beamline after the TFSM, one gets 22 W m^{-1}, whereas the left and right beamline yield 115 W m^{-1} each. For the calculations an average beam power of 300 kW and 100 kW is considered before and after the TFSM, respectively. Note that a straight forward

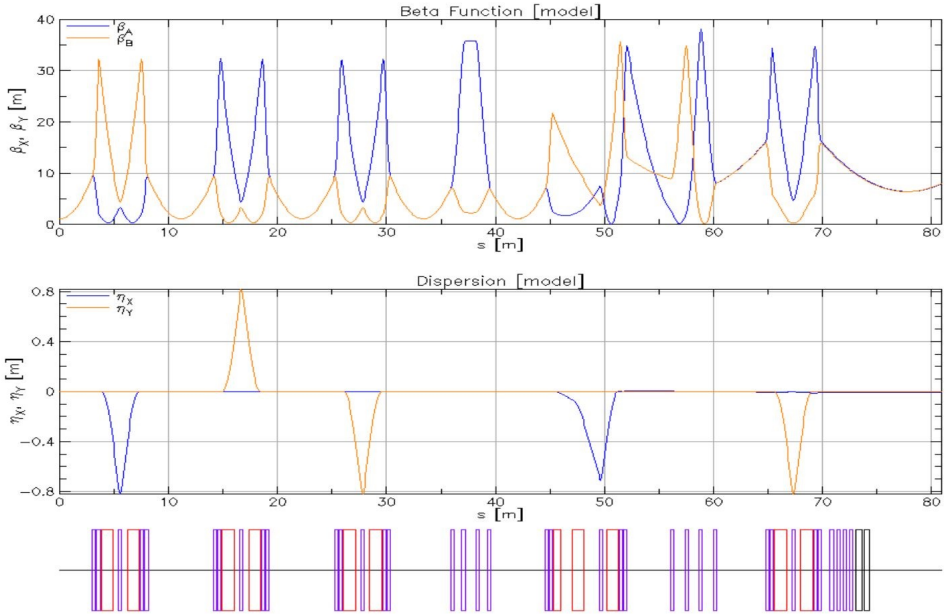

Figure VI.10: *Horizontal and vertical Beta function $\beta_{x,y}(s)$ (upper plot), and dispersion function $\eta_{x,y}(s)$ (middle plot) versus longitudinal position s along the left HEBT beamline. The lower plot shows the magnet arrangement with quadrupoles in pink, dipoles in red, and scanner dipole magnets in black. The multiplexer is located at roughly 50 m.*

approach to reducing the average beam loss by the use of a 100 mm aperture diameter throughout the HEBT (instead of 60 mm) as well as a beam scraper in the beginning of the HEBT, which limits the beam size to 6σ, yields an average beam loss below $1\,\mathrm{W\,m^{-1}}$ in all beam lines.

VI.2.4 Quadrupole and correction magnet layout

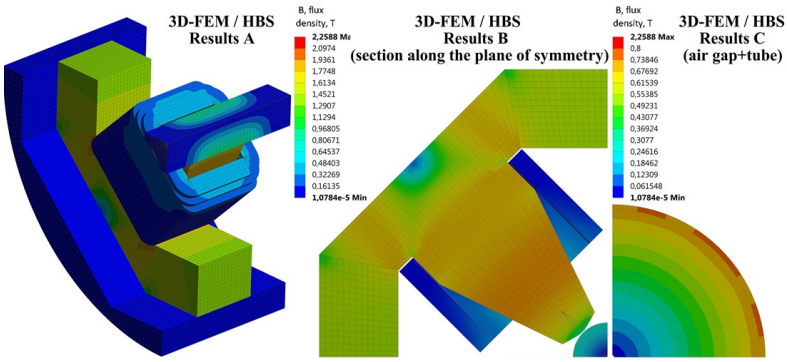

Figure VI.11: *Field calculations for a quadrupole including a horizontal and vertical correction dipoles.*

A compact design including horizontal and vertical correcting dipoles in quadrupole is currently under investigation (Fig. VI.11). It is based on field calculations, which have finally to be verified by beam dynamics calculations. The optimization of multipoles and the investigation of multipole corrector magnets are still ongoing.

VI.2.5 Beam instrumentation

Standard beam instrumentation equipment will be used to monitor and control beam properties in the HEBT. A similar beam instrumentation concept as used for the ESS target beamline will be adopted and further optimized with respect to beam performance and cost.

Each beam delivery quadrupoles are equipped with a beam position monitor (BPM) and a beam loss monitor (BLM). This enables to optimize the magnet setting. A beam current monitor (BCM) is installed after each beam line section to measure beam transmission and monitor the total beam loss. To ensure that the beam delivered to the target has the correct distribution and intensity and does not damage the target, local monitoring of the beam density is required.

Since protection of the target is of great importance, redundant methods will be used. A combination of secondary emission monitor (SEM) grids and non-invasive profile monitors (NPM), which provides an image of gas-induced fluorescence, offers complementary choice. Similar systems for beam monitoring are also required for the beam dump during commissioning and beam-setup. To reduce beam losses in the HEBT due to the formation of beam halos to an acceptable level, the transverse beam halo should also be measured and cleaned. Therefore, a beam cleaning approach with multiple beam collimators, non-invasive profile monitors (NPM), and possibly wire scanners is foreseen. To secure the target on emergency of any damage by the pulsed proton beam a kicker magnet will be installed in the HEBT to redirect the beam in case of failure to an appropriate beam dump. On the other side a fast shutter before the target will secure the accelerator structure from possible vacuum loss or damage by target water leakage.

VI.3 Beam dump

VI.3.1 Beamline layout and beam optics

The beam dump will be located in straight direction from the Linac. Therefore, the first dipole has to be switched off to reach the beam dump. To adjust the beam size to the requirements of the beam dump of roughly 4 m (rms), also the first two quadrupole of the achromat should have zero field and a long drift section of roughly 20 m is needed to increase the beta function above 500 m. The magnet arrangement and the optical functions are shown in Fig. VI.12.

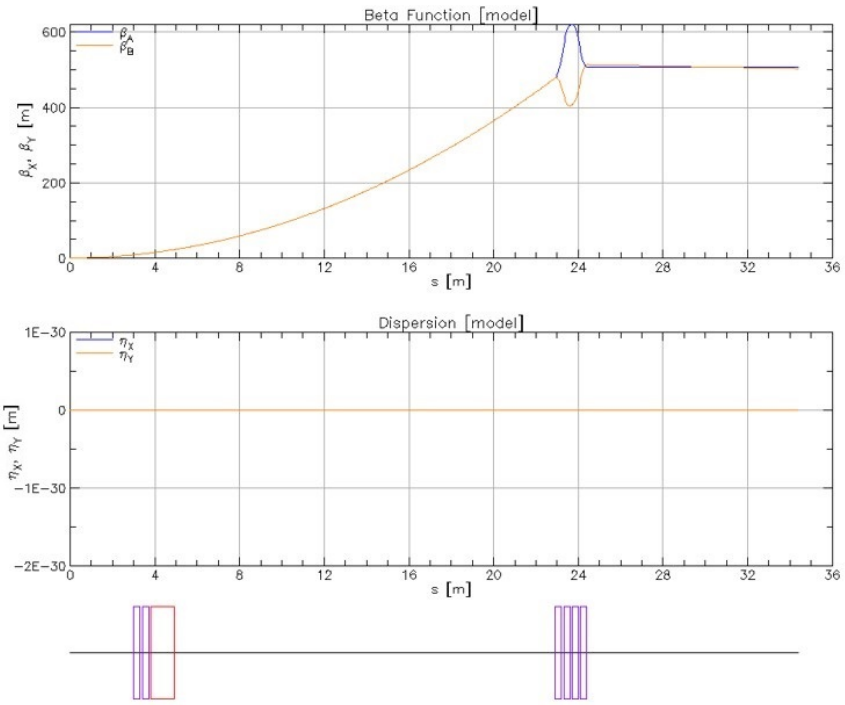

Figure VI.12: *Horizontal and vertical Beta function $\beta_{x,y}(y)(s)$ (upper plot), and dispersion function $\eta_{x,y}(s)$ (middle plot) versus longitudinal position s along the beam line to the beam dump. The lower plot shows the magnet arrangement with quadrupoles in pink and dipoles in red*

VI.3.2 Beam dump layout

The terms of reference for the development of a proton beam dump is based on the general beam parameters for the HBS in a conservative case of a continuous loading mode of an internal surface of a dump with a centrally-symmetric proton beam with an average power of 1 MW and a normal distribution with $\sigma = 0.04$ m. No sub-critical, critical or overcritical thermal-mechanical stresses and elongations in the beam dump and its periphery should appear , to ensure a smallest possibility for a charged high energetic particle to leave an artificial contour of guaranteed dumping. The power

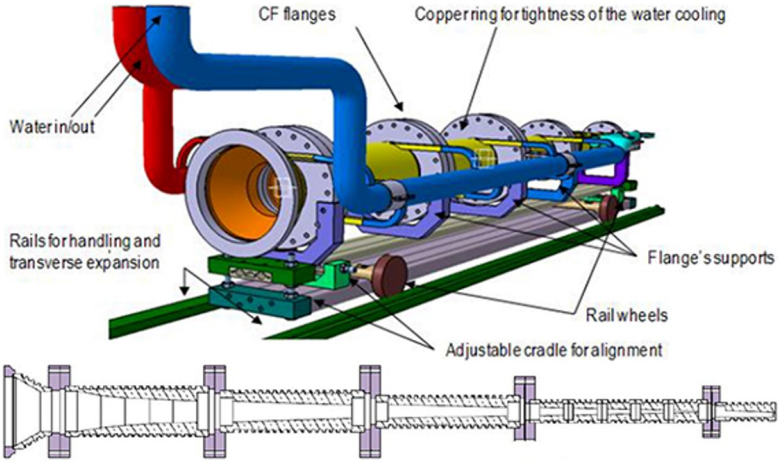

Figure VI.13: Schematic representation of the main elements of SPIRAL2 / SAFARI beam dump design [MSL+12].

could reach up to 1 MW during the adjustment and maintenance of the accelerator or in the case of a technical accident. Based on the general technical requirements, the SPIRAL2 / SAFARI concept shown in Fig. VI.13 [MSL+12], which is in operation since 2018 and adopted in another SAFARI beam dump at the ESSB accelerator [MSG+12], was used as the basis for the HBS beam dump design described in the following.

3.2.1 Features of design elements and assembly technology

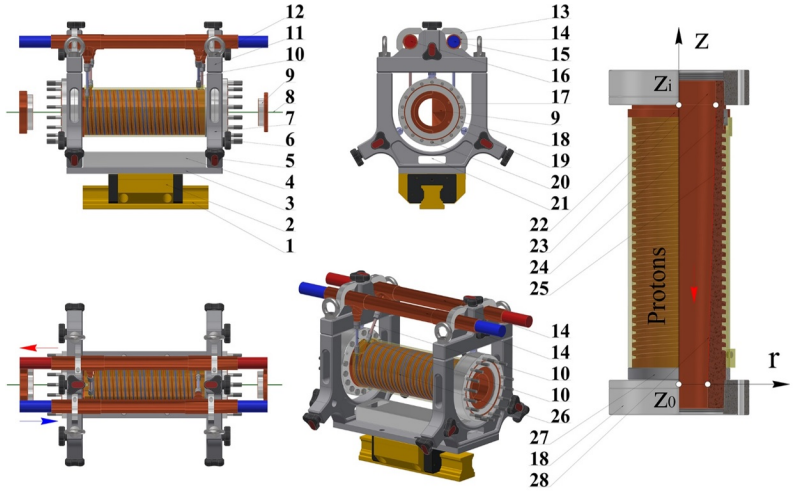

Figure VI.14: Main elements of the modified design of a regular SPIRAL2 / SAFARI beam dump segment adopted to the beam parameters of the HBS neutron source.

The modified design of the SPIRAL2 / SAFARI beam dump, adopted to the HBS neutron source characteristics, consists of a regular middle part and irregular end segments. The regular middle segment

has a length of 0.34 m with an internal incoming diameter of 0.09 m and an external diameter of 0.115 m. The specific elements of the middle part as shown in Fig. VI.14 are composed of an optically adjustable high precision steel monorail with a width of 0.055 m and a rail length of 3.836 m, operating temperature up to 353 K (1), a high precision pre-stressed steel ball bearing runner platform (2), an aluminium mounting plate (3), aluminium housing (4), steel manual mechanism for radial feed of a high precision pre-stressed (5), steel manual mechanism for locking a high precision clamp (6), the stationary part of the aluminium frame of a modified lathe steady rest (maximum diameter of the standard model of 0.195 m) (7), geodesic alignment laser (8), removable copper calibration disk with a central aperture withdiameter of 0.25 mm (9), channels connecting the dump cooling contour with the coolant main inlet / outlet routes (10), removable part of the aluminium frame of a modified lathe steady rest (11), steel eye bolts (12), aluminium holder of the central coolant channel (13), copper thick-walled seamless central channels for coolant in- and outlet (14), inlet / outlet coolant for distilled and filtered water [MSH17] (15-16), copper sealing ring (17), steel fitting with an external positioning groove and tapered thread (18), freely rotating steel axial symmetric element of the precision pre-stressed clamp (withstanding weight of at least five times the weight of the segment of 500 N) (19), steel fasteners for fittings, installed with a change of direction in places, where there is a deficit of a space for mounting (20), opening of the lathe steady rest (21), casing hot pressing stroke limiter (22), cylindrical precision surface of the dump (23), steel engineering key, acting as a guide during the hot pressing of the casing and as a mechanism, blocking an unwanted rotation of it in the operating mode (24), two-way counter-directional helix channel for cooling water [MSH17] (25), copper casing with flanges and thickening for the engineering key groove, performed by turning and milling (26), steel ring for locking the return stroke of the casing in the operating mode (27) and internal contour of the copper [KKMG08] dump (28) according to Fig. VI.15

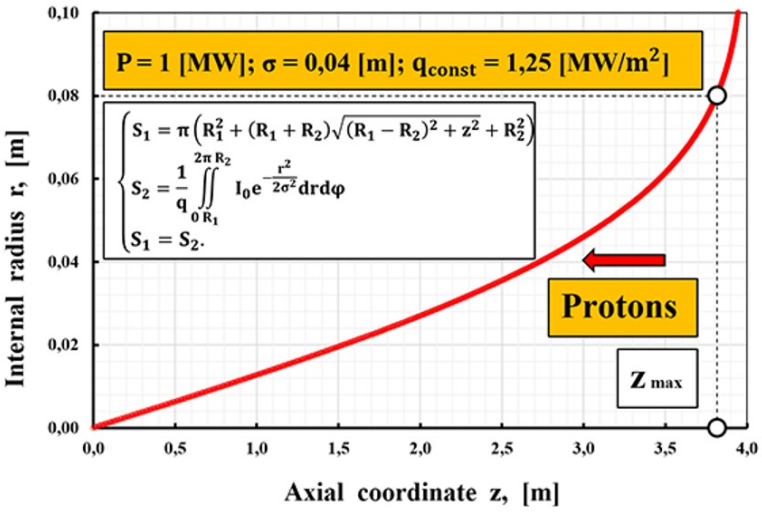

Figure VI.15: Theoretical internal beam dump contour calculated numerically for uniform power distribution along z.

The theoretical internal contour of the beam dump is calculated numerically for an uniform distribution of the heat flux along the longitudinal axis z and a power density of $q_{const} = 1.25\,\mathrm{MW/m^2}$. This ensures a maximal wall temperature of 358 K under the boundary conditions presented above [MSG$^+$12]. For beam dump covering $2\,\sigma$ of the beam, a length of the beam dump of 3.8 m can be derived from the function z = f(r) presented in Fig VI.15

In order to prove the feasibility of the heat removal for $q_{const} = 1.25\,\mathrm{MW/m^2}$, a two-way coupled

CFD-FEM analysis of the central segment was performed including the temperature fields of the beam dump walls as well as the temperature and the pressure of its cooling liquid. This is the basis of all subsequent calculations of the beam dump design. The simulated model is a simplified central segment of the beam dump consisting of 5 elements (1 (Stainless Steel) – 2 (Cu) – 3 (Cu) – 4 (H_2O) – 5 (Stainless Steel)), subjected to a stationary but geometrically inhomogeneous heat flux with $q_1 = 0.05 \cdot q_{const}$, $q_2 = 1.00 \cdot q_{const}$, $q_3 = 0.10 \cdot q_{const}$. The ends were assumed to be insulated thermally and on the periphery a convective heat removal surface was assumed that is coupled to the environment represented with T_{ref}. The central element of the dump responsible for heat removal is a bidirectional (Inlet A+ / Inlet B-) channel with continuously circulating water (T_{InletA^+} / T_{InletB^-}; U_{InletA^+} / U_{InletB^-}). The simulation parameters are summarised in tables VI.3 and VI.4.

Table VI.3: *Important geometric parameters of the simulated model space.*

L_1 [m]	L_2 [m]	L_3 [m]	R_1 [m]	R_2 [m]
0.03	0.34	0.03	0.0575	0.045

Table VI.4: *Thermophysical properties of the material of structural elements and the conditions of its loading.*

Position of the structural element	1 2 3 5	4
Thermophysical property	$k_{1,5} = 15 \frac{W}{mK}$ $k_{2,3} = 401 \frac{W}{mK}$ $h = 28.41 \frac{W}{m^2 K}$	$\rho = 998.2 \frac{kg}{m^3}$ $Cp = 4182 \frac{J}{KgK}$ $k = 0.6 \frac{W}{mK}$ $\mu = 0.001 \frac{kg}{ms}$ $I_{Turbulencek-\epsilon} = 0.05$
Loading	$U_{Wall} = 0.0 \frac{m}{s}$ $T_{ref} = 294K$ $q_1 = 62.5 \frac{kW}{m^2}$ $q_2 = 1250 \frac{kW}{m^2}$ $q_3 = 125 \frac{kW}{m^2}$	$U_{InletA^+} = 7.0 \frac{m}{s}$ $U_{InletB^-} = 7.0 \frac{m}{s}$ $P_{OutletA^+} = 101325Pa$ $P_{OutletB^-} = 101325Pa$ $T_{InletA^+} = 294K$ $T_{InletB^-} = 294K$

The results of the CFD /FEM calculation show that the empirical value $q_{const} = 1.25 \frac{MW}{m^2}$ recommended in [MSG+12] is reliable and can be used for more technically advanced optimisation calculations since the maximum water temperature of 366 K in the channel subject to the specified initial and boundary conditions is in good agreement with the expected value of 358 K. Additionally, the calculated value of the water pressure of 0.75 MPa in the channel is technically reliably, although it exceeds the desired value of 0.5 MPa. The maximum wall temperature of the dump of around 1100 K is located at the heat flux change from q_1 to q_2 and q_2 to q_3. To reduce the maximum temperature further optimisation will be done by increasing the values of L_1 and L_3 by a factor of e.g 2 - 2.5 times thus increasing the surface area and reducing the heat load. This would also lead to a possible reduction of the pressure in the channel by reducing the mass flow rate (or velocity) of the water in both inlets.

The total length of the beam dump for HBS has a length of 4 m with 10 sectors of equivalent length and a total mass of 520 kg. The concept of the design of the tail segment is shown in Fig. VI.16. The CFD / FEM calculations show that a heat load of $q_{const} = 1.25 \frac{MW}{m^2}$ can be removed with the

adopted beam dump design of SPIRAL2 / SAFARI but further optimization processes need to be done in order to reduce the maximum temperature. A full analysis and subsequent optimization of the whole beam dump will performed at a later stage.

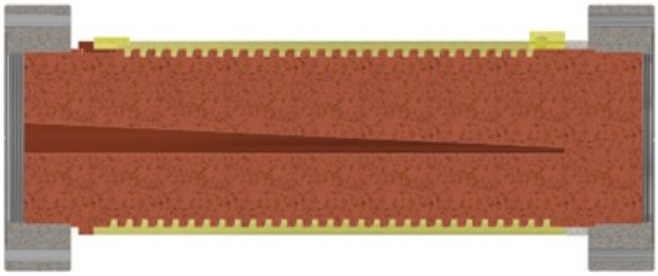

Figure VI.16: Concept of the design of the tail segment of the beam dump.

3.2.2 Adjustable mobile platform

In order to ensure the convenient maintenance, adjustment, operational aggregate and over-aggregate assembling and disassembling of the long-length beam dump, the concept of a compact mobile beam dump platform was developed as shown in Fig. VI.17.

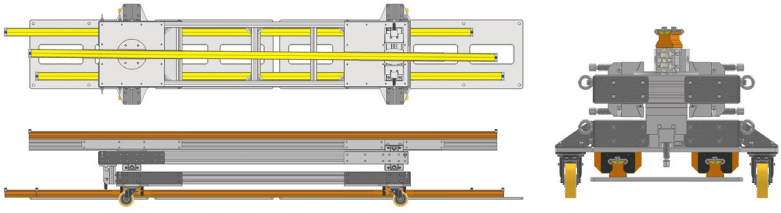

Figure VI.17: Design concept of the mobile platform for placing a modular beam dump with a reinforced steel monorail.

The platform is a two-level frame made of hot-extruded aluminum profiles, reinforced in places of insufficient rigidity or increased responsibility with steel plates. The lower level of the frame has 8 support points in the lower hemisphere, 4 of which serve for precise longitudinal movement of the beam dump and 4 are service points. For ease of installation, dismantling and transportation, the lower level of the frame is equipped with transportation crane rings. In order to organize the spatial adjustment of the beam dump, the platform is equipped with a system of micro-screw mechanisms for precision rotation, lifting and movement. Adjusting rotation and transverse movement units are installed on the upper conditionally autonomous frame level together with additional transport crane rings. The installation of the proton beam dump, pre-assembled on a precision steel monorail, reinforced to increase the longitudinal rigidity with an aluminum hot-pressed profile, is carried out by an independent lifting mechanism, located in close proximity to the casemate of the radiation protection of the unit, after which the platform can be brought into the working position by moving it into the casemate cavity manually along the precision guides and subsequent locking. The overall dimensions of the platform are 800 x 600 x 3800 mm^3 and the total mass is 500 kg.

VII.
CONTROL / OPERATION SYSTEMS

VII.1 Overview

The HBS accelerator control system consists of components and tools, which connect all HBS equipment and present a homogenous and ergonomic interface to operators, engineers and physicists enabling safe and reliable operation of the HBS. This comprises

- software,
- electronics,
- communication systems and
- intelligent control or diagnostic devices

The HBS control system is responsible for all interlock and local control functions, too. To minimize the overall development effort, several decisions regarding design and development strategies have been made:

- EPICS [EPI] and Control System Studio (CSS) [CSS] have been selected as the control system framework providing device abstraction, communication, central services and HMI, since both are most commonly used in the physics accelerator community and since they are well supported open source toolkits. Also, there is EPICS/CSS experience at the IKP and JCNS is building up EPICS experience due to its involvement in the ESS. Linux will be used as the operating system platform.
- Commercially available systems and components should be used as much as possible and the number of different vendors and standards should be minimized. As an example, Simatic S7-1500 PLCs in combination with ET200pro, ET200SP and ET200MP decentral periphery systems as well as PROFINET and IO-Link communication have been selected as the PLC platform, since they are well-established at JCNS and market-leading.
- It is intended to start cooperation with scientific partners for the implementation of subsystems, e.g. the machine protection system or the LLRF system, with the goal of sharing as much as possible from existing systems at the partner labs. Potential partners are ESS, PSI, MYHRRA and DESY.

From a control system point of view, the HBS can be subdivided into the HBS machine consisting of ion source, accelerator system (LINAC, HEBT,...), target stations and conventional facilities (cooling

water, pressed air,. . . .) which is responsible for neutron production, and the instruments using these neutrons for research. For the HBS machine a central control room is foreseen that is permanently manned with operators, whereas instruments are locally controlled by dedicated measurement scripts and programs. Ideally there will be one integrated control system for the HBS machine in order to reduce the development efforts and support a homogeneous user interface. Since the Ion source and the conventional facilities will be provided by external partners, it is quite likely that they will come with their own control systems. In order to reduce the overall costs, these control systems will not be replaced but extended by gateway functions to the integrated HBS control system.

Operation of instruments is typically fully automatic, requiring presence of instrument users or scientists only for measurement definition and start, for development and test of dedicated scripts or for sample change. From the perspective of the control system, instruments and HBS machine are only loosely coupled via the timing system, personnel protection system, vacuum system and exchange of some information on the machine state (e.g. pulse charge and proton energy, . . .). Due to this loose coupling and the different mode of operation, it is foreseen to have individual control systems for each instrument, independent of the integrated control system of the HBS machine. Since requirements are different, the control systems of the HBS machine and the HBS instruments will use different control system technologies and implementation approaches. JCNS has been developing neutron instruments since decades and operates 12 instruments at its main outstation at the FRM-II in Garching. All these instruments share the same architecture and technologies for the instrument control systems, based on TANGO [TAN], NICOS [NIC] and Siemens S7 PLC and motion technology. In order to minimize the implementation efforts by relying on the existing developments and the support of trained personnel, all HBS instrument control systems shall be implemented with to the same architecture and the same technologies. Reusing the existing framework with out-of-the-box software components will lead to an extremely cost-efficient implementation of the instrument control systems.

The following sections describe architecture, functionality, technologies and implementation issues of the accelerator control system. Since it will be implemented as an integrated control system for the accelerator and the three target stations, all basic considerations and decisions apply also to the target station control, which is covered in a separate volume.

VII.2 Accelerator Control System Architecture

VII.2.1 Vertical structure

The HBS machine and instrument control systems will be designed as distributed and object-oriented systems. Despite the different implementation, all will follow the same classical three-tier architecture as indicated in Fig. VII.1.

- At the lowest level, the **resource tier** facilitates the access to the front-end equipment of the HBS machine enabling direct equipment control and data collection. Conceptionally, the resource tier presents a device abstractions of front-end equipment to the middle tier. For the connection of the front-end equipment a wide range of interface standards has to be supported.

- The **middle tier** implements the application logic of the control systems, e.g procedures for automatic start up, shutdown or auto-tuning. Databases for configuration, archived process variables (PVs) and logging information reside at this tier. A name service implemented at the middle tier provides location transparence for the devices exported by the resource tier.

- The **presentation** tier is responsible for the HMI (Human Machine Interfaces) that enables machine and instrument operation for operators, engineers and physicists. At the presentation

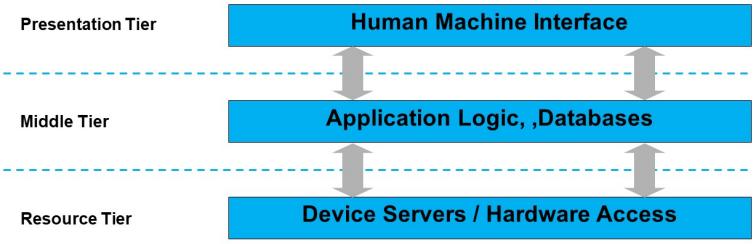

Figure VII.1: Three-tier architecture of the control system.

tier a variety of graphical and non-graphical tools are running on console computers which implement an abstract, aggregated and homogenous view of the HBS and hide unwanted details.

2.1.1 Horizontal Structure

The HBS machine control system functions can be grouped horizontally according to the machine subsysystems:

- **Ion source:** The ion source will be provided by an external partner. If possible, the Ion source control will be integrated into the accelerator control system. Otherwise, a gateway function to the ion source control system will be implemented.

- **Accelerator:** Core function is the RF system responsible for the definition, acceleration and guidance of the proton beam. Equipment to be controlled includes RF cavities or power supplies for magnets, using the beam instrumentation devices like beam position monitors or beam current monitors. Accelerator control can be further subdivided into control of LEBT, RFQ1, MEBT1, RFQ2, MEBT2, DTL and HEBT.

- **Beam dump:** The control system is responsible for monitoring beam dump parameters like temperatures, radiation levels or beam current. Violations of configurable thresholds will lead to interlocks in the machine protection system and in the personnel protection system.

- **Target stations:** Target station control can be further subdivided into target operation (monitoring, cooling), target exchange and cold moderator control. Main control functions are temperature control, vacuum control, cooling, gas management, personnel safety and target handling. Equipment to be monitored and controlled includes motors, pumps, valves, leak detectors, pressure gauges and temperature sensors.

- **Vacuum system:** There will be a common vacuum system for the ion source, the accelerator, the target and the neutron guides. In the vacuum subsystem different types of pumps in differential pumping systems, valves and pressure gauges have to be controlled and monitored.

- **Conventional facilities:** This subsystem is responsible for the control of pressed air, water and electrical power supply, including the control of compressors, pumps and valves as well as the continuous monitoring of process values like air pressure, air flow, water pressure, water flow, water temperature and electrical power, voltage, current, cos phi of all main circuits. It is expected that the conventional facilities will be delivered by commercial companies together with their corresponding control functions. In this case, gateways to the integrated HBS control system have to be implemented.

VII.2.2 Functional structure

Orthogonally to this horizontal structure, the HBS control system is structured into the following functional groups which are related to all subsystems:

- **HMI:** On operator consoles and wall displays in the control room GUIs will be implemented that allow control, optimization and state supervision of the HBS machine. This includes presentation of real-time summaries of all relevant machine parameters. For standard operation, easy startup, shutdown and auto-tuning buttons will be offered. The role-based access allows the presentation of different granularity levels to individual user groups. Homogeneous appearance and a good ergonomic behavior are key design goals for all GUIs.

- **Alarm/Logging System:** The alarm and logging system is responsible for the collection, distribution and archiving of alarms (information on abnormal situations) and logging events (diagnostic information). At the presentation tier, a GUI-based console application allows the definition of alarms and logging events, presents these to the operator and supports the retrieval of archived alarms and logging events.

- **Process Archive:** During the operation the HBS machine all relevant process data have to be collected and archived for later analysis. A a graphical tool allows selection of process data for archiving, definition of archiving intervals and persistence times in the archive. A data browser serves as a graphical front-end later retrieval and presentation in configurable graphs, e.g. as time series.

- **Electronic Logbook:** The electronic logbook is a software tool that is used for the communication between the accelerator personnel. It allows adding observations and comments during accelerator operation and combine these with accelerator state information and measurement data. It is integrated into the control system and typically has a client server architecture using a database.

- **Timing system:** Due to the pulse structure of the proton beam, neutron instruments and HBS machine components have to be synchronized. This can be achieved with a central clock that is distributed via a dedicated timing network together with event, trigger and state information. Timing receivers have to be implemented at individual devices that decode timing and event/trigger/state data and generate pulses and clocks for the synchronization of the device hardware.

- **LLRF (Low Level Radio Frequency) system:** Central functionality of the LLRF system is the control and stabilization of the RF field of the cavities by implementing complex filters and feedback loops. Additionally, the LLRF is responsible for the cavity tuning via stepper motors. The design of the LLRF will be based on the MicroTCA.4 platform, since this is a well-established standard in many recent accelerator projects and because commercial boards are available on the market, e.g. from SIS. A more detailed discussion of the LLRF system functionality and implementation can be found in section IV.2.

- **Beam diagnostics:** During accelerator operation beam parameters have to be monitored. This is accomplished with a variety of diagnostic devices like beam position monitors, beam current monitors or beam loss monitors. Selection of diagnostic devices should consider the availability of commercial readout electronics. The control system will provide access to the beam parameters by interfacing the readout electronics.

- **Machine protection system (MPS):** The Machine Protection System has to avoid machine damage or unwanted radiation due to device failures or abnormal events like beam loss, failure of a cooling system or failure of the vacuum system. It will be designed as a failsafe system shutting down targets stations, accelerator or ion source in the case of a fault. It will have a distributed architecture consisting of input devices, output devices and a beam interlock system, connected by a dedicated optical MPS network. The beam interlock system will be based on FPGA technology to ensure fast reaction times. Due to the independent operation of the target stations in in the states IDLE, COMMISSONING and BEAM-ON, shutdown interlocks as well as the HBS components affected by a shutdown must be dynamically changed according to the state of the targets.

- **Personal protection System (PPS):** The personal protection system has to ensure the protection of humans against any hazards from the machine, which may lead to injuries. Main focus is the exposure to radiation, but also other hazards like electrical shock have to be prevented. The personal protection system will be implemented as a highly reliable failsafe system that ensures a safety level according to ISO 13849 PL e (roughly corresponding to IEC 61508 SIL 3). With regard to radiation safety it will manage entrance and exit from radiation controlled areas. Additionally, radiation levels will be monitored. Any access violation or any violation of radiation level thresholds will lead to immediate shutdown of ion source and accelerator.

- **Operational Security:** Since remote network access to the HBS machine control system shall be allowed, appropriate cyber security mechanisms have to be implemented. One of the mechanisms is the strict separation between the technical network with the control devices from the standard office network. In order to reduce operational faults, a role-based access to the control systems has to be implemented that gives different levels of control to specific user groups.

- **Automation and State Transitions:** The control system will provide a scripting interface that allows the definition of high-level procedures for automatic execution of complex sequences of tasks. One dedicated high-level procedure will be a Master Control Task, that will execute state transitions of the accelerator. At least the following states will be defined:

  - Normal Operation (Beam On)
  - Commissioning
  - Maintenance
  - Idle
  - Fault

  The control system will provide mechanisms to record and play back control system configurations and operational sequences.

VII.3 Selection of Technologies

VII.3.1 Software framework for the control system core

Since many decades, Forschungszentrum Jülich has the proven competence to build and maintain complex particle accelerator systems, e.g. the synchrotron COSY. As a consequence, all competences to implement the HBS control system from the scratch are available in Jülich. In order to reduce the implementation effort, it is intended to base the implementation on a control system software tool that is well established in the research community. Today, the most promising and most commonly used candidates are EPICS and TANGO [Mü15]. JCNS has a long-term experience in TANGO since all JCNS instrument control systems at the FRM II have been implemented with TANGO. Because the control systems of all JCNS instruments planned for the ESS have to be based on EPICS, JCNS has started to build up an EPICS competence. Additionally, EPICS competence is existing at IKP, since it is already used at COSY. Since EPICS is the most widely spread in the accelerator community and since it is used at most potential partner facilities like MYRRHA, ESS, ISIS or PSI, it has been decided to use EPICS as the software framework for the accelerator control system core.

Originally EPICS has been developed in a cooperation of LANL and ANL. It is open source and supported by a large community. From the architecture point of view, EPICS is designed as a distributed client server system where so called IOCs (Input Output controllers) exchange process data in form of process variables (PVs) with client computer systems via the Channel Access protocol, as shown in Fig. VII.2. The Channel Access Protocol is based on Ethernet and UDP or TCP. EPCICS V7 introduced a new protocol called PVaccess that allows the access to structured and distributed data. Central functionalities of EPICS are location independence and device abstraction using device server software on IOCs which provide a common interface independent of a specific hardware device.

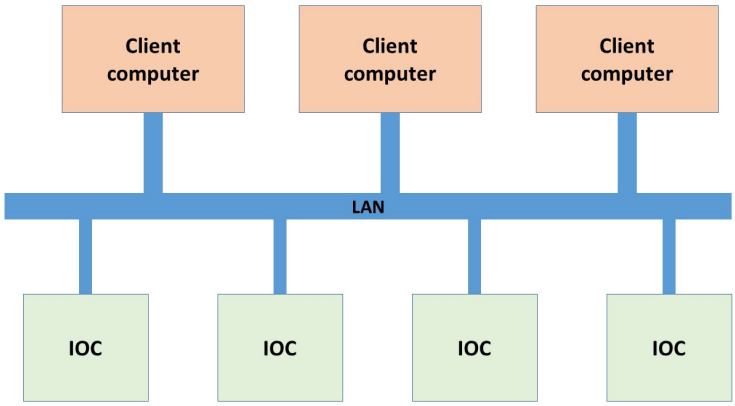

Figure VII.2: *EPICS distributed Client/Server Architecture.*

The IOCs are computer systems to which all front-end electronics are connected. Historically, IOCs were implemented as VME systems with the commercial real time operating system VxWorks. Today it is possible to use PCs with Linux or the free real time system RTEMS as IOCs. IOCs in the HBS accelerator control system shall be based on industrial PCs with Linux, normally. RTEMS shall only be used when real time operation is required.

VII.3.2 Software framework for HMIs

Historically, a variety of different HMI tools and applications have been developed in the EPICS context. Today, most recent EPICS projects use Control System Studio (CSS) as a software framework for HMIs. Originally started around 2006 as a joint effort of DESY and SNS, CSS now is open source software which is used by a broad community (APS, BNL, ITER, DIAMOND, ESS,...). It is a very large system consisting of about 2 Million lines of Java source code. Due to the common use and the extensive functionality of CSS, it has been decided that it shall be used as HMI software framework for the HBS accelerator control system.

CSS consists of a synoptic editor for development of new HMI tools and a collection of ready-to-use tools which cover most HMI requirements of an accelerator control system, like alarm system, process archiving system or electronic logbook. It is based on Eclipse RCP and a version independent of Eclipse, called Phoebus, is available, too. CSS supports Oracle, MySQL or PostgreSQL as relational databases for the storage of PVs, alarms or log messages and it has not yet been decided which of these databases will be used for the HBS accelerator control system.

CSS is a highly modular system based on plugins. It can easily be extended by new software components and existing software components can easily be exchanged by new ones, simply by providing a wrapper around the new software component that conforms to the plug-in interface. The consistent design of CSS provides a homogeneous and ergonomic interface to the user. E.g. it is easy to select a PV in the context menu of one CSS tool and send it to another CSS tool.

VII.3.3 Computer and network technologies

Server computers as well as front end computer systems will be based on the PC technology using Linux as operating system. Front end computer systems – e.g. IOCs - will be industrial PCs. The formfactor will depend on the requirements. E.g. for the LLRF system MicroTCA systems will be used, which is heavily deployed at many recent accelerator control systems, like XFEL or ESS. In other scenarios PXIe or CompactPCI Serial seem to be good choices. Also, virtualization is an option for IOCs, when front-end equipment is connected via TCP/IP or UDP.

There will be dedicated communication systems for the timing system and for the machine protection systems. For PLC type of equipment fieldbus systems like Profinet or IO-Link will be used. Otherwise communication will be based on Ethernet, using TCP/IP or UDP.

VII.3.4 PLC technologies

The front-ends of the cooling subsystems, of the conventional facility subsystem and of the vacuum subsystem will follow a distributed architecture implemented with industrial grade PLCs and decentral periphery systems connected via field bus systems. Due to the long-term experience of JCNS and the market dominance, it is intended to use Siemens S7-1500 as PLC systems, ET200SP and ET200MP as decentral periphery systems and PROFINET, PROFIBUS, AS-i and IO-Link as fieldbus systems. At the HBS control systems resource tier, industrial PCs are used that are connected via PROFINET to these front-ends. The implementation of the personal protection system will be based on the Siemens distributed safety concept with failsafe S7-1500F CPUs, failsafe F-Modules and PROFIsafe communication, which allows to achieve PL e according to ISO 13849.

VII.4 Implementation approach for functional groups

VII.4.1 Human Machine Interface (HMI)

HMI encompasses a wide range of tools and screens intended for a variety of functions, user groups and scenarios. Scenarios include

- the central control room, from which the HBS is operated,
- displays distributed over the facility, e.g. giving machine state information like beam energy and beam current,
- remote access.

The central control room will contain large overview displays illustrating the state of all subsystems in graphical representations of the HBS. Dedicated operator consoles and engineering screens allow the operation, maintenance and optimization of the HBS for operators, engineers and scientists. The central control room should be designed in a way that provides ergonomic work space for these different user groups. Fig. VII.3 shows the central control room of SLAC as a typical example, how the HBS control room could be designed.

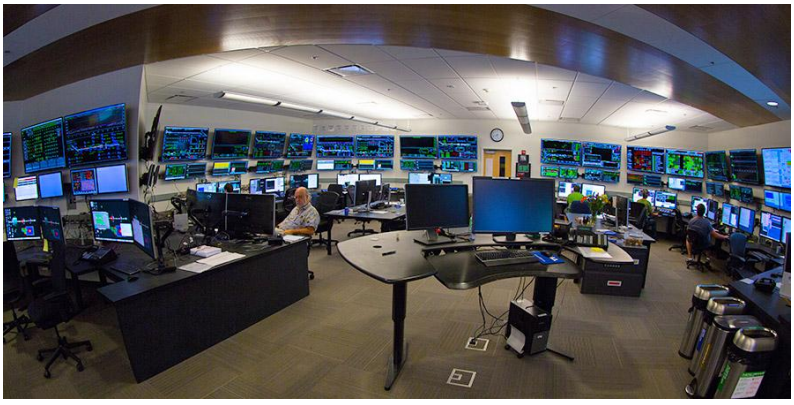

Figure VII.3: *Control room of SLAC as an example for the HBS central control room [Dir23].*

Complementary to the central control room there must be a main server room, containing the server and database computers required by the control system. For redundancy reasons there should be a secondary server room, running backup copies of important systems in the main server room. In the following sections the most important HMI functions and their implementation are covered.

4.1.1 Synoptic Editor

The synoptic editor is a graphical editor that is used to build operator interfaces (OPIs), typically showing animated illustrations of the accelerator or its subsystems. In the synoptic editor, graphical objects and widgets can be used to draw pictures. Attributes of these elements – like color, size, position or text – can be connected directly to PVs of the control systems or to scripts. Ideally, the designer of an OPI does not have to care on which device the OPI will run. Possible devices include Windows based PCs, Linux-based workstations, panels displayed by web browsers or mobile phones.

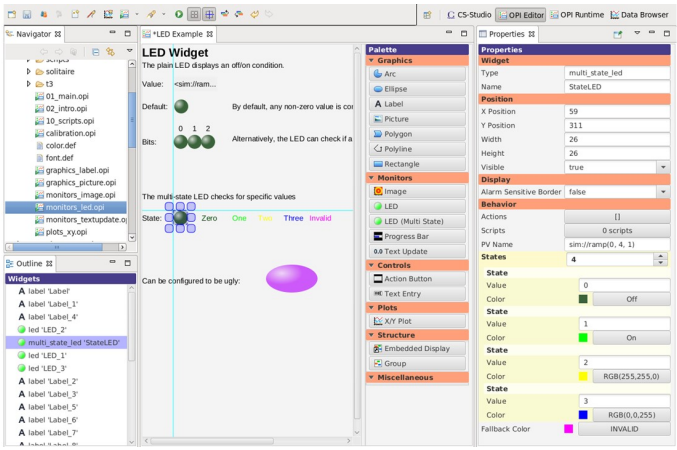

Figure VII.4: Display Builder OPI editor screenshot [KGC16]

Since Control System Studio already comes with a ready-to-use synoptic editor that fulfills all HBS requirements, this will be used for the HBS control system. Due to performance issues, the original OPI builder of CSS, called BOY (Best OPI, yet), has recently been replaced by the so-called Display Builder, which is downward compatible to BOY. The Display Builder consists of a synoptic editor as well as a runtime environment for OPIs. The Display Builder creates *.bob files, which are loaded and interpreted in the runtime environment. Fig. VII.4 shows a typical screenshot of the Display Builder OPI editor, illustrating how OPIs can be drawn with graphical objects and how their attributes can be connected to scripts or PVs. Graphical objects and widgets include arcs, polylines, images, LEDs, action buttons, progress bars, x/y-charts, text entries, text displays and many more.

4.1.2 Alarm and Logging Systems

CSS has built-in powerful alarm and logging systems, which comprise a variety of GUI based tools for the configuration, display and handling (acknowledgement, disabling, ...) of alarms and log messages as well as a runtime environment responsible for the storage of alarms, log messages or alarm configurations and the automatic reaction to alarms. Alarms, log messages and alarm configurations are stored in a relational data base.

It has been decided to use the CSS alarm and logging systems for the HBS accelerator control system, since both fulfill all requirements. The CSS alarm system is called BEAST (Best Ever Alarm System Tool). BEAST comes with a variety of tools for displaying alarms or configuring alarms, e.g. tabular alarm viewer shown in Fig. VII.5 as well as a tree alarm viewer. The CSS logging system comes with a generic history viewer can be used to display, sort or group log messages.

As shown in Fig. VII.6, an Alarm Server resides in middle tier of the control system that uses the alarm configuration in the relational database (RDB) to read the appropriate PVs from the IOCs and evaluates alarm conditions. As soon as alarms are detected, a log message is forwarded to the log message RDB, the alarm state is stored in the alarm state RDB and forwarded to the alarm client GUI. Optionally, speech annunciations will be executed. Any user activity like alarm acknowledgment or alarm configuration change is forwarded to the alarm server and stored in the alarm config or state RDBs. The Apache ActiveMQ implementation of the Java Message Server (JMS) is used for the communication between the individual software components. In an analogous way, the configuration of the logging system as well as log messages are stored in RDBs.

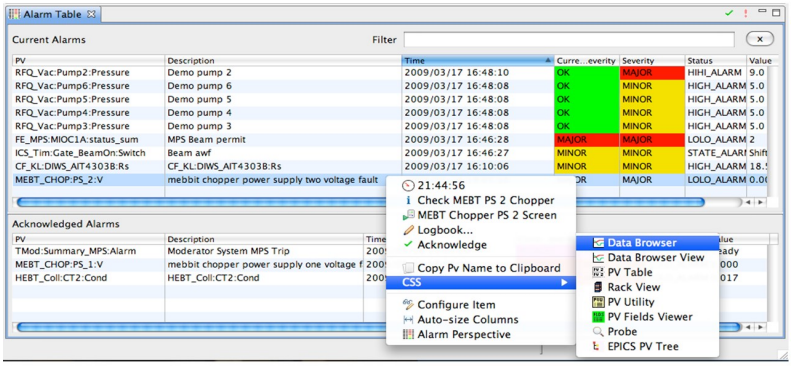

Figure VII.5: BEAST Alarm Table screenshot [Kas11b].

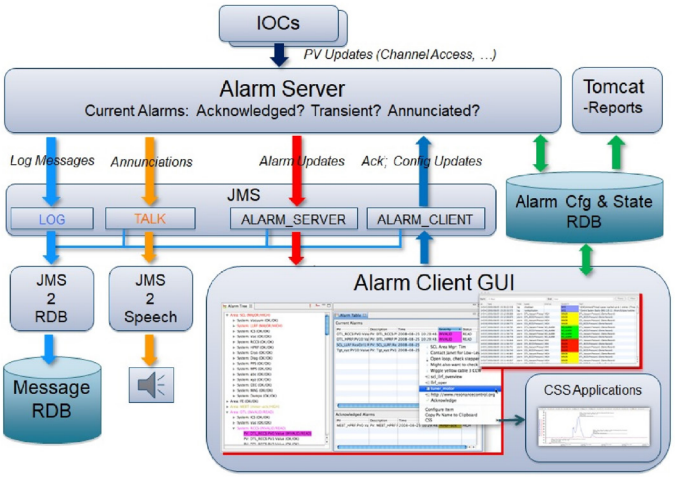

Figure VII.6: BEAST components and their interaction [Kas11a].

4.1.3 Process data archive

CSS provides an integrated environment for the archiving of process data, called BEAUTY (Best Ever Archiving Utility, Yet), which will be used by the HBS accelerator control system, too. Any CSS application can access archived data. Additionally, BEAUTY provides tools for the configuration of the process data archive (selection of PVs, sampling frequency,...) and a generic tool for the display of archived data, called Data Browser. The Data Browser allows the selection of PVs from the archive and offers a variety of options for plotting these data, as shown in Fig. VII.7.

As shown in Fig. VII.8, an Alarm Server resides in middle tier of the control system that continuously reads samples of configured PVs from the IOCs and stores these in the archive sample RDB. The Alarm Server operation is based on the configuration in the archive configuration RDB.

It is known that BEAST has performance issues, when the number of PVs is considerably higher than

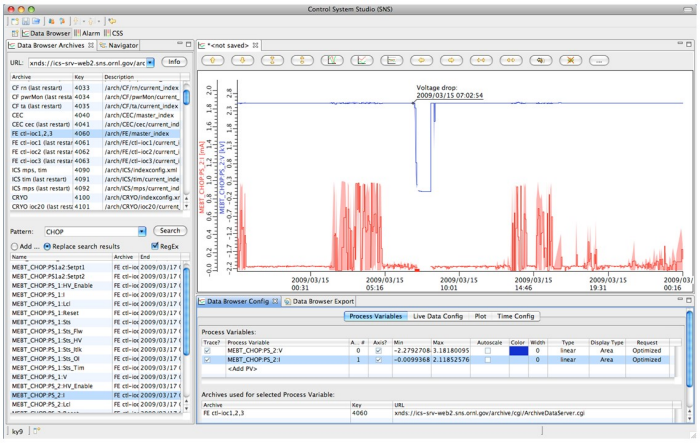

Figure VII.7: CSS Data Browser screenshot [Kas11b].

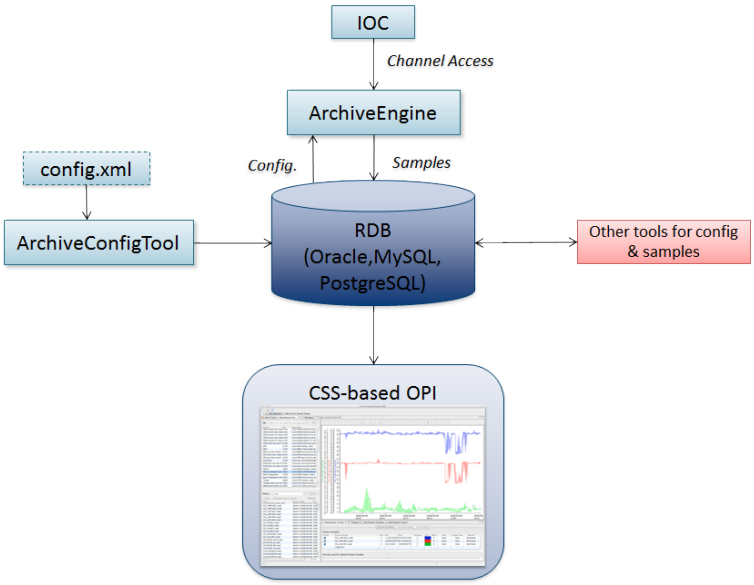

Figure VII.8: BEAUTY components and their interaction [KG18].

0.5 Million. It is not expected that this will be a problem, since the number of PVs in the HBS control system should be lower. Otherwise, EPICS Archiver Appliance could be used, which can handle several Million PVs.

4.1.4 Electronic Logbook

Due to the modular plug-in architecture of CSS, any logbook can easily be integrated into CSS. Since CSS already supports several electronic logbooks, it is recommended that the HBS accelerator control

system uses one of these. CSS provides high degree of integration between the CSS tools and the selected electronic logbook. For example, it is possible to select a PV, diagram or a screenshot from a CSS application and forward it to the electronic logbook, as illustrated in Fig. VII.9.

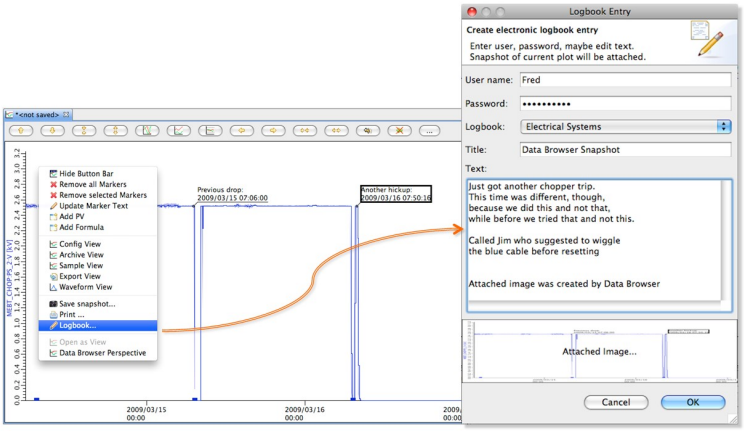

Figure VII.9: *Interaction between CSS applications and the CSS logbook [Kas11b].*

VII.4.2 Timing System

Besides the distribution of synchronous clocks with a jitter in the order of picoseconds, the timing system is responsible for the time stamping of events and the distribution of sequences of precise triggers. Synchronous clocks can be used to generate local clocks for DACs or sampling ADCs connected to diagnostic devices. Triggers will enable the synchronized operation of client devices, like chopper magnets, kicker magnets or cavity LLRF systems. Triggers can be used also as post mortem triggers to freeze post mortem buffers of high speed DAQ devices. Timing stamping provides a machine-wide time information for acquired data and important events.

As shown in Fig. VII.10, the timing system has a hierarchical architecture. A timing generator is responsible for the clock distribution and for the generation of timing event and trigger sequences. Timing clients that want to use services of the timing system have to be interfaced by timing receivers. The communication between timing receivers and the timing generator is accomplished by a dedicated timing network, that connects both via point-to-point communication links. Due to the limited fan-out of the timing generator, there will be switches/fan-outs between the timing generator and the timing receivers. The timing system defines a digital protocol on the timing network links. The timing generator encodes clocks and triggers according to this protocol and the timing receivers decode this information and provide it to the timing clients.

The reference clock for the timing generator will be provided by a very stable RF master oszillator with a jitter in the order of femtoseconds. RF client devices which special requirements to clock stability will directly be connected to the RF master oscillator.

For neutron detectors a timing resolution below 100 ns is sufficient, but for internal operation of the ion source and accelerator components like cavities, RFQs, kicker magnets or chopper magnets, a resolution in the order of nanoseconds and a jitter in the order of picoseconds is envisaged. An interesting candidate for the timing system is White Rabbit developed by CERN as an improvement of the Precision Time Protocol (PTP) according to IEEE 1588, achieving sub-nanosecond accuracy. Unfortunately, White Rabbit only defines clock synchronization and the timing network. Higher level

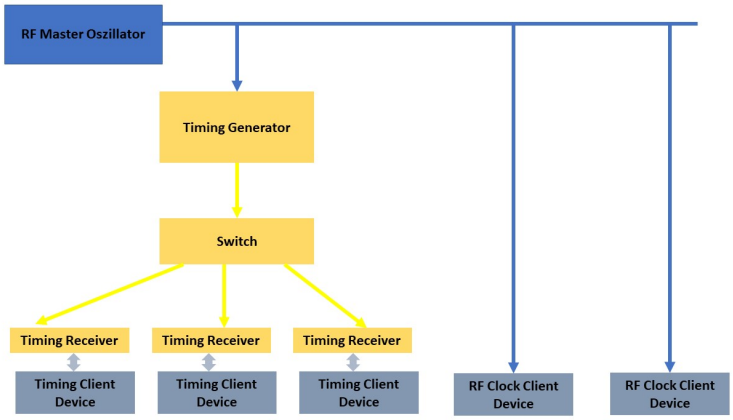

Figure VII.10: *Timing System Architecture.*

services like trigger distribution have to be defined and implemented specifically for each facility. The commercial support for White Rabbit is limited, too. Therefore, it has been decided to use the timing system available from the Finnish company Micro-Research Finland (MRF) for the HBS accelerator control system, also because MRF is widely used in the accelerator community and employed by the potential HBS cooperation partners ESS and PSI, too.

The MRF timing system is based on communication over optical links with 8B10B coding and automatic delay compensation. The event clock rate is between 50 MHz and 125 MHz, leading to a resolution of up to 8 ns. For the SwissFEL the resolution has been improved to 7 ns (142,9 MHz) and there is still room for further improvement. Outputs signals can be shifted in 50ps steps.

The MRF timing system defines an event/trigger distribution protocol and the timing system generator is equipped with a programmable sequencer for triggers and events. Free FPGA code implementing the event receiver is available, e.g. for the integration into detector electronics.

A wide range of timing generator, switch/fan-out and timing receiver modules for different form-factors - including MicroTCA.4, VME, CompactPCI, PMC and PCIe – are commercially available from MRF and well-supported by EPICS. For the HBS accelerator control system MicroTCA.4 is the preferred choice, which allow the easy integration into the LLRF electronics that is based on MicroTCA.4, too. Specifically, the module mTCA-EVM-300 shall be used as timing generator and the module mTCA-EVR-300U shall be used as timing receiver. The module mTCA-EVM-300 can also be used as a 1-to-8 fan-out. The event receiver mTCA-EVR-300U will be equipped with IO-mezzanines for different signal types like TTL, NIM, LVTTL or PECL. The IO-capabilities of the timing receiver can be further extended with the rear transition module mTCA-EVRTM-300. All three modules are shown in Fig. VII.11. Fig. VII.11 also shows the IO mezzanines for NIM and TTL.

In a typical configuration, mTCA-EVM-300 or mTCA-EVR-300U will reside in MicroTCA cates together with a CPU and other application-specific electronic modules. The CPU will serve as an EPICS IOC, which can access both timing modules via PCIe over the backplane of the MicroTCA crate. The software integration into EPCIS is accomplished via Linux device drivers and EPICS drivers, which are available for both timing modules.

MRF does not provide a RF master oscillator. This can be acquired either commercially or from a partner facility. Key requirements are low jitter, long term stability and flexible frequency selection. A possible choice for a commercial product is the Reference Master Oscillator, available from the Slovenian company Instrumentation Technologies D.O.O.

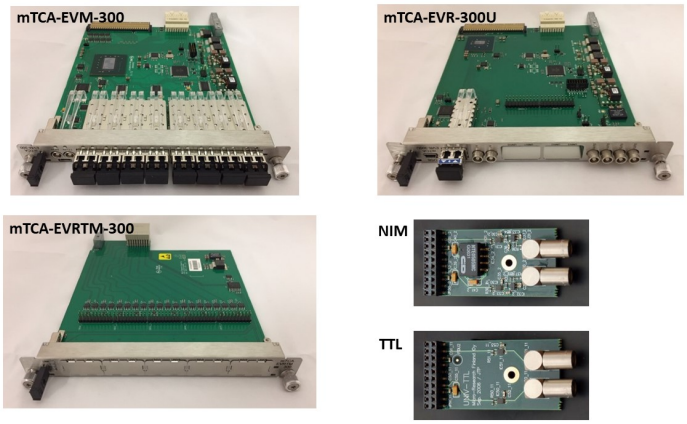

Figure VII.11: MRF timing system modules that will be used for the HBS accelerator control system. ©Micro-Research Finland Oy.

VII.4.3 Beam Diagnostics

The accelerator will be instrumented with a variety of different types of beam diagnostics devices, including beam position monitors, beam profile monitors, beam loss monitors, beam current monitors or secondary emission monitors. Some of these devices directly interact with the PPS or the MPS to accomplish a fast reaction in the case of faults. All beam diagnostic devices have to be read out by the control system in order detect alarm conditions and retrieve diagnostic information. Since it is expected that beam diagnostics are either commercially available or can be acquired from partner labs, the corresponding readout electronics are expected to provide some sort of EPICS support. Good EPICS support should be a selection criterion for beam diagnostic device.

The Libera system, which is commercially available from the Slovenian company Instrumentation Technologies D.O.O., is a possible choice for the readout electronics, since it fits to a wide range of beam diagnostic devices and provides a good EPICS support.

VII.4.4 Personnel Protection System (PPS)

Since the PPS has to prevent any harm to human beings, it has to work autonomously, independent of the HBS accelerator control system. It directly interfaces beam diagnostics in order to detect presence of the beam, electromagnetic radiation or radioactivity and it directly interfaces the machine interlock to switch off the beam reliably. Additional equipment connected to the PPS system includes oxygen monitors, monitors for poisonous gas, emergency buttons, personal key boxes, flash lights, door control boxes and many other safety-related devices. The PPS provides an interface to the control system to enable the monitoring of the PPS state and the detection of alarm conditions. Also, the MPS will be connected to the PPS in order to be informed about abnormal conditions.

An extensive risk and hazard analysis will lead to the definition of the PPS safety functions, from which the technical design will be derived. The implementation of the PPS will be completely based on the Siemens S7-1500 PLC family and ET200SP, ET200pro or ET200eco decentral periphery systems shown in Fig. VII.12, using mainly Profinet for device communication. Siemens HMI panels will be used for local operation and system state information. With these systems it is possible to achieve the intended safety level according to ISO 13849 PL "e".

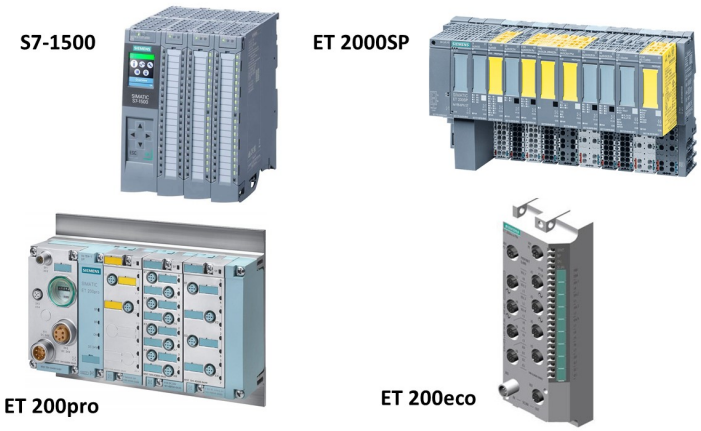

Figure VII.12: S7-1500, ET200SP, ET200pro and ET200eco devices. ©Siemens AG.

VII.4.5 Machine Protection System (MPS)

Due to the high investments into the accelerator the MPS has to be designed as a redundant fail-save system that is able to operate autonomously independently of other subsystems to ensure that the accelerator is switched off reliably and fast in the case of a fault. It should be flexible enough to support independent operation of target stations as well as commissioning activities. The analysis of the origin of shutdowns should be supported by the collection of post-mortem logs.

Analogous to [Peg18], the MPS consists of the following components, shown in Fig. VII.13:

- **MPS Input Devices (MID):** Devices that provide information about beam and accelerator status requiring a fast shutdown, e.g. diagnostic devices like BPMs or BLMs.
- **MPS Output Devices (MDO):** Devices that can quickly shutdown the beam, e.g. the ion source, chopper magnets or kicker magnet before the beam dump.
- **Beam Interlock Systems (BIS):** Hardware system responsible for the fast shutdown decision, typically distributed. This includes the communication system connecting MIDs and MODs.
- **Beam Permit System (BPS):** Subsystem that does consistency check of the machine state before beam is allowed to be enabled.

Besides the MIDs, indicating the need for a fast accelerator shutdown, the MPS is connected to the control system, which sends fault information of slow subsystems, like the PPS or the vacuum system, to the MPS. The MPS System can be configured by the control system and makes state information and post-mortem logs available to the control system for beam permit or for further analysis.

The pulse structure of the HBS requires a fast reaction time of the MPS below 1ms. As a consequence, it cannot be implemented with PLC technology like the PPS. Instead, it will be a dedicated hardware system that is based on FPGA technology. Since the MPS has to be designed as a distributed system, there will be a dedicated MPS communication system.

Fig. VII.14 shows a possible implementation approach for the fast beam interlock systems, suggested in [Roj20]. The BIS consists of a master device and concentrator devices connected via a network of redundant optical links. The concentrator devices interface the MID and MOD devices to send

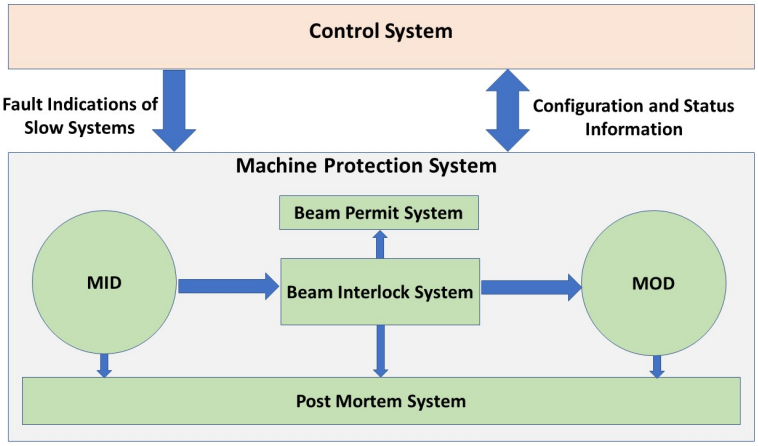

Figure VII.13: MPS components.

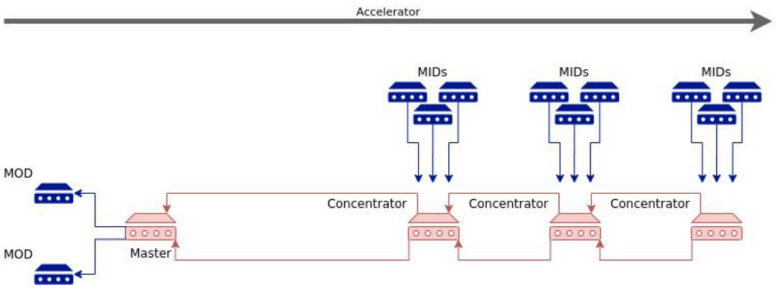

Figure VII.14: Architecture of the fast beam interlock system [Roj20].

status information to the master device and receive interlock commands from the master device. The master device is responsible for the interlock decision. The design of the master device as well as the communication with concentrator devices must guarantee failsafe operation of the BIS. Both master device and concentrator devices will be FPGA-based hardware modules, which rely on configurable tables for interlocks and communication. By masking of table entries, it is possible to suppress interlocks in the master or the transmission of data in the concentrators.

Implementation of the MPS requires extensive hardware and software development work and commercial systems are not available on the market. Therefore, it is intended to start a cooperation with a partner facility with the intention to reuse as much as possible of its existing MPS developments. A potential risk of this approach is the high innovation rate of FPGA technology leading to problems in reusing existing solutions. Another option for the implementation of the MPS is a cooperation with the Slovenian company Cosylab, d. d., which has proven experience in this field.

VIII.

SAFETY SYSTEMS / RADIATION SAFETY

With the high current proton beam the accelerator components can be activated and the area and devices do need appropriate radiation safety surveillance. For this purpose the accelerator hall and corresponding beam transport tunnels will be equipped with safety interlock switches and buttons for search and secure procedures. Several emergency proton/neutron beam shut-off-switches will be installed to shut down the accelerator in case of an accident. Optical and acoustic warning systems will be placed in the relevant parts of the facility to alert/caution the personnel inside. Locations with radiological hazards will be demarcated from other areas by putting appropriated symbols indicating the radiation level in work areas and precaution to be taken by working personnel. Neutron and gamma dose rate monitoring systems will be placed along the entire proton beam line.

VIII.1 Radiation Safety Requirements

The HBS Facilities must meet the conditions stipulated by the German radiation protection legislation:

- Radiation emerging directly from the facility must not exceed a level of 0.7 to 1 mSv per year (8760 h).
- Radiation exposure by the emission of radionuclides must not exceed a level of 0.3 mSv per year.
- The sum of i. and ii. must be below 1 mSv (§§80, 81 StrlSchG, German radiation protection law).
- The radiation exposure (outside the radiation controlled areas) must not exceed a level of 6 mSv/a (2000 h) on the institute premises and of 1 mSv/a outside the premises.

This means the level of ionizing radiation which can occur within a certain area or laboratory determines the degree of radiation protection measures which have to be foreseen. In the German radiation protection ordinance dose limits are specified which will affect the design of the planned accelerator facility. First, the dose to the public must not exceed 1 mSv per year from which only up to 0.3 mSv may result from the release of air and water containing induced radioactivity. Second, German implementation rules specify that these dose limits have to be fully respected assuming a worst-case scenario leading to a much smaller radiation exposure to the public on the average. Third, so-called radiation protection areas are defined inside the area of the facility. These are the following (in ascending order of the maximum tolerated dose rate):

- "Betriebsgelände" (company premises): up to 1 mSv per year.

- "Überwachungsbereich" (radiation surveyed area): up to 6 mSv per year.
- "Kontrollbereich" (radiation controlled area): up to 20 mSv per year.
- "Sperrbereich" (prohibited or inaccessible area): larger than 3 mSv per hour.

The radiation protection strategy for the planned facility will follow the existing one at Forschungszentrum Jülich: The accelerator itself and all transfer beam lines to the experimental areas and all experimental areas ("caves") are regarded as prohibited area (Sperrbereich) whenever beam can be transported in these areas. After shutting down the beam these areas can be set to a radiation controlled area (Kontrollbereich). This enables radiation-controlled workers to enter the area. Normal workers or visitors are only allowed to access radiation controlled areas under special conditions The reversal of the state "radiation controlled area" requires the approval of the radiation safety officer responsible for this area, who has to check in advance whether the remnant dose rate and the contamination level in this area permit to change the state of this area. For all other radiation surveyed areas within the premises the dose rate must not exceed 3μSv per hour which is calculated from the yearly dose limit of 6 mSv assuming a working time of 2000 hours per year. If no surveying of the radiation level is foreseen, i.e. no instrumentation is installed to measure the dose rate, the yearly maximum allowed dose is 1 mSv. Again 2000 working hours can be assumed for an average worker. Thus the shielding design has to secure a dose rate of less than 0.5μSv per hour for all areas and accelerator installations, which are within the premises and are freely accessible for workers and visitors.

Following the concept of the worst-case scenario (as described in §§99, 102, 103, German Radiation Protection Ordinance) the time which the reference person may spend at the fence of the premises is assumed to be 8760 hours per year (365 times 24 hours)). Exploiting the maximum allowed dose for the public of 0.3 mSv per year coming from the release of radioactivity with air and water one would have to fulfil a yearly dose limit of 0.7 mSv per year for the prompt radiation. This results in a prompt dose rate limit of approximately 0.08 μSv per hour to the public. Basis of the shielding requirements are the expected beam losses within the different accelerator sections. These Radiation safety aspects have a major impact on civil construction planning for the HBS facility, due to the shielding measures that are to be taken for operating the accelerators and experiments.

VIII.2 The Radiation Shielding Plan for HBS

The radiation shielding plan for HBS is based on detailed Monte Carlo calculations of the production, transport and attenuation of radiation at the various components of the HBS facility. These Monte Carlo techniques, to simulate the generation of radiation and the transport through the shielding are precise and well-suited for complex geometries e.g. in experimental stations. The geometry of the problem and the composition of the material under investigation are transferred into a computer model. Then the interaction of the radiation particles while travelling through the shield is simulated. The histories of all particles transported are evaluated and particle fluences or energy depositions can be scored. For the shielding calculations for HBS the Monte-Carlo code FLUKA (www.fluka.cern) has been chosen for mainly the following reasons:

- All kinds of leptons and hadrons, ions and nuclei can be transported,
- The energy of the particles is hardly restricted (from meV neutrons to TeV ions).
- Variance reduction techniques are already implemented in the code.
- The code has proven to be reliable and compared to experimental data.

- The induction of radioactivity can be calculated.

The shielding of the different experimental areas and the different accelerator structures have been modelled (Fig. VIII.1 and Fig. VIII.2) and verified with FLUKA.

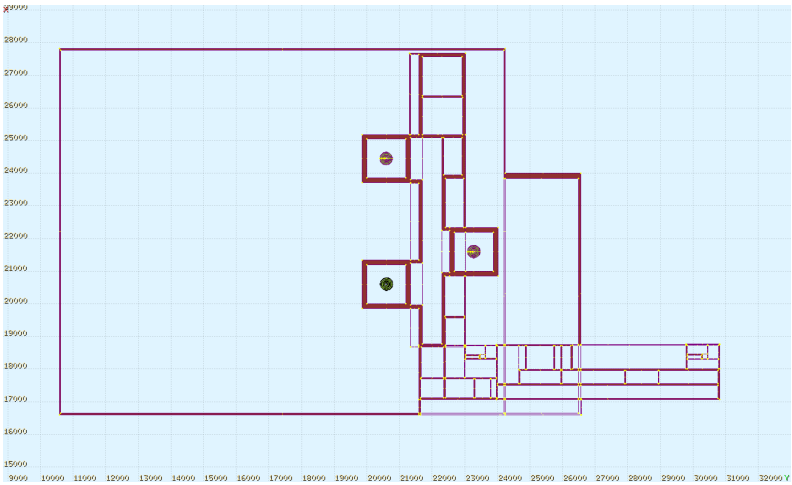

Figure VIII.1: *Setup of the HBS building in FLUKA. Given is the ground floor showing the TMR caves, experimental halls and technical rooms based on the footprint of HBS at the campus of FZJ Jülich (see TDR Vol. 4).*

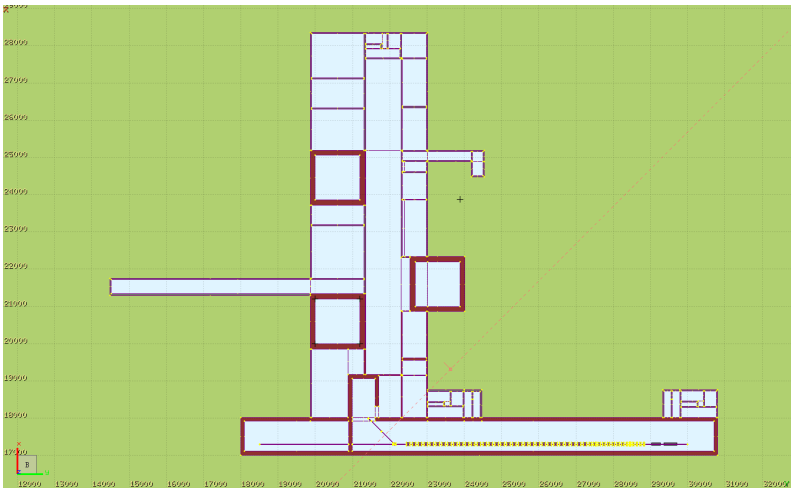

Figure VIII.2: *Setup of the HBS-Building in FLUKA. Given is the first basement level of the accelerator and technical rooms.*

As examples Figures VIII.3,VIII.4 shows the result of a Monte-Carlo dose calculation with FLUKA for the proposed HBS accelerator. In a worst case scenario, the loss of 10^{14} protons per second (3% beam loss) with energy of 70 MeV is simulated and the resulting radiation is transported through the concrete shield of the tunnel and the surrounding soil.

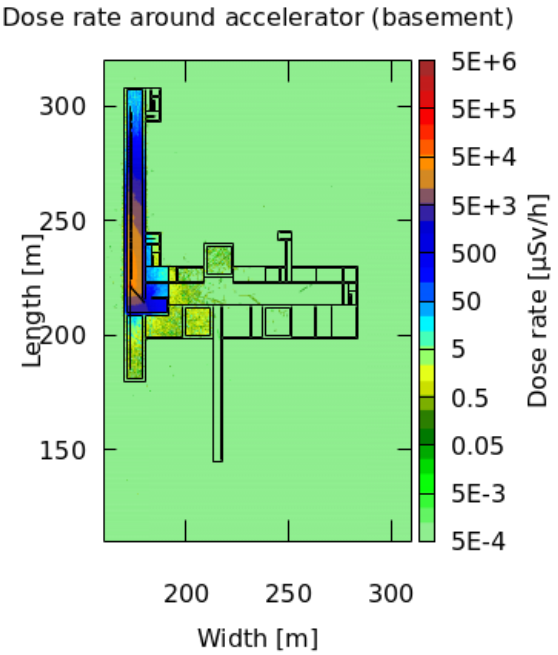

Figure VIII.3: *Dose pattern calculated for the underground HBS accelerator areas. Following conditions have been used: 3%-losses of a 100 mA-proton beam with increasing energy from 2.5 MeV to 70 MeV and a duty factor of 5 along the beam line. The protons are fully stopped in iron targets causing an interacting rate of 100% of the primary beam. The black outline shows the contour of the concrete shielding.*

Another example is the shielding of the TMR areas in which the neutrons are generated. The TMR itself consist of layers of polyethylene and lead of 1.4 m thickness. The TMR is surrounded by a concrete shielding of 1.4 m to decrease the number of neutrons entering the experimental area severely. Fig. VIII.5 shows the shielding design (simplified) and dose rate for the TMR-1 and concrete shield The results shown refer to a proton beam with 70 MeV, an intensity of 10^{16} protons per second, a iron-target causing an interacting rate of 100% of the primary beam in the target. The concrete shielding around the TMR was designed to ensure a neutron reduced experimental area. By this, the radiation level is much lower than 0.5 μSv.

VIII.3 Radiation Protection Concerning the Emission of Radio-Nuclides

The operation of HBS may cause an emission of radio-nuclides into the environment.Two radiological paths are to be considered, the activation of air and of soil (ground water respectively). The activation of air occurs mainly in the target areas of HBS and in the accelerator and transfer-tunnel of HBS. It can effect the emission of radio-nuclides (e.g. 11-C; 32,33-P; 7-Be; 38,39-Cl) which gives source terms for radiation exposure mainly by incorporation (respiration), by gamma submersion and by the deposition of radionuclides in the surrounding farmland and consequently the potential insertion of these in the food chain. Furthermore, the activation of soil and ground water can cause an exposure

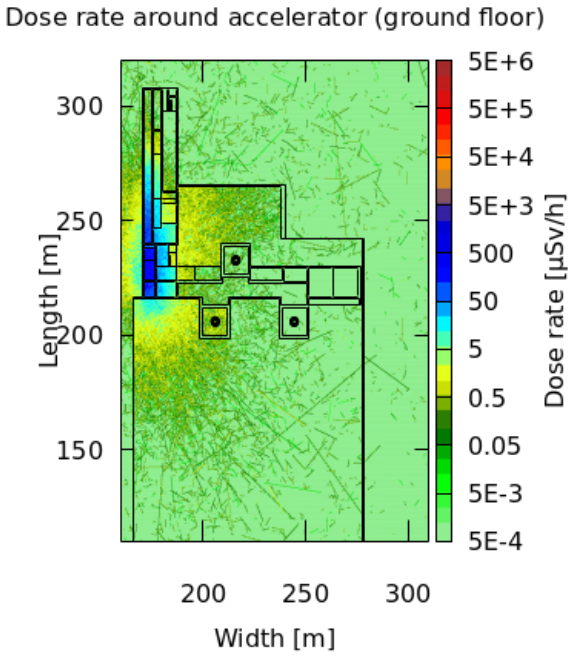

Figure VIII.4: *Dose pattern calculated for the accessible areas like experimental halls, technical rooms e.g. concerning a 3%-loss of a 100 mA-proton beam with along the beam line.*

by ingestion of drinking water (radio-nuclides 3-H; 7-Be; 22-Na; 45-Ca). The radiation exposure by all these radiological paths has to be limited according to §§80, 81 of the radiation protection law (StrlSchG,StrlSchV) to 0.3 mSv effective dose per year. For these model calculations FLUKA is used as well. As a result of these simulations, it was deemed necessary, to install retention systems for the aerosol-borne radioactivity to reduce the emission of the air-borne radioactivity.

VIII.4 Installations for the handling of induced radioactivity

The interaction of medium energetic and high intensive proton beams with matter will produce high levels of activation at several locations of the new accelerator facility. These areas are the following:

- The Neutron production targets
- The HBS accelerator tunnel
- The Transfer tunnel to the production targets
- The safety beam dump with high level of beam interaction

Handling of components and the accessing of these areas requires special care due to the production of radioactive substances. These aspects are described in the following paragraphs.

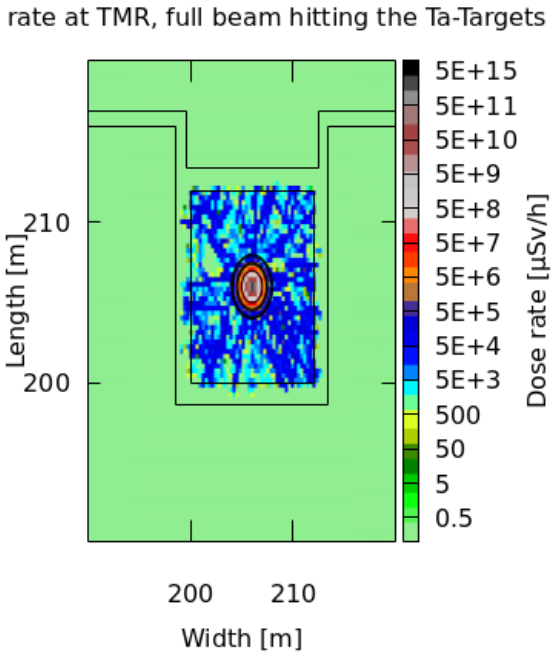

Figure VIII.5: *Dose pattern calculated for the TMR-1 cave under the following conditions: a proton beam enters from below with energy 70 MeV and an intensity of* 10^{16} *protons per second and hits a iron-target causing an interacting rate of 100% of the primary beam. The black outline shows the contour of the concrete shielding.*

VIII.4.1 Activation of accelerator components

A direct consequence of the activation is the occurrence of very high dose rates at the surface of accelerator components. A monitoring system will allow the measuring of the remnant dose rate at the high activation areas after having shut down the beam. This monitoring system will interact with the access control system: If the radiation levels are too high the area will stay in the status "Sperrbereich" preventing persons from entering the area. A set of spares will allow an exchange of components which can not be repaired for radiation safety reasons. A special location for storing activated components shall be foreseen to enable the decay of accumulated radioactivity. For transporting activated components within the premises special containment or sheltering bottles may be needed in order to shield the gamma radiation and to seal radioactive contamination. Installations have to be foreseen for the decommissioning of radioactive accelerator components including the pre-treatment and the long time storage of components which can not be used anymore.

VIII.4.2 Ventilation system for activated air

The air in areas with high levels of beam interaction can get highly activated. Therefore dedicated ventilation systems will have to be installed at these locations. The air flow will have to be independent and hermetically sealed preventing the diffusion of activated air in neighbouring areas. As in these

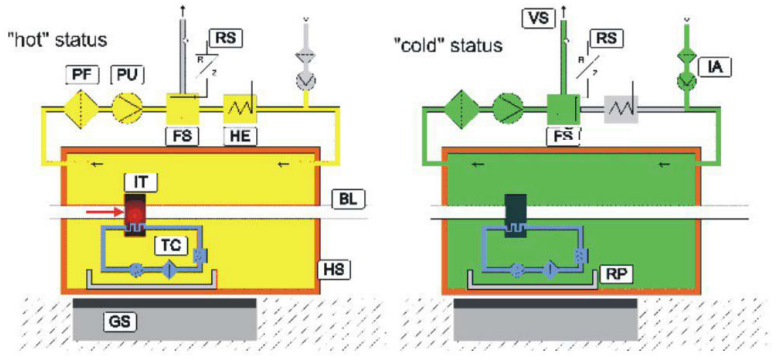

Figure VIII.6: *Schematic diagram of a high activation area at FAIR. Right: Activated air is circulating in a closed ventilation system. Left: The area is flushed with fresh air after shutting down the beam (BL - beam line, FS - flow switch, GS - ground shield, HE - heat exchanger, HS - hermetic sealing, IA - intake of fresh air, IT - interaction target, PF - particle filter, PU - pump, RS - radiation sensor, RP - retention pond, TC - target cooling, VS - vent stack).*

places both high amounts of beam power and of electrical power will be converted into heat, an adequate climate control has to be arranged. A closed system of the primary air flow cooled by a secondary flow of air or water might be advisable. High levels of ionizing radiation are known to cause the dissociation of some molecules of the air leading to the production of toxic and corrosive compounds like for example nitrogen monoxide. Generally air is more or less contaminated by dust and aerosols. These particles will get activated by ionizing radiation and may lead to a higher radiation risk than the gaseous activation products. The air and all installations should be kept as a clean as possible in order to minimize the production of activated dust. Consequently the equipment of working areas where high levels of activation are expected should fulfil both the requirements of a radionuclide laboratory and of a clean room. The block diagram in Figure VIII.6 shows the principle of a ventilation system for a high activation area. The radioactive air (indicated in yellow) is circulating in a closed ventilation system being filtered and cooled along its way. In the lower figure the area is shown in non-active (green) mode. Fresh air is drawn in through a filter (clean room condition) and a non-return valve. The technical construction of the ventilation systems will be addressed by the building services engineering at a later stage of the HBS project.

VIII.4.3 Target cooling systems

Cooling systems may be needed in areas with high levels of beam interaction in order to lead off the high amounts of energy released. Water circulating systems are favoured as water is easily available and has a comparative high heat capacity. The water in these cooling systems will get activated. We foresee a two-stage cooling system consisting of a primary water system working which transfers the heat from the target to a secondary cooling system. Both cooling systems are connected via a heat exchanger allowing the lead off of energy but no transport of radioactivity. The primary cooling should be small but working at a high flow rate in order to restrict the radioactive cooling water to a part of the cooling system which is as small as possible. A collecting system will pick up the radioactive water in case of a leakage of the primary target cooling system. Filters in the primary cooling system will be installed to retain radioactive nuclides.

VIII.4.4 Storage for radioactive residuals

The production of radioactive substances through activation will lead to a high quantity of radioactive. One species of radioactive residuals are the activated accelerator components mentioned already above. These will mainly consist of stainless steel and other metals and non combustible materials. Another source of residuals with probably the highest level of radioactivity will be disused production targets or components from target areas. These residuals will have to be stored for longer periods (several years) to allow the cooling down of radioactivity and the preparation for the decommissioning. Working in areas with high level of activation will demand the wearing of protective clothing. This may be single-serving overalls, shoes, gloves, and others. Large amounts of these residuals per year will have to be collected and treated as radioactive waste, i.e. intermediately stored and packaged for the final decommissioning (combustion). Another possibility would be the usage of multiple-serving protective clothes. Special installations and staff for washing the clothes and monitoring the level of contamination would be required in this case which might cost more time and efforts. Another type of radioactive residuals may come from the ventilation and cooling water systems. Particle filters for the air and ion-exchanging filters for the water will be needed as mentioned above. The induced radioactivity will get accumulated in these filters and they will have to be treated as radioactive residuals.

IX.
INFRASTRUCTURE AND BUILDINGS

IX.1 Infrastructure and support

To operate the linear accelerator and its subsystems an electrical connected load of about 12.5 MW is required. Main technical support to operate the accelerator are the RF and solid state amplifier systems, which have be placed adjacent to the accelerator lattice. Furthermore technical workshops for maintenance will have to be placed here. A dedicated storage area for used magnets, cavities or other possible activated components of the accelerator system will be provided in close proximity. To supervise the operation of the accelerator system as well as the target areas a suitable control room is to be installed.

	Operation 5000 h/y [kW]	24/7 8760 h/y [kW]
Accelerator	12000	100
Beam transport	500	50
Total	12500	150

Table IX.1: Predicted energy assumption of the HBS accelerator.

IX.2 Buildings

The HBS accelerator and proton beam transport systems need a dedicated building structure which can accommodate for the required space and installation of its infrastructure as vacuum supply, cooling systems, air conditioning, maintenance workshops, control systems, IT and storage areas. For radiation safety the whole accelerator and proton beam transport structure will be placed in a two story basement system which will also allow to guide the proton beam from underneath towards the target stations. The accelerator main beam dump, HEBT and beam multiplexer are placed in the basements underneath the experimental halls and target areas. All this leads to a building structure as indicated in Fig. IX.1.

Accelerator tunnel. The accelerator in final stage will be about 100 m long including ion source. It will be paced in a tunnel in the basement shielded by 1 m thick concrete walls and ceiling. The width of the tunnel will be 7 m and the height 6 m underground allowing an overhead crane installation along the whole accelerator structure. Floor load in this tunnel will be 5t/m^2. The accelerator tunnel

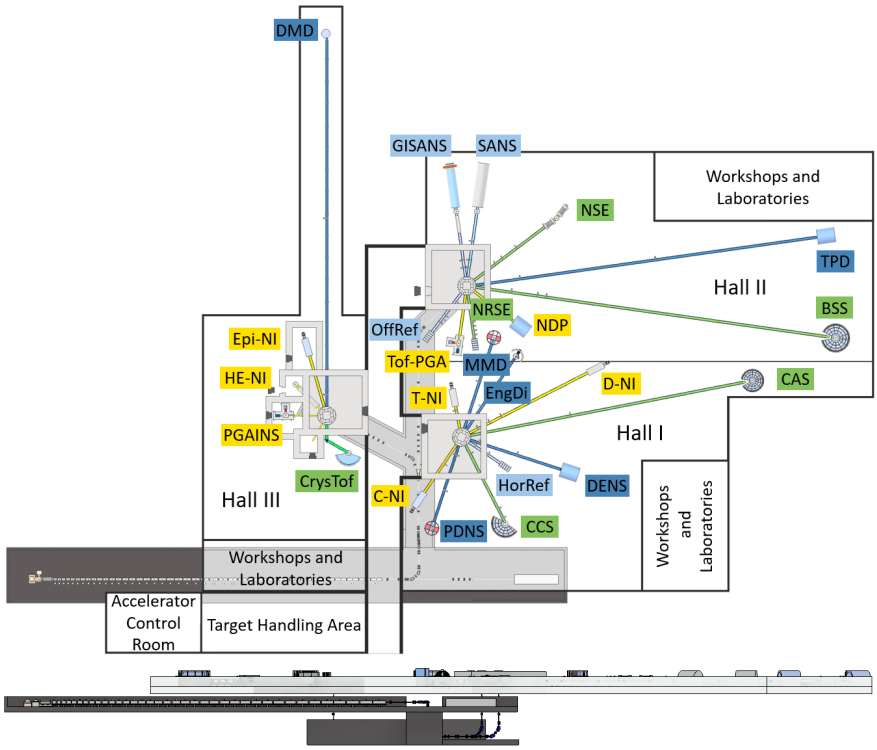

Figure IX.1: *Top view and side view of the HBS facility with the accelerator and the HEBT lines below the ground floor of the facility. The following instruments are indicated: SANS, SANS with GISANS option (GISANS), Offspecular Reflectometer (OffRef), NSE, NSRE, Backscattering Spectrometer (BSS), Tof-PGNAA (T-PGA), Neutron Depth Profiling (NDP), Horizontal Reflectometer (HorRef), Engineerting Diffractometer (EngDi), Diffuse Elastic Neutron Scattering (DENS), Polarized Diffuse Neutron Scattering (PDNS), Single Crystall Diffractometer (MMD), Cold Chopper Spectrometer (CCS), Indirect Geometry Spectrometer (CAS), Cold Neutron Imaging (C-NI), Thermal Neutron Imaging (T-NI), Diffractive Neutron Imaging (D-NI), Disordered Material Diffractometer (DMD), PGAINS, Epithermal Neutron Imaging (Epi-NI), High Energy Neutron Imaging (HE-NI), CRYSTOF.*

is enlarged for hosting the beam dump and corresponding drift line. A central loading space at the end of the accelerator structure is placed for access with all devices to install or de-install accelerator components. At the end, the middle and the start of the accelerator tunnel access via stair cases into the controlled area are foreseen for maintenance work access. The whole accelerator area will be radiation safety controlled area with restricted access. A dedicated storage area for used magnets, cavities or other possible activated components of the accelerator system will be provided in close proximity.

Amplifier gallery. On top of the accelerator tunnel at ground floor the amplifier and electric power support systems are placed in an infrastructure building. The area has the same footprint as the accelerator tunnel but standard wall and ceiling structure as this area will be outside the radiation controlled area allowing access for construction and maintenance.

Accelerator control room. Attached to the amplifier gallery the accelerator control room is placed with up to 10 work spaces.

HEBT tunnel. From the accelerator tunnel the proton beam is bent by 90 deg. aside and another 45 deg downwards to reach a lower second basement level of -12 m beneath ground. Here space for the HEBT beam transport system and the multiplexer is given. This structure will have concrete walls and ceiling of 1 m thickness and a floor load of 5t/m^2. Normal width of this tunnel will be 7 m enlarged for extension to guide the beam towards the individual target stations. The structure will be connected with the central loading space for the accelerator. Access via stair cases into the controlled area of the HEBT tunnel system are foreseen for maintenance work access at the beginning and the end of the system.

Workshops. Technical workshops for maintenance of accelerator components, electronics and testing of software are placed here aside of the accelerator control room.

Infrastructure support area. In the basement above the HEBT tunnel and beneath the target handling area the infrastructure systems for the operation of accelerator and beam transfer components as air conditioning, vacuum systems, electrical power systems, water supply systems etc. will be placed. Network infrastructure, backup servers and further IT systems will be located in close vicinity.

Offices. Office space for the operators and maintenance engineers and technicians as well as radiation safety personal will be provided in the central office building attached to the facility.

IX.3 Costing and timeline

Investment on installations and building costs are estimated according to the individual space requirements on the basis of 2021 cost references. An area of 2720 m^2 is foreseen at three levels with estimated costs of installations of 115.0 Mio EUR (Table IX.2). The costs for the construction of the main buildings and structures to host the accelerator are are outlined in the TDR Vol. 4 Infrastructure & Sustainability.

Based on the timeline to realize the HBS facility the main components of the accelerator with the full front end would be realized with an energy of up to 30 MeV and the part of the HEBT to transfer the proton beam to the first target station. For this part a construction and installation period of 4 years is scheduled. After this the accelerator would be equipped with further cavities to reach the design energy of 70 MeV and the multiplexer and additional sections of the HEBT system would be installed to accommodate the second target station. The timeline for this extension of accelerator and HEBT will be 3 years. At last the remaining part of the HEBT would be installed to serve the third target station. For this part of the installation about one year is estimated. Hence, the building and installation of the full accelerator and HEBT system of the HBS would be realized within 8 years after start of construction. A detailed timeline for the realization of HBS can be found in TDR Vol.4 Infrastructure & Sustainability.

Linac systems		Costs [MEUR]
Ion source	-	2.2
LEBT	-	1.2
RFQ 1+2	-	6.4
MEBT 1+2	-	1.6
DTL 0-35 MeV	-	42.6
DTL 35-50 MeV	-	16.5
DTL 50-70 MeV	-	27.5
Total	-	98.0
HEBT components	**Number**	**Costs [MEUR]**
Quadrupoles	85	4.6
Dipoles	16	4.4
Diagnostics	-	1.0
Beam transfer	-	2.0
Total	-	12.0
Other components		**Costs [MEUR]**
Beam dump	-	2.0
Multiplexer	-	1.0
Control system	-	2.0
Total	-	5.0

Table IX.2: *Estimated investment costs for HBS linac and HEBT systems.*

X.
AUTHOR LIST AND ACKNOWLEDGEMENTS

X.1 Volume author list

J. Baggemann, T. Gutberlet, E. Mauerhofer, I. Pechenitzkiy, U. Rücker, P. Zakalek
Forschungszentrum Jülich GmbH, Jülich Centre for Neutron Science, JCNS-HBS, Jülich, Germany

H. Kleines
Forschungszentrum Jülich GmbH, Jülich Centre for Neutron Science, JCNS-IT, Jülich, Germany

O. Felden, R. Gebel, A. Lehrach
Forschungszentrum Jülich GmbH, Nuclear Physics Institute, IKP-4, Jülich, Germany

M. Droba, K. Kümpel, S. Lambrecht, O. Meusel, N. Petry, H. Podlech, S. Reimann, M. Schwarz, C. Zhang
Goethe University Frankfurt, Institute for Applied Physics, Frankfurt, Germany

X.2 Acknowledgments

This Technical Design Report has been compiled with the kind support of a large number of colleagues at the Jülich Centre for Neutron Science and other collaborating institutes and universities. The editors would like to thank in particular:

J. Baggemann, Th. Brückel, J. Chen, T. Claudio Weber, T. Cronert (†), Q. Ding, P.-E. Doege, M. El Barbari, T. Gutberlet, J. Li, Z. Ma, E. Mauerhofer, N. Ophoven, I. Pechenitzky, T. Randriamalala, U. Rücker, N. Schmidt, A. Schwab, E. Vezhlev, P. Zakalek
Forschungszentrum Jülich GmbH, Jülich Centre for Neutron Science, JCNS-HBS, Jülich, Germany

F. Beule, P. Kämmerling, H. Kleines, K. Lieutenant, F. Suxdorf, J. Voigt
Forschungszentrum Jülich GmbH, Jülich Centre for Neutron Science, JCNS-IT, Jülich, Germany

B. Daegener, F. Gossen
Forschungszentrum Jülich GmbH, Jülich Centre for Neutron Science, JCNS-2, Jülich, Germany

N. Bernard, H. Feilbach, J. Lipperts, J. Peetz, S. Pistel, J. Schnitzler
Forschungszentrum Jülich GmbH, Jülich Centre for Neutron Science, PGI/JCNS-TA, Jülich, Germany

R. Achten, Y. Bessler, R. Hanslik, F. Löchte, M. Strothmann, J. Wolters
Forschungszentrum Jülich GmbH, Central Institute of Engineering, Electronics and Analytics, ZEA-1, Jülich, Germany

O. Felden, R. Gebel, A. Lehrach, M. Marzen, M. Rimmler, R. Similon
Forschungszentrum Jülich GmbH, Nuclear Physics Institute, IKP-4, Jülich, Germany

B. Neumaier
Forschungszentrum Jülich GmbH, Institute of Neurosciences and Medicine, INM-5, Jülich, Germany

O. Meusel, H. Podlech
Goethe University Frankfurt, Institute for Applied Physics, Frankfurt, Germany

W. Barth
GSI Helmholtzzentrum für Schwerionenforschung, Darmstadt, Germany / Helmholtz Institute Mainz, Mainz, Germany

J. Fenske, M. Müller, A. Schreyer
Helmholtz-Zentrum Geesthacht, Geesthacht, Germany

S. Böhm, J.-P. Dabruck, R. Nabbi
RWTH Aachen University, Nuclear Engineering and Technology Transfer, Aachen, Germany

S. Eisenhut, Ch. Haberstroh
Technische Universität Dresden, Bitzer-Chair of Refrigeration, Cryogenics and Compressor Technology, Dresden, Germany

C. Lange
Technische Universität Dresden, Institute of Power Engineering - Chair of Hydrogen and Nuclear Energy, Dresden, Germany

A.
APPENDIX

A.1 Simulation tools

The following simulation tools were used at the preparation of the MEBT and DTL chapter of this document.

A.1.1 LORASR

The beam dynamics design for the HBS linac was developed using two different beam dynamics codes. One of them is LORASR[1], a simulation program especially for drift-tube accelerators which use the KONUS beam dynamics. Details on the general functionality of LORASR can be found in [Rat98], on the PIC-FFT algorithm in [Tie09] and with focus on KONUS in [RHT+19]. Among the accelerator facilities where LORASR has been used so far are:

- GSI high-current injector (HSI) [Rat00b], high charge injector (HLI) [TCP+06], ion trap facility HITRAP [KRM04] FAIR proton injector [GBB+12] and HELIAC/cw-linac [Sch21],
- CERN Linac3 [Rat00a] and REX-ISOLDE (Geneva, Switzerland) [FPJV10],
- Fission fragment accelerator (MAFF) at the Munich II research reactor [Bon03],
- Heidelberg Ion Beam Therapy Center (HIT) [LMR+04],
- Ion Beam Therapy Center MedAustron (Wiener Neustadt, Austria) [Str06],
- CNAO (Pavia, Italy) [RHT+19],
- MIT (Marburg, Germany) [RHT+19],
- SPHIC (Shanghai, China) [RHT+19],
- EBIS pre-injector at BNL (Upton, USA) [RAK+07],
- TRIUMF ISAC-I (Vancouver, Canada) [TRP+08],
- FRANZ at Goethe University (Frankfurt, Germany) [NCD+11, Sch14, ABB+16],
- Injector for CSRm at HIRFL (Lanzhou, China) [ZYX12],

[1] Acronym for ger. *Longitudinale und radiale Strahltransportrechnungen unter Berücksichtigung der Raumladung* (longitudinal and radial beam transport calculations including space charge).

- HILac and LILac injectors for NICA at JINR (Dubna, Russia) [BDD+13, KBB+18],
- MYRRHA injector (Mol, Belgium) [Mä15, Pet14].

Probably the most important characteristic of a simulation is whether it is *realistic*, in the sense that the results determined by it, or in this case the particle beam dynamics, are actually true in reality or at least are reasonably accurate approximations. The successful construction and long-term operation of the accelerator facilities mentioned above can be regarded as a very strong indication of this. Therefore, LORASR has been chosen as primary simulation code for design and optimization of the beam dynamics layout in this TDR.

To model the acceleration gaps inside a cavity, LORASR proceeds as follows [Tie09]: After defining the array and geometry of the acceleration gaps (based on the input parameters of the designer) each gap field is approximated by an axially symmetric E-field (E_ϕ = const.). In radial direction, 4 zones with linearized longitudinal fields $E_z(z, r)$ are defined (zone borders are at $20\,\%$, $31.5\,\%$ and $40\,\%$ of the inner drift tube diameter $\varnothing_i$) divided into 5 individual zones along the beam axis for each gap, resulting in a total of 20 rings (A.1). Each particle is then tracked along each gap in a 30-step process.

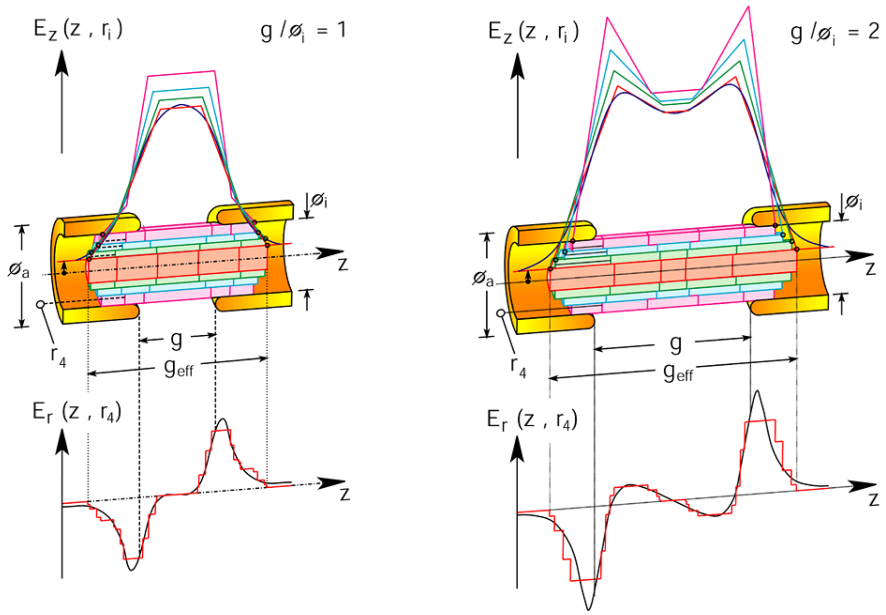

Figure A.1: *Schematic illustration of the longitudinal and radial E-field approximations used in LORASR for different gap geometries. [Rat98]*

A.1.2 TraceWin

Simulations for HBS have also been performed with TraceWin [UDP22]. It is a widely used and feature-rich beam dynamics code allowing start-to-end simulations from ion source to target. For large accelerator projects like ESS, MYRRHA, IFMIF, LINAC4, SPIRAL2, EUROTRANS, EUROISOL and SPL it has been chosen as reference code. Furthermore, a benchmark with the codes LORASR, DYNAMION and PARMILA at the UNILAC (GSI) has shown good agreement between the results. Also C. Zhang

et al. [ZKM+12] and H. Hähnel [HKR+19] found only minimal discrepancies between results from TraceWin and LORASR.

A crucial parameter for the accuracy of beam trajectories simulated with TraceWin is the way gaps in cavities are modeled in the simulation. In principle, three variants can be distinguished here:

1. **Thin Gap:** In the *Thin Gap* approximation, the forces on the particles of a bunch are only computed once – while the bunch center traverses the center of a gap. Thus, it is approximated to a literally infinitesimal thin gap. The great advantage of this variant is the high simulation speed it allows. Especially for error studies, which usually require a large number of simulations (order of magnitude 10^3), this advantage comes in handy. However, the highly simplifying approximation of the gap geometry is at the same time the disadvantage of this method. Longitudinally, often the largest emittance growth occurs compared to the other two methods, which approximate the longitudinal gap geometry more realistically. Especially for complex beam dynamics concepts like KONUS and EQUUS, this approximation therefore leads to errors that should be taken into account. Fine tuning of parameters such as the RF phase of cavities can help to account for the simplified gap geometry. This approximation already showed sufficiently accurate agreement to LORASR in relevant beam parameters for other linac designs.

2. **2D (LORASR) Field Map:** TraceWin gives the possibility to import electric and magnetic field maps of external programs, so 2D field maps of $E_z(z)$, generated by LORASR and sufficiently converted to the required data structure format by TraceWin could be used. Thus, the main disadvantage of the Thin Gap method can be eliminated, since the longitudinal field profile is now reproduced much more accurately. At the same time, the variable and by default smaller step size of the approximated radial field in TraceWin can be utilized. The transverse E-field components are not exported from LORASR and imported into TraceWin in this method but are approximated by TraceWin so that the transverse RF defocusing of the beam in acceleration gaps is also taken into account. This ultimately leads to an already quite detailed reproduction of the accelerator respectively the cavity in TraceWin.

3. **3D (CST) Field Map:** For a very realistic reproduction of the fields inside a cavity, a full 3D field map of the electric (and possibly magnetic) fields can be used, usually especially in the final phase of the design process. This can usually be exported from the electromagnetic 3D simulation program (e.g. CST Microwave Studio) and used accordingly, after a format conversion, in TraceWin. While the resulting simulation results can be considered the most accurate among the three methods, the simulation time required is also the largest. Moreover, the effort required for this method is by far the largest, since the 3D model of the cavity must be created (or even fully finalized for manufacturing) beforehand. This usually requires very extensive R&D activities (see e.g. [Dzi16] and [Bas19]).

When directly comparing LORASR simulations to TraceWin Thin Gap simulations, the following has been observed: Even though the energy gain per gap is identical in both codes, it was found that the shear transformation of the bunch (the shear transformation of the bunch is often referred to as "rotation", but which, however, is geometrically not fully correct) in the longitudinal phase space in TraceWin sometimes is too weak (compared to the LORASR calculation). The difference is that in TraceWin the full shear occurs at one point (in the center of the gap) and the bunch drifts until there with the low initial energy of the previous gap. In LORASR, on the other hand, the shear happens gradually in a 30-step process (with simultaneous gradual energy gain) over the entire effective length of the gap. This difference obviously affects mainly the edge particles of a bunch (in particular the *late* particles). It can be handled in TraceWin by slightly changing the RF phase of the cavity and/or adjusting the E-field amplitude of the cavity in a small percentage range.

To sum up, all three variants of gap modeling in TraceWin have their advantages and disadvantages. The big benefit of TraceWin is the possibility to perform start-to-end simulations with feature-rich

analysis methods. In this way, the entire beam dynamics behavior of an accelerator can be modeled and investigated in detail, from the ion source through all acceleration, diagnostic and transport sections to the target of the experimentalists. Therefore, LORASR and TraceWin are well suited in combination for HBS. While the former is used to design the basic design and lattice for the MEBT and CH sections, the latter is ideal for subsequent fine tuning of parameters, error studies and a holistic beam dynamics overview.

Bibliography

[ABB+16] S. Alzubaidi, U. Bartz, M. Basten, A. Bechtold, L. P. Chau, C. Claessens, H. Dinter, M. Droba, C. Fix, H. Hähnel, M. Heilmann, O. Hinrichs, S. Huneck, B. Klump, M. Lotz, D. Mäder, O. Meusel, D. Noll, T. Nowottnick, M. Obermayer, O. Payir, N. Petry, H. Podlech, U. Ratzinger, A. Schempp, S. Schmidt, P. Schneider, A. Seibel, M. Schwarz, W. Schweizer, K. Volk, C. Wagner, and C. Wiesner. The frankfurt neutron source franz. *Eur. Phys. J. Plus*, 131(5):124, may 2016.

[Bas19] M. Basten. *Entwicklung und Inbetriebnahme zweier supraleitender 217 MHz CH-Strukturen für das HELIAC-Projekt*. phdthesis, Johann Wolfgang Goethe-Universität, 2019.

[BDD+13] A.V. Butenko, E.E. Donets, E.D. Donets, V.V. Fimushkin, A.I. Govorov, V.V. Kobets, A.D. Kovalenko, K.A. Levterov, V.A. Monchinsky, I.N. Meshkov, A.Y. Ramsdorf, A.O. Sidorin, G.V. Trubnikov, A.S. Belov, G.N. Kropachev, T.V. Kulevoy, A.A. Kolomiets, S.M. Polozov, H. Hoeltermann, U. Ratzinger, A. Schempp, and H. Podlech. *Development of the NICA Injection Facility*. Proceedings of IPAC2013, Shanghai, China, THPWO069, 2013.

[Bol86] L. M. Bollinger. Superconducting linear accelerators for heavy ions. *Annual Review of Nuclear and Particle Science*, 36(1):475–503, 1986.

[Bon03] H. Bongers. *Entwicklung der 7-Spalt-Struktur für den Münchner Spaltfragmentbeschleuniger MAFF*. PhD thesis, Ludwig Maximilian University of Munich, Germany, 2003.

[BPS+93] L. M. Bollinger, R. C. Pardo, K. W. Shepard, J. M. Bogaty, B. E. Clifft, F. H. Munson, and G. Zinkann. First operational experience with the positive-ion injector of atlas. *Nuclear Instruments and Methods in Physics Research Section A: Accelerators, Spectrometers, Detectors and Associated Equipment*, 328(1):221–230, 1993.

[CSS] CSS. Official Control System Studio website. `https://controlsystemstudio.org/`.

[Dir23] SLAC Accelerator Directorate. Photo of SLAC Control Room, 2023. Available online: `https://accelerators.slac.stanford.edu/sites/default/files/styles/slideshow_image_description_bottom/public/acr-slide_0.jpg`.

[Dzi16] F. Dziuba. *Entwicklung und Test einer supraleitenden 217 MHz CH-Kavität für das Demonstrator-Projekt an der GSI*. PhD thesis, 2016.

[EPI] EPICS. Official EPICS website. `https://epics-controls.org/`.

[FPJV10] M. A. Fraser, M. Pasini, R. M. Jones, and D. Voulot. *Beam Dynamics Investigation of the 101.28 MHz IH Structure as Injector for the HIE-ISOLDE SC Linac*. 2010. arXiv:1006.0183.

[GBB+12] L. Groening, W. Barth, R. Berezov, G. Clemente, P. Forck, A. Krämer, C. Mühle, R. Hollinger, B. Launé, J. Lesrel, N. Chauvin, O. Delferrière, O. Tuske, C. Simon, B. Koubek, H. Podlech, U. Ratzinger, A. Schempp, and R. Tiede. *Status of the FAIR 70 MeV Proton Linac.* Proceedings of LINAC2012, Tel Aviv, Israel, THPB034, 2012.

[GBD+21] A. Gatera, J. Belmans, F. Davin, W. De Cock, F. Doucet, L. Parez, F. Pompon, A. Ponton, D. Vandeplassche, F. Bouly, C. Joly, L. Perrot, H. Podlech, J. Tamura, and C. Zhang. Minerva (MYRRHA Phase 1) RFQ Beam Commissioning. In *Proc. IPAC'21*, pages 675–678. JACoW Publishing, Geneva, Switzerland, 2021.

[HKK+19] H. Höltermann, B. Koubek, D. Koser, K. Kümpel, P. Müller, U. Ratzinger, M. Schwarz, W. Schweizer, J. Orboeck, M. Busch, H. Hähnel, H. Podlech, C. Angulo, H. Belmans, W. De Cock, P. D. Faille, F. Davin, F. Doucet, A. Gatera, F. Pompon, and D. Vandeplassche. Development status of the myrrha injector. *AIP Conference Proceedings*, 2160(1):050003, 2019.

[HKR+19] H. Hähnel, C. M. Kleffner, U. Ratzinger, M. Syha, and R. Tiede. End to end simulations and error studies of the fair proton linac. In *Proc. 10th Int. Particle Accelerator Conf. (IPAC'19)*, pages 885–888. JACoW Publishing, 2019.

[Hä17] J. H. Hähnel. *Development of an IH-type linac for the acceleration of high current heavy ion beams.* PhD thesis, 2017.

[Kas11a] K. Kasemir. Control System Studio Alarm Handling, 2011. CSS seminar at KEK. Available online: `https://www-linac.kek.jp/cont/epics/css/KEK_CSS_Alarms.ppt`.

[Kas11b] K. Kasemir. Control System Studio Overview, 2011. CSS seminar at KEK. Available online: `https://www-linac.kek.jp/cont/epics/css/KEK_CSS_Intro.pptx`.

[KBB+18] B. Koubek, M. Basten, A. Butenko, D. Donets, B. Golovenskiy, A. Govorov, H. Höltermann, C. Kampmeyer, K. Levterov, D. Lyuosev, A. Martynov, V. Monchinsky, H. Podlech, D. Ponkin, U. Ratzinger, A. Schempp, H. Schlarb, K. Shevchenko, I. Shirikov, E. Syresin, and R. Tiede. The new light ion injector for nica. *Proceedings of the 29th Linear Accelerator Conf.*, LINAC2018:China, 2018.

[KG18] K. Kasemir and G.Carcassi. Control System Studio Guide - For installers and maintainers of CS-Studio, 2018. Copyright Oak Ridge National Laboratory. Available online: `https://cs-studio.sourceforge.net/docbook`.

[KGC16] K. Kasemir, M. Grodowitz, and A. Carpenter. Display Builder Update, 2016. Spring 2016 EPICS Collaboration Meeting. Available online: `https://indico.esss.lu.se/event/507/contributions/3826/attachments/3838/5245/DisplayBuilder_2016_05.ppt`.

[KKL+18] K. Kümpel, D. Koser, S. Lamprecht, N.F. Petry, H. Podlech, A. Schempp, D. Strecker, A. Bechtold, and C. Zhang. Measurements of the MYRRHA-RFQ at the IAP Frankfurt. In *Proc. IPAC'18*, pages 949–951. JACoW Publishing, Geneva, Switzerland, 2018.

[KKMG08] J. Kim, D. H. Kim, W. Y. Maeng, and C.-S. Gil. Preliminary design of a beam dump for the high-energy proton accelerator of pefp. *JOURNAL OF THE KOREAN PHYSICAL SOCIETY*, 52(3, 1, SI):799–804, MAR 2008.

[KRM04] C. Kitegi, U. Ratzinger, and S. Minaev. *The IH Cavity for HITRAP.* Proceedings of LINAC 2004, Lübeck, MOP10, 2004.

[LMR+04] Y. R. Lu, S. Minaev, U. Ratzinger, B. Schlitt, and R. Tiede. *The Compact 20 MV IH-DTL fo the Heidelberg Therapy Facility.* Proceedings of LINAC 2004, Lübeck, MOP11, 2004.

[MRP+09] S. Minaev, U. Ratzinger, H. Podlech, M. Busch, and W. Barth. Superconducting, energy variable heavy ion linac with constant β, multicell cavities of CH-type. *Physical Review Special Topics - Accelerators and Beams*, 12(12), dec 2009.

[MRS99] S. Minaev, U. Ratzinger, and B. Schlitt. Apf or konus drift tube structures for medical synchrotron injectors - a comparison. In *Proc. 18th Particle Accelerator Conf. (PAC'99), New York, NY, USA*, pages 3555–3557, 1999.

[MSG+12] F. Martínez, F. Sordo, A. Ghiglino, M. Magán, S. Terrón, J. P. de Vincente, R. Vivanco, F. J. Bermejo, and M. Perlado. Design of a 300kw proton beam dump for ess-bilbao. *Journal of Neutron Research*, 01, 2012.

[MSH17] M. H. Mahmood, Suryanto, and M. H. Al Hazza. The effects of water flow rate on copper corrosion. In *Advanced Materials and Engineering Materials VI*, volume 748 of *Key Engineering Materials*, pages 235–239. Trans Tech Publications Ltd, 9 2017.

[MSL+12] A. Mayoral, J. Sanz, D. Lopez, E. Schibler, and L. Perrot. Beam dump of spiral2 facility: Residual dose rate calculations and impact of the computational approaches. *IEEE Transactions on Nuclear Science*, 59(4):1665–1671, 2012.

[Mä15] D. Mäder. *Die CH-Sektion des 17 MeV Injektors für MYRRHA.* PhD thesis, 2015.

[Mü15] R. Müller. Control systems for accelerators, operational tools. 2015. Available online: `https://www.helmholtz-berlin.de/pubbin/oai_publication?VT=1&ID=87868`.

[NCD+11] D. Noll, L. P. Chau, M. Droba, O. Meusel, H. Podlech, U. Ratzinger, and C. Wiesner. *Beam Dynamics of the FRANZ Bunch Compressor using realistic Fields with a Focus on the Rebuncher Cavities.* Proceedings of IPAC2011, San Sebastián, Spain, MOPS030, 2011.

[NIC] NICOS. Official NICOS website. `https://nicos-controls.org`.

[OMY+16] M. Otani, T. Mibe, M. Yoshida, K. Hasegawa, Y. Kondo, N. Hayashizaki, Y. Iwashita, Y. Iwata, E. Kitamura, and N. Saito. Interdigital h-mode drift-tube linac design with alternative phase focusing for muon linac. *Phys. Rev. Accel. Beams*, 19:040101, Apr 2016.

[Peg18] S. Peggs. ESS Technical Design Report. Technical report, 2018. ESS document ESS-doc-274. Available online: `https://http://eval.esss.lu.se/cgi-bin/public/DocDB/ShowDocument?docid=274`.

[Pet14] N. Petry. *Error-studies zum 17MeV Injektor für das MYRRHA-Projekt.* PhD thesis, 2014. bachelor thesis.

[PGvH+98] H. Podlech, M. Grieser, R. v. Hahn, S. Papureanu, R. Repnow, and D. Schwalm. The 7-gap-resonator–accelerator for the rex-isolde-experiment at cern. *Nuclear Instruments and Methods in Physics Research Section B: Beam Interactions with Materials and Atoms*, 139(1):447–450, 1998.

[PKL+17] H. Podlech, K. Kümpel, C. Lorey, N.F. Petry, A. Schempp, P.P. Schneider, A. Bechtold, and C. Zhang. The MYRRHA-RFQ - Status and First Measurements. In *Proc. IPAC'17*, pages 2243–2245. JACoW Publishing, Geneva, Switzerland, 2017.

[Pod99] H. Podlech. *Entwicklung des 7-Spaltresonator-Beschleunigers für das REX-ISOLDE-Projekt am CERN.* PhD thesis, 1999.

[Pod13] H. Podlech. Superconducting versus normal conducting cavities. *CAS - CERN Accelerator School: High Power Hadron Machines*, CERN-2013-001:151–170, 2013.

[RAK+07] D. Raparia, J. Alessi, A. Kponou, A. Pikin, J. Ritter, S. Minaev, U. Ratzinger, A. Schempp, and R. Tiede. *End-to-End Simulations for the EBIS Preinjector*. Proceedings of PAC07, Albuquerque, New Mexico, USA, TUPAS102, 2007.

[Rat98] U. Ratzinger. *Effiziente Hochfrequenz-Linearbeschleuniger für leichte und schwere Ionen*. Goethe University Frankfurt, Germany, habilitation thesis edition, 1998.

[Rat00a] U. Ratzinger. *H-type linac structures*. Number Nr. 12 in CAS - CERN Accelerator School : Radio Frequency Engineering, Seeheim, Germany, 8 - 16 May 2000. CERN, 2000.

[Rat00b] U. Ratzinger. *The New High Current Ion Accelerator at GSI and Perspectives for Linac Design Based on H-Mode Cavities*. Proceedings of EPAC 2000, Vienna, Austria, TUZF204, 2000.

[RFR+21] M. Rimmler, O. Felden, U. Rücker, H. Soltner, P. Zakalek, R. Gebel, T. Gutberlet, and T. Brückel. Developments of a multiplexer system for the high-brilliance neutron source hbs. *Journal of Neutron Research*, 23:1–14, 06 2021.

[RHT+19] U. Ratzinger, H. Hähnel, R. Tiede, J. Kaiser, and A. Almomani. Combined zero degree structure beam dynamics and applications. *Phys. Rev. Accel. Beams*, 22(11):114801, 2019.

[Roj20] U. Rojec. J-HBS Accelerator Control System Conceptual Design. Cosylab report, 2020.

[Sag06] D. Sagan. Bmad: A relativistic charged particle simulation library. *Nuclear Instruments and Methods in Physics Research Section A: Accelerators, Spectrometers, Detectors and Associated Equipment*, 558(1):356–359, 2006. Proceedings of the 8th International Computational Accelerator Physics Conference.

[Sch14] M. Schwarz. Numerische Simulationen zur Strahldynamik eines CH-Drifröhrenbeschleunigers. Master's thesis, 2014.

[Sch21] M. A. Schwarz. *Beam dynamics design of an energy-variable superconducting heavy ion accelerator*. doctoralthesis, Universitätsbibliothek Johann Christian Senckenberg, 2021.

[SHK+19] M. Schwarz, H. Höltermann, B. Koubek, H. Podlech, U. Ratzinger, W. Schweizer, D. Strehl, and C. Trageser. Development of an Automated BPM Test Bench. In *Proc. IBIC'19*, pages 651–654. JACoW Publishing, Geneva, Switzerland, 2019.

[Str06] T. Strodl. *Design and Beam Dynamics Simulation for the Ion-Injector of the Austrian Hadron Therapy Accelerator*. Proceedings of EPAC 2006, Edinburgh, Scotland, WEPCH157, 2006.

[SZ83] K. W. Shepard and G. P. Zinkann. A superconducting accelerating structure for particle velocities from 0.12- to 0.23-c. *IEEE Transactions on Nuclear Science*, 30:3339–3341, 1983.

[TAN] TANGO. Official TANGO website. `https://tangocontrols.org`.

[TCP+06] R. Tiede, G. Clemente, H. Podlech, U. Ratzinger, and A. Sauer. LORASR Code Development. In *Proc. 10th Europ. Particle Accelerator Conf. (EPAC 2006)*, pages 886–888, 2006.

[Tie09] R. Tiede. *Simulationswerkzeuge für die Berechnung hochintensiver Ionenbeschleuniger*. PhD thesis, 2009.

[TRP+08] R. Tiede, U. Ratzinger, H. Podlech, C. Zhang, and G. Clemente. *KONUS Beam Dynamics Designs using H-Mode Cavities*. Proceedings of Hadron Beam 2008, Nashville, Tennessee, USA, WGB11, 2008.

[UDP22] D. Uriot, R. Duperrier, and N. Pichoff. Tracewin, 2022. last requested on November 23rd, 2022.

[vGH+93] R. von Hahn, M. Grieser, D. Habs, E. Jaeschke, C.-M. Kleffner, J. Liebmann, S. Papureanu, R. Repnow, D. Schwalm, and M. Stampfer. Development of seven-gap resonators for the heidelberg high current injector. *Nuclear Instruments and Methods in Physics Research Section A: Accelerators, Spectrometers, Detectors and Associated Equipment*, 328(1):270–274, 1993.

[Wie14] Ch. Wiesner. *Chopping and transport of high-intensity ion beams*. PhD thesis, 2014.

[YHOY04] K. Yamamoto, T. Hattori, M. Okamura, and S. Yamada. The study of apf-ih linac. In *Proc. 9th European Particle Accelerator Conf. (EPAC'04), Lucerne, Switzerland*, pages 2679–2681, 2004.

[Zha22] C. Zhang. *Beam Physics and Techniques Towards Efficient Linear Accelerators with Space Charge Challenges, Habilitationsschrift*. University of Frankfurt, 2022.

[ZKM+12] C. Zhang, H. Klein, D. Mäder, H. Podlech, U. Ratzinger, A. Schempp, R. Tiede, and M. Vossberg. Front-end linac design and beam dynamics simulations for myrrha. pages 849–851. Proc. 26th Linear Accelerator Conf. (LINAC'12), Tel Aviv, Israel, Sep, 2012. paper THPB005.

[ZYX12] X. H. Zhang, Y. J. Yuan, and J. W. Xia. *One Design of Heavy Ion Linac Injector for CSRm*. Proceedings of LINAC2012, Tel Aviv, Israel, TUPB043, 2012.

List of Figures

FIGURE CREDITS

The following Figures displayed are used by permission as follows:

Cover figures, Fig. II.15, II.16, III.17, IV.1, V.1 : Goethe Universität Frankfurt

Fig. VII.3: SLAC

Schriften des Forschungszentrums Jülich
Reihe Allgemeines / General

Band / Volume 3
Advances in Nuclear and Radiochemistry
Extended Abstracts of Papers presented at the Sixth International Conference on Nuclear and Radiochemistry (NRC-6), 29 August to 3 September 2004, Aachen, Germany
edited by S. M. Qaim, H. H. Coenen (2004), XXXII, 794 pp
ISBN: 3-89336-362-9

Band / Volume 4
Wissenschaft im Zeichen der Zeit
Preisträger des Leibfried-Preises im Forschungszentrum Jülich 2000 – 2005
herausgegeben von R. Ball (2005), ca. 185 pp
ISBN: 3-89336-411-0

Band / Volume 5
Proceedings of the 1st International Conference on Natural and Biomimetic Mechanosensing
edited by: J. Casas, G. Krijnen, M. Malkoc-Thust, J. Mogdans, A. Offenhäusser, H. Peremans (2009), ca. 80 pp
ISBN: 978-3-89336-583-8

Band / Volume 6
Leo Brandt (1908-1971)
Ingenieur – Wissenschaftsförderer – Visionär
Wissenschaftliche Konferenz zum 100. Geburtstag des nordrhein-westfälischen Forschungspolitikers und Gründers des Forschungszentrums Jülich
herausgegeben von B. Mittermaier, B.-A. Rusinek (2009), I, 121 pp
ISBN: 978-3-89336-602-6

Band / Volume 7
Conceptual Design Report
NOVA ERA
(Neutrons Obtained Via Accelerator for Education and Research Activities)
A Jülich High Brilliance Neutron Source project
E. Mauerhofer, U. Rücker, T. Cronert, P. Zakalek, J. Baggemann, P.-E. Doege, J. Li, S. Böhm, H. Kleines, T. Gutberlet, and T. Brückel (2017), 68 pp
ISBN: 978-3-95806-280-1

Band / Volume 8
Conceptual Design Report
Jülich High Brilliance Neutron Source (HBS)
T. Brückel, T. Gutberlet (Eds.) (2020), 197 pp
ISBN: 978-3-95806-501-7

Schriften des Forschungszentrums Jülich
Reihe Allgemeines / General

Band / Volume 9-01
Technical Design Report HBS
Volume 1 – Accelerator
R. Gebel, A. Lehrach, H. Podlech (Vol. Eds.), T. Brückel, T. Gutberlet (Ser. Eds.)
(2023), 151 pp
ISBN: 978-3-95806-709-7

Band / Volume 9-02
Technical Design Report HBS
Volume 2 – Target Stations and Moderators
J. Baggemann, E. Mauerhofer, U. Rücker, P. Zakalek (Vol. Eds.),
T. Brückel, T. Gutberlet (Ser. Eds.) (2023), 118 pp
ISBN: 978-3-95806-710-3

Band / Volume 9-03
Technical Design Report HBS
Volume 3 – Instrumentation
K. Lieutenant, J. Voigt (Vol. Eds.), T. Brückel, T. Gutberlet (Ser. Eds.)
(2023), 163 pp
ISBN: 978-3-95806-711-0

Band / Volume 9-04
Technical Design Report HBS
Volume 4 – Infrastructure and Sustainability
T. Gutberlet (Vol. Eds.), T. Brückel, T. Gutberlet (Ser. Eds.)
(2023), 137 pp
ISBN: 978-3-95806-712-7

Band / Volume 9-Overview
Opportunities for Research with Neutrons at the Next Generation Facility HBS
Overview of the High Brilliance neutron Source (HBS) Technical Design Report
T. Brückel, T. Gutberlet (Eds.) (2023), 44 pp
ISBN: 978-3-95806-713-4

Allgemeines / General
Band / Volume 9-01
ISBN 978-3-95806-709-7

Mitglied der Helmholtz-Gemeinschaft

JÜLICH
Forschungszentrum